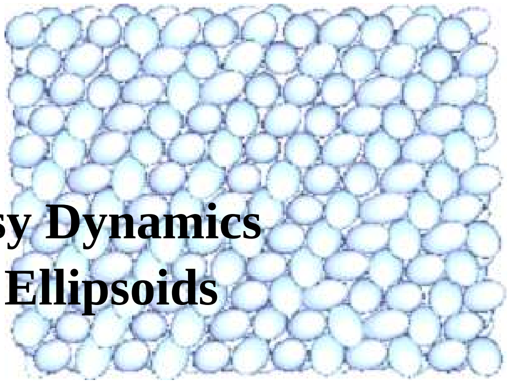

Crystal Phases and Glassy Dynamics in Monodisperse Hard Ellipsoids

Dissertation
zur Erlangung des Grades
"Doktor der Naturwissenschaften"
am Fachbereich Physik der
Johannes Gutenberg−Universität in Mainz

Patrick Pfleiderer

geb. in Nürnberg

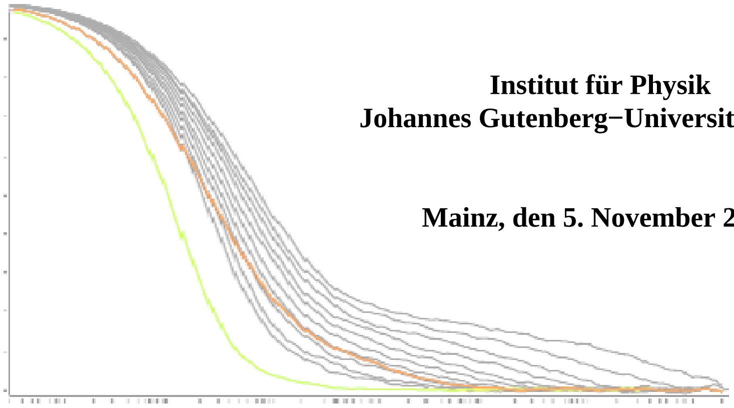

Institut für Physik
Johannes Gutenberg−Universität Mainz

Mainz, den 5. November 2008

Erstberichter:
Zweitberichter:
Tag der mündlichen Prüfung: 9. Februar 2009

Parts of this thesis have already been published in:

- P. Pfleiderer, K. Milinkovic, and T. Schilling
  Glassy dynamics in monodisperse hard ellipsoids
  Europhys. Letters **84**, 16003 (2008).
- P. Pfleiderer and T. Schilling
  Simple monoclinic crystal phase in suspensions of hard ellipsoids
  Phys. Rev. E **75**, 020402(R) (2007).

D77

Zusammenfassung

Wir haben Monte Carlo und Molekulardynamik-Simulationen an Suspensionen monodisperser, harter Ellipsoide durchgeführt. Harte-Teilchen-Modelle spielen eine Schlüsselrolle in der Statistischen Mechanik. Sie sind einfach und erlauben Einblicke in Systeme, in denen die Form der Teilchen wichtig ist, einschließlich atomarer, molekularer, kolloidaler und granularer Systeme.

Im Phasendiagramm prolater Ellipsoide fanden wir bei hohen Dichten eine neue Kristallphase, die stabiler ist als die bislang bekannte gestreckte FCC-Phase [1]. Die neue Phase, SM2, ist simpel-monoklin mit einer Basis von zwei Ellipsoiden, die ungleiche Orientierungen haben. Der Neigungswinkel β ist sehr weich bei Länge-zu-Breite-Verhältnis (Aspekt-Verhältnis) $l/w = 3$, wohingegen die anderen beiden Winkel nicht weich sind. Es gibt eine symmetrische Anordnung der Einheitszelle. Diese wurde in Verbindung gebracht mit den dichtesten bekannten Packungen von Ellipsoiden [2]; sie ist nicht immer die stabilste. Die gestreckte FCC-Phase wird also beim Aspekt-Verhältnis $l/w = 3$ durch SM2 ersetzt, sehr wahrscheinlich auch bei $3 \leq l/w \leq 6$, und vermutlich auch jenseits dieser Grenzen. Außerdem zeigen die Ellipsoide in SM2 bei $l/w = 1.55$ 180°-Drehungen, die einer näheren Untersuchung, z.B. des Einfrierens dieser Dynamik, würdig sind.

Zweitens haben wir die Dynamik fast kugelförmiger Ellipsoide untersucht. Im Gleichgewicht zeigen sie einen Phasenübergang erster Ordnung von der isotropen Phase in eine Rotatorphase, in der die Positionen kristallin und die Orientierungen frei sind. Bei Überkomprimierung der isotropen Phase in den Bereich der Rotatorphase haben wir Super-Arrhenius-Verlangsamung der Diffusion und Relaxation, und Signaturen des Käfig-Effekts beobachtet. Diese Merkmale von Glasdynamik sind so deutlich, dass asymptotische Gesetze der Modenkopplungstheorie (MCT) verifiziert werden konnten. Translatorische und Orientierungsfreiheitsgrade sind stark gekoppelt, mit der Konsequenz, dass ein gemeinsamer MCT-Glasübergangs-Volumenbruch ϕ_c existiert ($l/w = 1.25$: $\phi_c = 0.615 \pm 0.005$, $l/w = 0.80$: $\phi_c = 0.618 \pm 0.005$). 180°-Drehungen sind dagegen nicht betroffen. Unsere Resultate hängen nicht von der Simulationsmethode ab, wie von der MCT vorhergesagt. Bereits die Bewegung innerhalb der Käfige ist kooperativ. Dynamische Heterogenitäten wurden auch nachgewiesen. Der Transit zwischen Käfigen findet zwar in kurzen Zeitspannen statt, jedoch zeigt er keine von der Bewegung innerhalb der Käfige unterscheidbare Verschiebungen. Die Existenz glasiger Dynamik war durch molekulare MCT [3] (MMCT) vorhergesagt worden, jedoch ignoriert MMCT Kristallisation; ein Test per Simulation war nötig. Kristallisation verhindert typischerweise Glasdynamik in monodispersen Systemen. Polydispersität oder andere Asymmetrien sind nötig, um die Kristallisation zu unterbinden. Also fungiert die Anisometrie der Teilchen als Quelle von Unordnung. Dies wirft ein neues Licht auf die Bedingungen zur Glasbildung.

Abstract

We have performed Monte Carlo and molecular dynamics simulations of suspensions of monodisperse, hard ellipsoids of revolution. Hard-particle models play a key role in statistical mechanics. They are conceptually and computationally simple, and they offer insight into systems in which particle shape is important, including atomic, molecular, colloidal, and granular systems.

In the high density phase diagram of prolate hard ellipsoids we have found a new crystal, which is more stable than the stretched FCC structure proposed previously [1]. The new phase, SM2, has a simple monoclinic unit cell containing a basis of two ellipsoids with unequal orientations. The angle of inclination, β, is very soft for length-to-width (aspect) ratio $l/w = 3$, while the other angles are not. A symmetric state of the unit cell exists, related to the densest-known packings of ellipsoids [2]; it is not always the stable one. Our results remove the stretched FCC structure for aspect ratio $l/w = 3$ from the phase diagram of hard, uni-axial ellipsoids. We provide evidence that this holds for $3 \leq l/w \leq 6$, and possibly beyond. Finally, ellipsoids in SM2 at $l/w = 1.55$ exhibit end-over-end flipping, warranting studies of the cross-over to where this dynamics is not possible.

Secondly, we studied the dynamics of nearly spherical ellipsoids. In equilibrium, they show a first-order transition from an isotropic phase to a rotator phase, where positions are crystalline but orientations are free. When over-compressing the isotropic phase into the rotator regime, we observed super-Arrhenius slowing down of diffusion and relaxation, and signatures of the cage effect. These features of glassy dynamics are sufficiently strong that asymptotic scaling laws of the Mode-Coupling Theory of the glass transition (MCT) could be tested, and were found to apply. We found strong coupling of positional and orientational degrees of freedom, leading to a common value for the MCT glass-transition volume fraction ϕ_c ($l/w = 1.25$: $\phi_c = 0.615 \pm 0.005$, $l/w = 0.80$: $\phi_c = 0.618 \pm 0.005$). Flipping modes were not slowed down significantly. We demonstrated that the results are independent of simulation method, as predicted by MCT. Further, we determined that even intra-cage motion is cooperative. We confirmed the presence of dynamical heterogeneities associated with the cage effect. The transit between cages was seen to occur on short time scales, compared to the time spent in cages; but the transit was shown not to involve displacements distinguishable in character from intra-cage motion. The presence of glassy dynamics was predicted by MMCT [3]. However, as MMCT disregards crystallization, a test by simulation was required. Glassy dynamics is unusual in monodisperse systems. Crystallization typically intervenes unless polydispersity, network-forming bonds or other asymmetries are introduced. We argue that particle anisometry acts as a sufficient source of disorder to prevent crystallization. This sheds new light on the question of which ingredients are required for glass formation.

Contents

1 Introduction 1
- 1.1 Colloidal Suspensions 1
- 1.2 Hard-Particle Models 2
- 1.3 Hard Ellipsoids of Revolution 4
  - 1.3.1 Definition 4
  - 1.3.2 Earlier Work 5
    - 1.3.2.1 Equilibrium Results 5
    - 1.3.2.2 Close-Packing 7
    - 1.3.2.3 Dynamics 10
    - 1.3.2.4 Experiment 11
- 1.4 Glasses 14
  - 1.4.1 Overview 14
  - 1.4.2 The Mode-Coupling Theory of the Glass Transition 15

2 Simulation - Theory and Technique 23
- 2.1 Monte Carlo Simulation (MC) 23
  - 2.1.1 General Features 23
  - 2.1.2 Constant-Pressure-and-Tension Ensemble 24
    - 2.1.2.1 Partition Function 25
    - 2.1.2.2 Monte Carlo Moves 29
  - 2.1.3 Other Monte Carlo Versions 31
  - 2.1.4 Testing for Overlaps 32
- 2.2 Molecular Dynamics Simulation (MD) 32
  - 2.2.1 General Features 32
  - 2.2.2 Event-driven MD 33

3 Simple Monoclinic Crystal Phase 35
- 3.1 Overview of Simulations 35
- 3.2 The SM2 Phase at Aspect Ratio 3 38
  - 3.2.1 Characterization of Structure 38
  - 3.2.2 Close-Packing Limit 41

3.2.3 Softness of Inclination 43
3.2.4 Equation of State Data 45
3.3 Other Aspect Ratios and Phase Diagram 46
3.3.1 Aspect Ratios Greater Than 3 46
3.3.2 Aspect Ratios Smaller Than 3 48
3.3.3 Phase Diagram 49
3.3.4 Flipping Mode in SM2 at Aspect Ratio 1.55 51
3.4 Summary 51

4 Glassy Dynamics in Almost Spherical Ellipsoids 55
4.1 Overview of Simulations 55
4.2 Structure 60
4.2.1 Local Order: Pair Correlation Function 60
4.2.2 Intermediate Range: Static Structure Factors 60
4.3 Average Dynamics 62
4.3.1 Mean Squared Displacement and Diffusion 62
4.3.2 Relaxation 64
4.3.2.1 Intermediate Scattering Functions 64
4.3.2.2 Orientational Correlation Functions 69
4.3.3 Slowing-down of Diffusion and Relaxation 71
4.3.4 Testing Mode-Coupling Theory 71
4.3.4.1 MD vs. MC 75
4.3.4.2 Time-Volume Fraction Superposition Principle . 75
4.3.4.3 Von Schweidler Law and Factorization Property 79
4.3.4.4 MCT Glass Transition Volume Fraction 84
4.4 Heterogeneous Dynamics 86
4.4.1 Non-Gaussian Parameter 86
4.4.2 Jumps 88
4.5 Summary 91

A Corrected Constant-Pressure Ensemble 97

Bibliography 101

List of Figures

1.1 Left: schematic colloidal suspension. Right: real colloidal suspension (courtesy of T. Palberg, http://kolloid.physik.uni-mainz.de/). In the schematic, a crystal is alluded to in the bottom-right corner. The real suspension contains spherical polymer particles whose index of refraction is close to that of the solvent. Hence, they cannot be seen in the isotropic phase (top, dark region); but they display Bragg scattering of green light in the crystalline phase at the bottom. 2

1.2 Ellipsoids of revolution. 5

1.3 Frenkel and Mulder's phase diagram of hard ellipsoids (adapted from [1] with permission). At low densities, there is an isotropic phase (I, illustrated in green), in which all degrees of freedom are disordered. At high densities, we have a solid phase (S, black), with orientational and positional order. Beyond moderate anisometry, a nematic phase exists in between (N, dark blue), where one has orientational order only (all ellipsoids point in nearly the same direction). Finally, nearly spherical ellipsoids can form a plastic solid phase (PS, light blue), with positional order and orientational disorder. Grey regions mark coexistence. 6

1.4 Construction of the sFCC crystal of ellipsoids as done in Ref. 1. The upper part shows an FCC crystal of spheres in the [111] direction (left) and in the two perpendicular directions labeled x and y (middle and right). The lower part shows the same structure after an affine stretch in the [111] direction. The volume fraction (at close-packing $\phi \approx 0.74$) remains unchanged. 8

1.5 Construction of densest-known packings of ellipsoids [2]. In each sketch, two layers of particles are shown, a lower one (filled with light blue) and an upper one (transparent with dark outline). Such pairs of layers can be stacked to fill all space. a) Layers of FCC-packed spheres. The spheres are deformed to ellipsoids until they touch an additional two neighbors (*n* is the number of touching neighbors). The directions of deformation alternate perpendicularly from layer to layer. The ellipsoids remain at their lattice sites, as one can check with the red reference square. b) The resulting structure has the maximal volume fraction $\phi \approx 0.7707$. The diagonal line indicates a plane of symmetry in which an affine stretch keeps all ellipsoids congruent. c) Same as b), but rotated by 45^o. d) Same as c), but after an in-plane stretch to obtain ellipsoids with $l/w = 3$, packed at $\phi \approx 0.7707$. 9

1.6 Equilibrium phase diagram of hard ellipsoids (adapted from [1] with permission) showing the Molecular Mode-Coupling Theory results of Letz et al. [3]. The red line marks a discontinuous (Type B) glass transition line, which follows the coexistence region delimiting the isotropic regime; and a continuous (Type A) transition line inside the plastic-solid region, affecting flipping modes only. In addition, the blue arrows indicate that positional freedom of the particles is governed by density, while the turquoise arrows indicate that orientational freedom is governed by anisometry. This decoupling was found by de Michele et al. [30]. In green we preview our result that both orientational and positional degrees of freedom are strongly slowed down by the indicated over-compression. 12

1.7 Micrograph of polystyrene ellipsoids ($l/w \approx 2.5$, $w \approx 3\,\mu$m), prepared by the author during a visit to the group of Prof. Jan Vermant (Katholieke Universiteit Leuven). 14

1.8 Schematic time dependence of correlators, for liquid to supercooled regimes and the glass case (high to low temperatures, or low to high densities). 19

2.1 Illustration of Monte Carlo moves. In addition to particle moves, changes of the box shape are indicated. Left: Constant-pressure MC. Right: Constant-pressure-and-tension MC. 30

3.1 Top: Constructed sFCC (cf. Figure 1.4) which was input. Bottom: Snapshot of the SM2 crystal which spontaneously formed from it. The color code distinguishes orientations. 39

3.2 Left: Snapshot of SM2 ($P = 46$, $N = 1728$) in which the collective re-orientation took place along an oblique angle with respect to the box walls. The arrangement of tips on a rectangular lattice is clearly visible. Right: Illustration of the possible directions of re-orientation from sFCC. The yellow line indicates the one the system on the left had chosen, the red ones indicate the other two possibilities. 40

3.3 Unit cell of SM2 for $l/w = 3$. The open circles indicate the centers of the two ellipsoids which form the basis. The yellow ellipsoid is at the origin, the green one is at $\frac{1}{2}(\mathbf{a}+\mathbf{b})$. The orientations are symmetric about the *ac*-plane. The cell is monoclinic. β exhibits large variations. The parameters in Parts a) and b) are average values for $N = 1728$ and $P = 46$. Part c) shows the cell at close-packing with $\beta \approx 148.3^\circ$, where it is an instance of the family of packings introduced by Donev et al. [2]. Part d) illustrates that β specifies the angle which the planes of equal orientations form with the basis of the simulation box from Figure 3.1. 41

3.4 a) Maximizing the density of SM2. β increases and planes of equal orientations slide past each other in the process. The resulting structure is an instance of the family of packings reported by Donev et al. [2]. b) Perspective from which to view the Donev packing to identify it with close-packed SM2. 42

3.5 Inclination as monitored by the shear variable g_{23}, for the runs $l/w = 3$, $N = 432$, $P = 46$ (top) and $P = 36$ (bottom). g_{23} fluctuates over a broad range, corresponding to values of β in the range $105^\circ < \beta < 150^\circ$. Variations of g_{23} corresponding to 15° in β were typical at both pressures even within a single simulation. This implies a small shear modulus of elasticity. Also shown for comparison is g_{13} (blue) which remains near zero (i.e. the angle γ remains near 90°); it fluctuates much less, corresponding to a much larger shear modulus. The lower plot ($P = 36$) suggests metastability of two angles. 44

3.6 a) Planes slide well past each other in the direction indicated by the arrows. b) Defect as a result of the softness. The orientations in one plane (fifth from right) have slightly changed. c) Centers of mass of the same configuration, exposing the undulations in the lattice. 45

3.7 Equation of state data for hard ellipsoids at $l/w = 3$. Errors are smaller than symbol size. Lines guide the eye. The density of SM2 (blue solid squares) is higher than that of sFCC (red open squares [1]) for all pressures. SM2 melts directly to the nematic phase without revisiting the sFCC phase. The nematic branch (triangles) is shown including over-compressed states. The isotropic fluid states are shown as circles. 46

3.8 SM2 with aspect ratio $l/w = 6$, $N = 3072$, and $P = 46$. Left: defect-free structure. Right: two vertical planar defects, separating two conflicting orientations of SM2. 47

3.9 SM2 with defect due to a geometrical mismatch of the simulation box and the unit cell ($l/w = 6$, $N = 2352$, $P = 36$). Planes of one orientation meet with planes of the other orientation after one periodic length. 48

3.10 Phase diagram of hard, uni-axial ellipsoids ($l/w \geq 1$). The scaling of the abscissa is reciprocal. The diagram shows the results of Frenkel and Mulder [1] (open symbols), and their suggested phase boundaries and coexistence regions. The data points at $l/w = 1$ are taken from Hoover and Ree [72]. We have inserted our state points (filled symbols, errors less than symbol size) and a vertical dashed line to delimit the region in which SM2 was found more stable than sFCC. To the left of it, both sFCC and SM2 are metastable, and assessing their relative stabilities requires free-energy calculations (in progress [70]). Preliminary results [71] indicate that SM2 is more stable down to $l/w = 2$, but that sFCC is more stable at $l/w = 1.55$. Our solid state points are isobar at $P = 46$ (except for the lower SM2 one at $l/w = 3$, where $P = 30$). 50

3.11 Left: snapshot of SM2 at $l/w = 1.55$ ($N = 432$, $P = 46$). The colorful appearance documents the expectedly large fluctuations around the preferred orientations. Right: distribution of orientations on the unit sphere from the same system. The existence of four preferred orientations shows that the particles have been able to flip upside-down (this does not reflect onto the color code of the snapshot). 52

4.1 Snapshots of the simulated suspensions. The color code indicates orientation. At first sight, they all look the same. However, the upper systems contain prolate ($l/w = 1.25$) ellipsoids, while the lower ones contain oblate ($l/w = 0.8$) ellipsoids; and the left-hand systems are isotropic, while the right-hand systems are plastic solids. Especially for $l/w = 0.8$, the plastic solid is not easy to identify by eye. 56

4.2 Pair correlation functions $g(r)$ for the prolate (top) and the oblate (bottom) systems, for several volume fractions ϕ (see legend). MC and MD data fully agree and so their average was taken. The maximum represents the nearest-neighbor distance; it moves to smaller values as the volume fraction is increased. Its location for the highest volume fraction is 1.131 (prolate system, $\phi = 0.598$) and 0.994 (oblate system, for both $\phi = 0.598$ and $\phi = 0.614$). . . 61

4.3 Static structure factors $S(q)$ for the prolate (top) and the oblate (bottom) systems, for several volume fractions ϕ (see legend). MC and MD data fully agree and so their average was taken. The maximum represents a recurring length scale due to the neighbor spacing; it moves to higher values of q as the volume fraction is increased. The black dotted line indicates q_{max} used for the analysis of the dynamics ($l/w = 1.25$: $q_{\text{max}} = 6.85$; $l/w = 0.8$: $q_{\text{max}} = 7.85$). There are no features for $q < q_{\text{max}}$, i.e. on length scales larger than the neighbor spacing. 63

4.4 Mean-squared displacements (MSD) of all systems at several volume fractions ϕ (see legend). One can see the ballistic regime (MD only) at early time scales and the diffusive regime at late time scales. Towards high volume fractions there is a sub-diffusive regime on intermediate time scales, indicative of glassy dynamics. 65

4.5 Self-intermediate scattering functions $F_{\text{s}}(q_{\text{max}}, t)$ at several volume fractions ϕ (see legend), with q_{max} near the maximum of the static structure factor (see Figure 4.3). Towards high volume fractions there develops a plateau on intermediate time scales. The final relaxation is slowed down strongly with increasing volume fraction, indicative of glassy dynamics. 67

4.6 Second-order orientational correlators $L_2(t)$ at several volume fractions ϕ (see legend). Again a plateau develops with increasing volume fraction, i.e. the glassy dynamics affects the orientational degrees of freedom as well. Hence, orientational degrees of freedom are coupled to positional ones. 70

4.7 Third-order orientational correlators $L_3(t)$ at the lowest and highest simulated ϕ (see legend). Comparing to $L_2(t)$ (grey curves), they do not slow down significantly, indicating that flipping modes are not affected by the onset of glassy dynamics. 72

4.8 Inverse relaxation times τ^{-1} obtained from $F_\mathrm{s}(q_\mathrm{max},t)$ (triangles) and from $L_2(t)$ (circles), and diffusion constants D (squares), as a function of volume fraction ϕ, for all systems. MC data: filled symbols (with lines to guide the eye); MD data: open symbols. The MC values have been multiplied by a factor of 24 (prolate) and 18 (oblate) to match the MD time scale [$L_2(t)$: 19 and 16, respectively]. D is in units of $(2\pi/q_{max})^2/[t]$ to account for the structural length scale given by the neighbor spacing. See Figure 4.3 for the definition of q_{max}. The plots show excellent agreement between MD and MC. 73

4.9 MC data of diffusion constants (squares) and inverse relaxation times (F_s: triangles, L_2: circles), comparing the prolate (red, open symbols) and the oblate (blue, solid symbols) system. The data are extremely similar, indicative of symmetry under exchange of l/w with its inverse; this is seen in D as well, thanks to the choice of units $[D]=(2\pi/q_{max})^2/[t]$. 74

4.10 Comparing the long-time shapes of the intermediate scattering functions $F_\mathrm{s}(q_\mathrm{max},t)$ from MC and MD for all volume fractions ϕ. The lowest and highest volume fractions are annotated. The MD functions have been rescaled in t to match with the MC data at long times [for $\phi < 0.598$ the ratio of relaxation times was used; for $\phi = 0.598$, more precise adjustment lead to multiplication of MD times by 21.0 ($l/w = 1.25$) and 16.67 ($l/w = 0.8$)]. Excellent agreement is found with the (M)MCT prediction that the long-time dynamics not depend on microscopic dynamics (i.e. simulation method). 76

4.11 Comparing the long-time shapes of the second-order correlators $L_2(t)$ from MC and MD for the range of ϕ as annotated. The MD functions have been rescaled in t to match with the MC data at long times (the ratio of relaxation times was used except for $l/w = 1.25$, $\phi = 0.598$, where we multiplied MD times by 19). Apart from statistical fluctuations, the long-time dynamics are confirmed to be independent of the microscopic dynamics. 77

4.12 Comparing the long-time shapes of the intermediate scattering functions from MC and MD, for $\phi = 0.598$ and wave vectors in the range $2.8 \leq qw \leq 18$. The MD functions of each system have been rescaled in t by one common factor to match with the MC data at long times ($l/w = 1.25$: multiplied by 21.0; $l/w = 0.8$: multiplied by 16.67). The shapes match well over this wide range of wave vectors after 10^5 time units, even for the case of $l/w = 1.25$ which has poor statistics. 78

4.13 Time-volume fraction superposition principle for $F_\mathrm{s}(q_\mathrm{max}, t)$. All curves have been rescaled by their relaxation time τ to check whether a master curve results, as MCT predicts for the vicinity of the glass transition. Two curves seem to violate the prediction: the cyan one in $l/w = 1.25$ MC ($\phi = 0.598$), and the black one in $l/w = 0.80$ MC ($\phi = 0.606$). The deviation of both is of statistical origin, and the deviation of the former is aggravated by the uncertainty due to extrapolation when determining τ. The two outliers do not change the conclusion that the superposition principle holds. 80

4.14 Time-volume fraction superposition principle for $L_2(t)$. All curves have been rescaled by their relaxation time to check whether a master curve results, as MMCT predicts for the vicinity of the glass transition. In the MD data, some of the lowest volume fractions' curves are not considered as the near-vanishing plateau made it impossible to extract the relaxation time. The MMCT prediction is clearly confirmed. 81

4.15 Upper panels: $F_\mathrm{s}(q,t)$ for $l/w = 1.25$ and the highest volume fraction $\phi = 0.598$, and for q-vectors (from top) 2.8, 4.0, 5.5, 7.1, 8.1, 10.1, 12.1, 14.1, 18.1. The red lines show examples of the von Schweidler fit $F_\mathrm{s}(q,t) = f_q - h_q^{(1)} t^b + h_q^{(2)} t^{2b}$ with $b = 0.65$. Lower panels: the same correlators after transformation to $R(t) = [F_\mathrm{s}(q,t) - F_\mathrm{s}(q,t_1)]/[F_\mathrm{s}(q,t_2) - F_\mathrm{s}(q,t_1)]$, demonstrating the factorization property. The color code, distinguishing wave vectors, shows that the curves remain ordered, i.e. a curve which is above another one before the collapse is above the other one after as well. 82

4.16 Same as Figure 4.15, but for $l/w = 0.80$; $\phi = 0.614$ for MC and $\phi = 0.598$ for MD. 83

4.17 q-dependence of the fit parameters in the von Schweidler law $F_{\mathrm{s}}(q,t) = f_q - h_q^{(1)} t^b + h_q^{(2)} t^{2b}$. See legend for aspect ratio, simulation method, and volume fraction. $h_q^{(1)}$ of $l/w = 1.25$ (MD) was rescaled by 16.67^b, and of $l/w = 0.8$ (MD) by 21.0^b; $h_q^{(2)}$ was rescaled by the squared value in each case. f_q resembles a Gaussian, and for $\phi = 0.614$, $l/w = 0.8$ (MC) the curve can in fact be well fitted, up to $q = 16$, by $f_q = \exp(-r_{\mathrm{L}}^2 q^2)$, with the localization length $r_{\mathrm{L}} = 0.072$ (red dashed line). For $\phi = 0.598$, $l/w = 1.25$ (MD) we show the corresponding fit (cyan dashed line, $r_{\mathrm{L}} = 0.087$) which is less satisfactory. 85

4.18 $\tau^{-1/\gamma}$ multiplied by arbitrary factors for clarity, from $F_{\mathrm{s}}(q,t)$ (from top: $l/w = 1.25$: qw = 6.85, 11, 16; $l/w = 0.8$: qw = 7.85, 16, 20) and L_2 (bottom), demonstrating the validity of the MCT scaling law $\tau^{-1} \propto (\phi_c - \phi)^\gamma$. The exponent $\gamma = 2.3$ was chosen in agreement with $b = 0.65$. The straight-line fits indicate a glass transition volume fraction of $\phi_c = 0.615 \pm 0.005$ (prolate system) and $\phi_c = 0.618 \pm 0.005$ (oblate system). MC and MD data agree. . . . 87

4.19 Non-Gaussian parameter for all systems. Towards higher volume fractions, a maximum develops, and its position on the time axis coincides with the departure from the plateau in the intermediate scattering function. Hence, the dynamics becomes heterogeneous when the development of the system is governed by the cage effect. When most particles escaped from their cages, the associated larger displacements dominate and follow a Gaussian distribution, making the non-Gaussian parameter zero again. 89

4.20 Trajectory of a fast particle from the MC simulation of $l/w = 0.8$ at $\phi = 0.614$. Three cages can be identified, whose size agrees with the result from the mean-squared displacement, $r_{\mathrm{MSD}} \approx 0.2w$. Moving to a new cage may later be followed by the return to the previous cage. The displacements between individual positions are of similar size within a cage and during transit. 90

4.21 Self part of the van Hove correlation function (times r^2) for several values of t, in linear (top) and semi-logarithmic (bottom) plots, from the MC simulation of $l/w = 0.8$ at the highest volume fraction $\phi = 0.614$. It is the distribution of scalar displacements r in the interval t. The curves are normalized to unit area. The largest value of t corresponds to maximal dynamical heterogeneity, i.e. where the non-Gaussian parameter (Figure 4.19) has its maximum. The dotted vertical lines indicate the partitioning of particles according to their mobility for further analysis. 92

4.22 Normalized distributions of scalar displacements during intervals of 10^5 MC steps, on linear (top) and semi-logarithmic (bottom) plots, from the MC simulation of $l/w = 0.8$ at the highest volume fraction $\phi = 0.614$. The particles were separated into sets of various mobilities on a longer time scale ($5 \cdot 10^6$ MC steps; see also Figure 4.21). The shape of the curves is essentially the same from the fastest down to the slowest set of particles. Fast particles show an overall shift of their short-term displacements towards larger values, and not the addition of few large displacements to an otherwise similar distribution. 93

Symbols and Units

Constants and Variables

k_B	Boltzmann's constant
T	temperature
E	energy
U	potential energy
N	number of particles
V	volume
ϕ	volume fraction (filled space / all space)
ρ	number density
P	pressure
F	Helmholtz free energy
G	Gibbs free energy
Z	partition function
m	particle mass
l	ellipsoid length
w	ellipsoid width
l/w	aspect ratio of each ellipsoid
$\mathbf{r}$	position
$\mathbf{u}$	orientation
r	(scalar) displacement
$\mathbf{a}$, $\mathbf{b}$, $\mathbf{c}$	unit cell vectors
β	crystal: angle of inclination; glass: stretching parameter
$\mathbf{q}$, q	wave vector, its magnitude
τ	relaxation time
λ	MCT exponent parameter
a, b, γ	MCT exponents
δ_max	max. trial move size
R_A	acceptance ratio
r_MSD	mean cage radius
r_I	instantaneous cage radius

Units

length	particle width w
mass	particle mass m
moment of inertia	mw^2
temperature	irrelevant in hard-particle systems
energy	$k_\mathrm{B}T$
pressure	$k_\mathrm{B}T/[(l/w)w^3]$
volume fraction	dimensionless
number density	$1/[(l/w)w^3]$ (same as in Frenkel and Mulder [1])
time (MC)	MC step (see Section 2.1.3)
time (MD)	MD step (see Section 2.2.2)

Conversions

volume fraction = $\pi/6$ number density

Abbreviations

MC	Monte Carlo
MD	Molecular Dynamics
FCC	face-centered cubic
sFCC	stretched face-centered cubic
SM2	simple-monoclinic with a basis of two ellipsoids
MSD	Mean-squared displacement
NGP	Non-Gaussian parameter
MCT	Mode-Coupling Theory
MMCT	Molecular Mode-Coupling Theory

Chapter 1

Introduction

1.1 Colloidal Suspensions

A colloidal suspension is any system in which particles are dissolved in a continuous solvent. The particles typically have sizes from nanometers to micrometers. With such a general definition, it comes as no surprise that there are many examples: In milk, there are fat droplets in water; in paint, there are pigments in a solvent; dust in air forms a colloidal suspension; motor oil carries metal particles—and so on. An even more general definition includes systems which have any structure on the μm to nm scale, not just particles.

Instead of "colloidal suspensions", one often simply says "colloids". Occasionally, an individual particle in a suspension is called a colloid. The original meaning of the word is "glue-like" and comes from the Greek "kolla" (glue) and "eidos" (appearance). The term was introduced in 1861 by Thomas Graham, the reputed founder of colloid chemistry [4].

Figure 1.1 shows an illustration of a colloidal suspension (left) and a real example (right). In the schematic, we see an isotropic (disordered) phase, and in the bottom-right corner a crystal phase is indicated. There exists a rich variety of phases in colloidal suspensions, depending on the properties of the particles and the solvent. We will encounter some more below. The real colloidal suspension in Figure 1.1 (right) contains spherical polymer particles whose index of refraction is close to that of the solvent. Hence, they cannot be seen in the isotropic phase (top, dark region); but they display Bragg scattering of green light in the (poly)crystalline phase at the bottom.

Apart from their beauty and interesting properties, colloidal suspensions are popular since they allow the study of many-particle physics in a direct way: The size of the particles makes them visible under the microscope, their dynamics is slow enough to be followed in experiment, and the scale of particle interactions

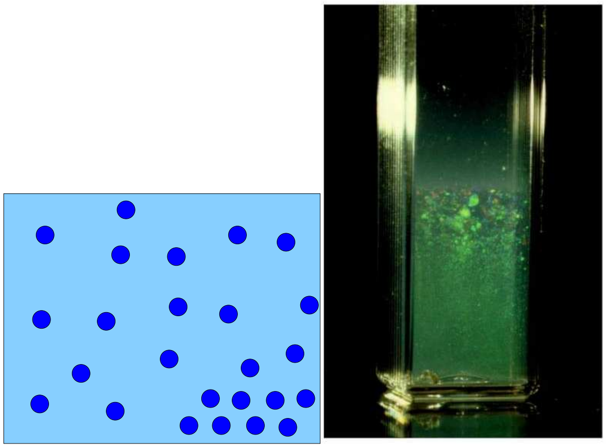

Figure 1.1: Left: schematic colloidal suspension. Right: real colloidal suspension (courtesy of T. Palberg, http://kolloid.physik.uni-mainz.de/). In the schematic, a crystal is alluded to in the bottom-right corner. The real suspension contains spherical polymer particles whose index of refraction is close to that of the solvent. Hence, they cannot be seen in the isotropic phase (top, dark region); but they display Bragg scattering of green light in the crystalline phase at the bottom.

is on the order of $k_\mathrm{B}T$ at room temperature. On the other hand, the phase behavior and non-equilibrium phenomena of colloids may translate to those of other systems. For example, Pusey and van Megen [5] discovered that suspensions of nearly-hard spheres display equilibrium and glass phases found in atomic systems. Thus, the understanding of the statistical physics of colloids promises the understanding of other systems, including atomic, molecular, or granular ones.

1.2 Hard-Particle Models

Consider a system of N identical, hard molecules in the canonical ensemble. The potential energy is zero everywhere in phase space except when particles overlap, where it is infinite. Therefore, the particles never overlap, and the potential energy is always zero. The internal energy E has only the kinetic contribution for $6N$ degrees of freedom, so that the Helmholtz free energy is

$$F(N,V,T) = E(N,V,T) - TS(N,V,T) = \frac{6N}{2}k_\mathrm{B}T - TS(N,V,T)$$

Note that the configurational space available to the system is independent of internal energy, so that S is not a function of E or T:

$$F(N,V,T) = k_{\mathrm{B}}T\left[\frac{6N}{2} - \frac{1}{k_{\mathrm{B}}}S(N,V)\right]$$

and we see that T is nothing but an overall scaling parameter in hard-particle systems. We therefore express the free energy in units of $k_{\mathrm{B}}T$. Also, since N is constant, the kinetic term will not contribute to the equilibrium behavior, and can be disregarded. We have

$$\frac{F(N,V,T)}{k_{\mathrm{B}}T} = -\frac{1}{k_{\mathrm{B}}}S(N,V) \tag{1.1}$$

Hence, the equilibrium behavior of hard-particle systems is fully determined by entropy. For this reason, they are also called *entropic systems*.

In terms of the partition function in the canonical ensemble, we have

$$Z(N,V,T) \;=\; \frac{1}{N!\lambda^{6N}}\int\limits_{V} d\mathbf{r}^N \int\limits_{4\pi} d\mathbf{u}^N \exp\left[-U(\{\mathbf{r}_i\},\{\mathbf{u}_i\})/k_{\mathrm{B}}T\right] \tag{1.2}$$

where $\lambda = \sqrt{h^2/(2\pi m k_{\mathrm{B}}T)}$ is the thermal de Broglie wavelength[1], $\mathbf{r}_i$ is the position and $\mathbf{u}_i$ the orientation of particle i, $U(\{\mathbf{r}_i\},\{\mathbf{u}_i\})$ is the potential energy, and the curly braces denote that the potential energy is a function of all positions and orientations. We will in the following drop the prefactors, which have no influence on the equilibrium behavior. Given the nature of the potential energy, the exponential in Eq. (1.2) will be unity everywhere except for the case of overlap, where it is zero. So we may write

$$Z(N,V) = \int\limits_{V}\int\limits_{4\pi}\limits_{\text{no overlap}} d\mathbf{r}^N d\mathbf{u}^N \tag{1.3}$$

This is precisely the configurational space available to the system, so that

$$S(N,V) = k_{\mathrm{B}}\ln Z(N,V)$$

Recalling that

$$F = -k_{\mathrm{B}}T\ln Z$$

we note that Eq. (1.3) is equivalent to Eq. (1.1).

---

[1] assuming unit moment of inertia for simplicity.

The simplicity of Eq. (1.3) is one reason why hard-particle models are so attractive. The behavior of the system is only a matter of geometry. This also makes computer simulations relatively easy. One of the first applications of computer simulations was a study of the liquid-solid phase transition in hard spheres [6].

But the chief motivation for the study of hard-particle models is that all structural properties are purely a result of the shape of the particles (the dynamics also depend on the moment of inertia of the particles). The importance of shape was highlighted by Onsager in 1949 [7], who showed that particle anisotropy alone can lead to an isotropic-nematic transition[2]. The understanding of hard-particle models expedites the understanding of more complicated systems, where effects from particle shape may be anticipated and contrasted with other effects. For further reading on hard-particle models, we recommend the reviews by Care and Cleaver [8] and by Wilson [9].

We point out that the trivial kinetic contribution in the above equations does not make the dynamics, the time evolution, of a system trivial. While the instantaneous distribution of momenta will follow the familiar results at all times, the properties of diffusion and relaxation may nevertheless be intricate. Particles may be constrained to local motion for long times (Section 1.4).

1.3 Hard Ellipsoids of Revolution

1.3.1 Definition

One hard-particle model is the suspension of hard ellipsoids. In our study, the ellipsoids are uni-axial, i.e. they possess two equal axes of size w, and one special axis of size l. w, the width of the particles, provides the unit of length used throughout this work. The ratio l/w is the aspect ratio. If l/w is larger than unity, the ellipsoids are called prolate; if it is smaller than unity, they are oblate. Since uni-axial ellipsoids can be constructed by revolving an ellipse around one axis, they are also called ellipsoids of revolution. Our ellipsoids are monodisperse; i.e., they all have the same size and aspect ratio. The suspension is a collection of ellipsoids in a box of fixed or variable size, depending on the choice of thermodynamic ensemble. Figure 1.2 illustrates the model.

---

[2] The nematic phase is introduced in Section 1.3.2.1.

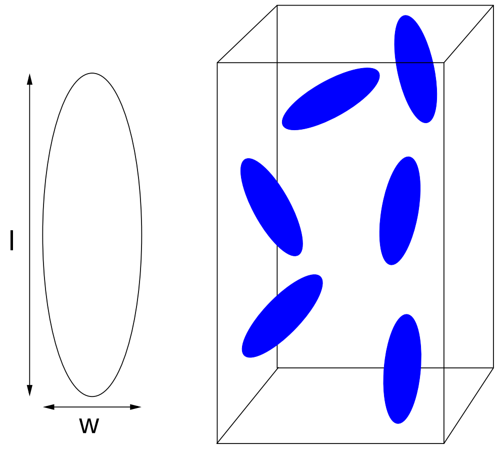

Figure 1.2: Ellipsoids of revolution.

1.3.2 Earlier Work

1.3.2.1 Equilibrium Results

The Monte Carlo (MC) simulation of hard ellipsoids began with the work of Vieillard-Baron [10] in 1972, whose algorithm for the detection of particle overlap is partly used even today, but whose results were otherwise limited by the computing power at the time. The efficiency of overlap detection, which is the bottle neck in the simulation, was improved by Perram and Wertheim [11, 12]. Using this, Frenkel and Mulder [1][3] established a phase diagram for hard ellipsoids in 1985; it has seen little modification since then.

Figure 1.3 shows the mentioned phase diagram. At low densities, there is an isotropic (or liquid) phase in which all degrees of freedom are disordered. At high densities, we have a solid phase, with orientational and positional order. If the ellipsoids are sufficiently anisometric ($l/w < 0.36$ or $l/w > 2.75$), a nematic phase exists between liquid and solid; there one has orientational order only: all ellipsoids point in nearly the same direction, but their positions are disordered as in the liquid phase. Finally, nearly spherical ellipsoids ($0.7 < l/w < 1.4$) can form a plastic solid phase (or rotator phase), with positional order and orientational disorder. The partially ordered phases are examples of liquid crystals, a vast subject of research [14]. Especially the nematic phase has been a chief motivation to study ellipsoids.

Hence, the focus of attention since the work of Frenkel and Mulder has been on the nematic phase and the isotropic-nematic transition [15, 16, 17]. These works

---

[3] Ref. 1 is a reprint; original paper: Ref. 13.

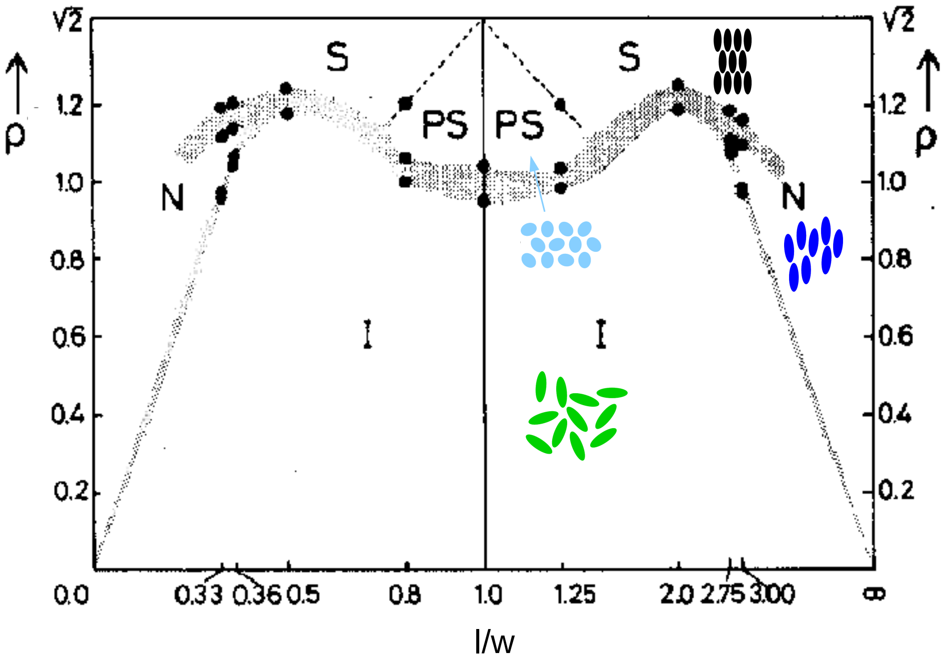

Figure 1.3: Frenkel and Mulder's phase diagram of hard ellipsoids (adapted from [1] with permission). At low densities, there is an isotropic phase (I, illustrated in green), in which all degrees of freedom are disordered. At high densities, we have a solid phase (S, black), with orientational and positional order. Beyond moderate anisometry, a nematic phase exists in between (N, dark blue), where one has orientational order only (all ellipsoids point in nearly the same direction). Finally, nearly spherical ellipsoids can form a plastic solid phase (PS, light blue), with positional order and orientational disorder. Grey regions mark coexistence.

determined the coexistence parameters more precisely and confirmed Onsager's theory for the nematic phase [7] for $l/w \gtrsim 3$, a common geometry in liquid crystals. Finally, we note that biaxial hard ellipsoids have also been studied [18, 19], which exhibit more liquid crystalline phases. For further reading we suggest the review articles [8, 9, 20]

The high-density phases, however, have not been investigated further. Knowledge of these phases is relevant for studies of elongated colloids in general, and it is critical for the study of nucleation and glassy dynamics in hard ellipsoids. The solid phases are one subject of the present investigation and, as we will see, they have surprises in store.

The crystal phase at high densities was *assumed* by Frenkel and Mulder [1] to be a solid of a certain structure. This step was necessary since crystallization is a rare event and in a simulation requires techniques unavailable at the time. It was argued that the chosen solid should at least be near the free-energy minimum due to its high symmetry. We close this section by describing how it is constructed (see Figure 1.4). We begin with an FCC system of spheres (top part of the Figure). An affine stretch by a factor x is performed in an arbitrary direction $\mathbf{z}$, in this case the [111] direction. Thereby we stretch both the lattice and the constituent particles. This transformation results in a crystal structure of ellipsoids of aspect ratio $l/w = x$, which are oriented along $\mathbf{z}$. Since filled space is stretched as much as empty space, the volume fraction of closest packing is the same as for the closest packing of spheres, $\phi = \pi/\sqrt{18} \approx 0.7405$. In the work of Frenkel and Mulder, this structure was then simulated at finite pressures. We will refer to it as stretched face-centered cubic (sFCC).

1.3.2.2 Close-Packing

Recently, Donev et al. [2] showed that close-packings of ellipsoids can be constructed which exceed the volume fraction for sFCC. They key was to take non-lattice periodic packings into account, i.e. packings in which a unit cell contains several ellipsoids at different orientations. $\phi \approx 0.7707$ can be achieved for $l/w \geqslant \sqrt{3}$ and $l/w \leqslant 1/\sqrt{3}$ if the unit cell contains two ellipsoids.

While this result concerns only close-packing, it is important for our thermodynamic results as the infinite-pressure limit. Therefore, we outline the construction in this section. Consider two layers of an FCC packing of spheres (see Figure 1.5a), a lower one (filled in light blue) and an upper one (transparent with dark outline). The red square highlights one face of the FCC. Such pairs of layers can be stacked to fill all space with FCC. The spheres are now deformed to ellipsoids as indicated by the red arrows, until they touch an additional two neighbors (n is the number of touching neighbors). The directions of deformation alternate perpendicularly from layer to layer. The ellipsoids remain at their lattice sites, as

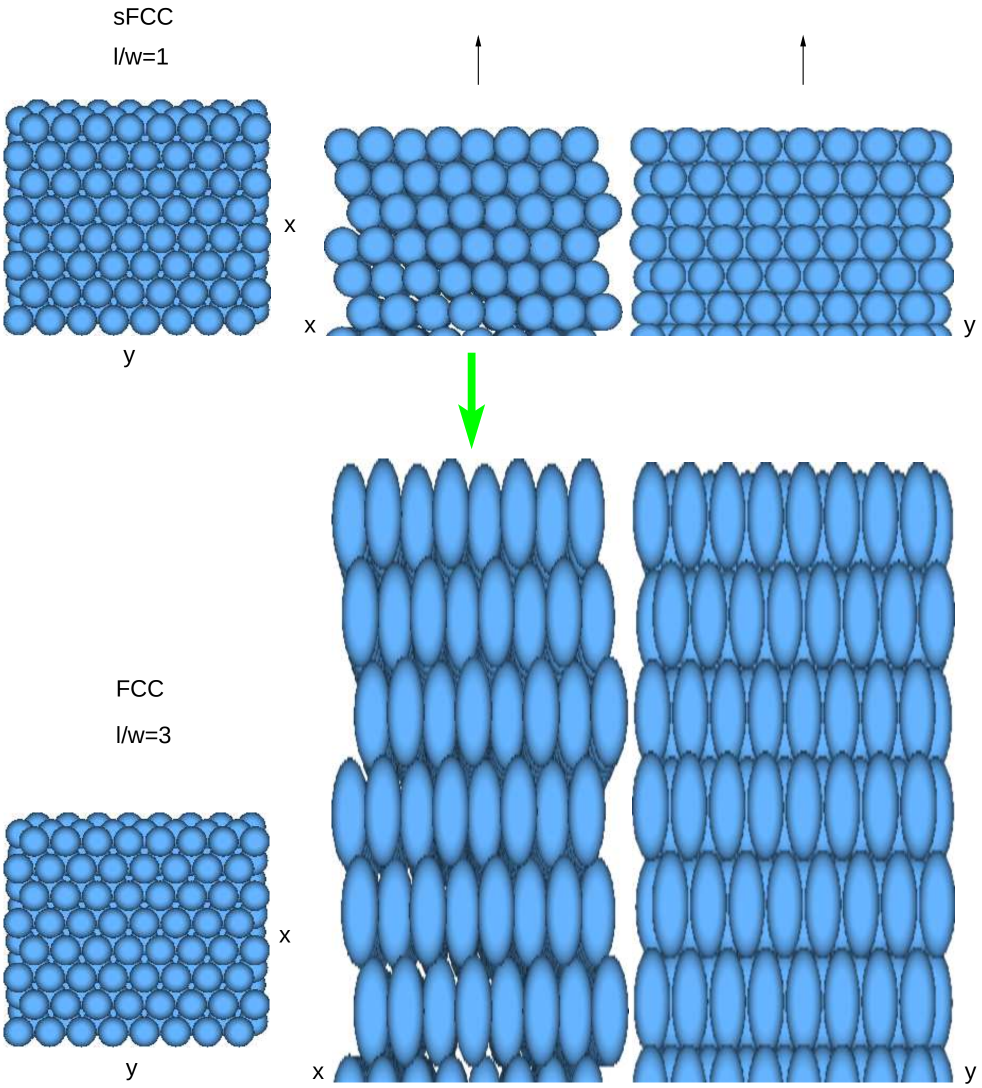

Figure 1.4: Construction of the sFCC crystal of ellipsoids as done in Ref. 1. The upper part shows an FCC crystal of spheres in the [111] direction (left) and in the two perpendicular directions labeled x and y (middle and right). The lower part shows the same structure after an affine stretch in the [111] direction. The volume fraction (at close-packing $\phi \approx 0.74$) remains unchanged.

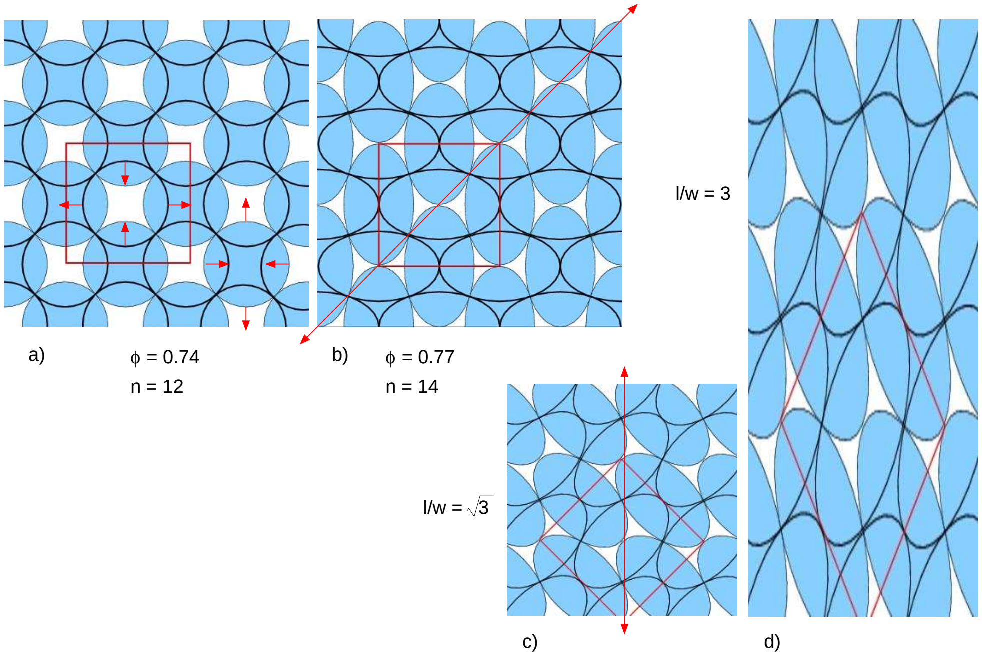

Figure 1.5: Construction of densest-known packings of ellipsoids [2]. In each sketch, two layers of particles are shown, a lower one (filled with light blue) and an upper one (transparent with dark outline). Such pairs of layers can be stacked to fill all space. a) Layers of FCC-packed spheres. The spheres are deformed to ellipsoids until they touch an additional two neighbors (*n* is the number of touching neighbors). The directions of deformation alternate perpendicularly from layer to layer. The ellipsoids remain at their lattice sites, as one can check with the red reference square. b) The resulting structure has the maximal volume fraction $\phi \approx 0.7707$. The diagonal line indicates a plane of symmetry in which an affine stretch keeps all ellipsoids congruent. c) Same as b), but rotated by 45^{o}. d) Same as c), but after an in-plane stretch to obtain ellipsoids with $l/w = 3$, packed at $\phi \approx 0.7707$.

one can check with the red reference square. As it happens, neighbors touching previously remain touching in the process. The resulting structure (Figure 1.5b) has the maximal volume fraction $\phi \approx 0.7707$. A hint towards this effect comes from the darker appearance of the illustration. The number of touching neighbors has increased to $n = 14$, also indicative of a denser packing. The aspect ratio $l/w = \sqrt{3}$ at this point, but higher values can be reached. The diagonal line indicates a plane of symmetry in which an affine stretch keeps all ellipsoids congruent. We recall that such a stretch leaves the packing fraction unchanged, since filled space is stretched as much as empty space. For clarity we now rotate the view by 45^{o} (move on to Figure 1.5c), and then perform an example stretch in the vertical direction to arrive at a packing of ellipsoids with $l/w = 3$, packed at $\phi \approx 0.7707$ (Figure 1.5d). To be precise, we note that the ellipsoids have become biaxial in the last step, since the stretch was not parallel to the long axis l. This can be remedied by performing an according stretch perpendicular to the plane of the page, so that the rotational symmetry is restored. In addition, one may perform a larger stretch perpendicular to the plane of the page, to obtain a densest packing of *oblate* uni-axial ellipsoids with $l/w = 1/3$. Depending on the in-plane stretch beforehand, densest packings of oblate ellipsoids $l/w \leqslant 1/\sqrt{3}$ are possible.

In addition to ordered close-packing of ellipsoids, the same group has been studying random close-packing of ellipsoids [21], partly in the search for a thermodynamically stable “glass”; i.e. a random packing which forms the ground state. This search is motivated by the fact that these packings achieve $\phi \approx 0.74$, not far from the ordered case. We understand a glass as a non-equilibrium state, however (Section 1.4).

1.3.2.3 Dynamics

The first molecular dynamics (MD) simulation of ellipsoids, and the first of all molecular, hard-particle fluids, was that of prolate hard ellipsoids with aspect ratios 2 and 3 by Allen and Frenkel [22]. The event-driven MD algorithm was developed by Allen, Frenkel, and Talbot [23], and it is the one we employ as well (Section 2.2.2). The investigation confirmed dynamic precursors of the isotropic-nematic transition, viz. the slowing-down of collective re-orientation indicative of the weakly first-order nature of the transition. Subsequently, Allen [24] showed with the same technique that in the nematic phase, diffusion along the long axis (prolate) or perpendicular to the short axis (oblate) becomes enhanced as the density is increased, before it is finally slowed down again. Further, Bereolos et al. [25] have studied diffusion, shear viscosity, and thermal conductivity in the isotropic region of the phase diagram, using the same MD. More results are reviewed in Ref. 20.

More recently, Letz et al. [3] have applied idealized molecular mode-coupling theory[4] (MMCT [26, 27, 28]) to the hard-ellipsoid fluid. Amending conventional mode-coupling theory (MCT [29]), MMCT takes orientational degrees of freedom into account. They predicted a glass transition of type B; that is, the long-time limit of the correlation functions jumps to a finite value as the transition line is crossed. Positional and even-parity orientational degrees of freedom become non-ergodic there. For nearly spherical ellipsoids this transition is driven by the cage effect, and is located inside the coexistence region between the isotropic fluid and the positionally ordered phases (solid and plastic solid). For more anisometric ellipsoids ($l/w < 0.5$ and $l/w > 2.0$) it is driven by pre-nematic order, i.e. by the formation of nematic domains, and located in the vicinity of the isotropic-nematic transition. In addition, a type-A glass transition was predicted, where the long-time limit of the correlators becomes finite continuously as the transition line is crossed. This transition affects only the odd-parity orientational degrees of freedom, i.e. 180° flips. It was predicted to occur in nearly-spherical ellipsoids, upon further compression in the plastic-solid regime of the equilibrium phase diagram.

De Michele et al. [30] have subsequently studied the dynamics of hard ellipsoids by molecular dynamics simulations. The simulated state points are mostly located in the isotropic region. The calculated isodiffusivity lines showed that the positional and orientational degrees of freedom are decoupled, since the positional isodiffusivity lines cross the orientational ones at nearly 90°. The behavior of correlation functions corroborated this decoupling. The self-part of the intermediate scattering function displayed slight stretching only when over-compressing nearly-spherical ellipsoids, while the second-order orientational correlator showed such stretching only for sufficiently anisometric particles, i.e. near the isotropic-nematic transition. But significant indicators of glassy dynamics, e.g. two-step relaxation in correlators or drastic slowing-down, were not seen as over-compression was weak. The last two studies are summarized in Figure 1.6.

Our study of glassy dynamics is motivated by the mentioned MMCT predictions of Letz et al. [3], and as a complement to the molecular dynamics investigation of de Michele et al. [30] which did not focus on the over-compressed fluid states.

1.3.2.4 Experiment

A celebrated experiment of granular ellipsoids is the study of random packings of M&M candies [21]. As mentioned in Section 1.3.2.2, the result was that random packings of ellipsoids can achieve packing fractions as high as $\phi \approx 0.74$, near the sFCC result.

As for colloidal suspensions, a procedure is available for making almost monodis-

---

[4] A brief introduction to mode-coupling theory is given in Section 1.4.2.

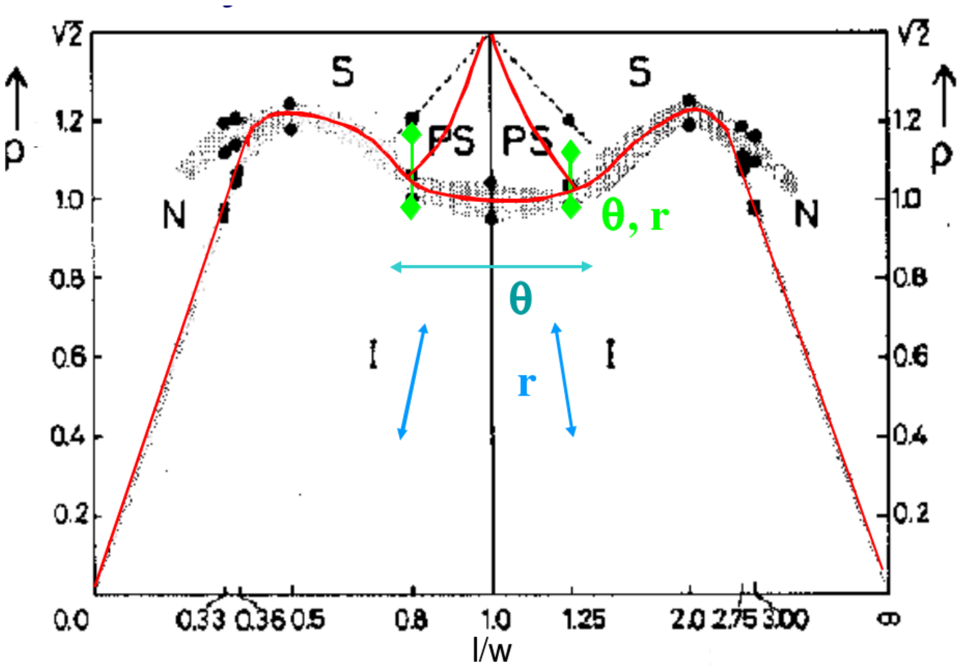

Figure 1.6: Equilibrium phase diagram of hard ellipsoids (adapted from [1] with permission) showing the Molecular Mode-Coupling Theory results of Letz et al. [3]. The red line marks a discontinuous (Type B) glass transition line, which follows the coexistence region delimiting the isotropic regime; and a continuous (Type A) transition line inside the plastic-solid region, affecting flipping modes only. In addition, the blue arrows indicate that positional freedom of the particles is governed by density, while the turquoise arrows indicate that orientational freedom is governed by anisometry. This decoupling was found by de Michele et al. [30]. In green we preview our result that both orientational and positional degrees of freedom are strongly slowed down by the indicated over-compression.

perse ellipsoids [31, 32], as follows: Polystyrene (PS) or poly(methyl-methacrylate) (PMMA) spheres, which are commercially available in narrow size ranges, are dispersed in a polyvinyl-alcohol (PVA) / water solution. The mixture is spread onto a flat surface, and upon drying (i.e. evaporation of the water), a PVA film results, which contains the particles. This film is then heated to $\approx 140^{o}$C, i.e. above the glass transition temperature of the particles. Stretching of the film then deforms the spheres to ellipsoids of controllable aspect ratio. After cooling, the film is dissolved in a water/alcohol mixture, and the solution centrifuged to sediment the particles. The liquid is decanted. Several more dispersions in water/alcohol and subsequent separations washes the remnant PVA from the particles. Figure 1.7 shows a micrograph of such particles prepared by the author during a visit to the group of Prof. Jan Vermant (Katholieke Universiteit Leuven). The spheres had an initial radius of $3.1\,\mu$m, and the aspect ratio of the resulting ellipsoids is estimated near $l/w = 3$.[5] Such ellipsoids of course are not exactly hard; but the use of steric stabilization, which avoids coagulation by attaching a polymer brush to the surface, allows for promisingly hard realizations.

The behavior of PS ellipsoids confined to water-air interfaces has been studied. This confinement occurs because the surface free-energy is significantly lower for the ellipsoid-air and ellipsoid-water interfaces than for the water-air interface. The presence of the particles at the interface thus lowers the total free energy of such a system. The ellipsoids are not fully immersed in water, and the anisometry of the particles brings about a deformation of the interface, inducing an effective interaction (capillary forces) tending to minimize the deformation. The surface deformation and its consequences has been studied both experimentally [33] and theoretically [34]. In addition, the packing of ellipsoids at high surface coverages was studied experimentally [35].

Furthermore, 3D structural properties of a sedimentation of these particles have been successfully characterized [36], showing nematic domains. Fluorescently labeled PMMA particles were imaged by confocal microscopy. Recently, this technique has been extended to dynamics [37]. Both translational and rotational motion could be followed. A study of glassy dynamics in this fashion seems promising, so does the investigation of the equilibrium phases of colloidal ellipsoids in bulk.

---

[5] It is thus demonstrated that a theoretician can perform this procedure after some training.

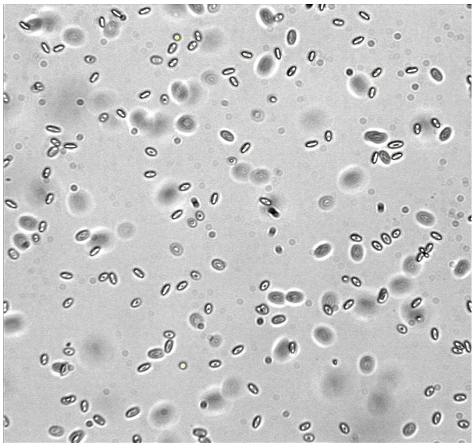

Figure 1.7: Micrograph of polystyrene ellipsoids ($l/w \approx 2.5$, $w \approx 3\,\mu$m), prepared by the author during a visit to the group of Prof. Jan Vermant (Katholieke Universiteit Leuven).

1.4 Glasses

1.4.1 Overview

Glasses are familiar materials in every-day life. The reader may have visited factories or artists forming shapes from the glowing hot, viscous mass which then somehow freezes in the given shape when allowed to cool, to finally yield the useful and beautiful products we know.

From the scientific perspective, glasses form a peculiar “phase” of matter in that they are solid and liquid at the same time. They are solid in appearance, but their microscopic structure is indistinguishable from their liquid phase. It is their dynamical properties which make the difference. Viscosity and relaxation times are 12-14 *orders of magnitude* larger than those of liquids, after only a modest change in temperature (e.g. a factor of three). As a consequence, glasses are non-equilibrium systems, since even slow cooling from the liquid state eventually occurs too fast for the system to adjust.

There are various definitions of the glass transition and associated transition temperature:

- the system falls out of equilibrium during cooling
- the viscosity has reached 10^{13} Poise
- special conditions in theoretical models arise, e.g. the arrest of dynamics in Mode Coupling Theory.

Typically (but not necessarily) glassy characteristics develop upon supercooling the liquid below its freezing point. The competing mechanism is crystallization. Whether or not a system remains amorphous during cooling depends on material properties and the cooling rate. If the system crystallizes readily, rapid cooling (a “quench”) is required to reach a glass state. In archetypal glass formers, such as silica mixtures, the slowing-down becomes significant well before the freezing point is reached, so moderate cooling rates suffice.

If the cooling rate is slow enough, and if crystallization does not intervene, glassy dynamics may be studied in quasi-equilibrium. The term *glassy dynamics* refers to the significant slowing-down of diffusion and relaxation (as compared to the microscopic time scale[6]), non-exponential relaxation, and their strong dependence on a control parameter. In our case, density (or volume fraction) is the control parameter, rather than temperature.

A concise and accessible introduction to glasses is given by Kob [38].

1.4.2 The Mode-Coupling Theory of the Glass Transition

The dynamics of glassy systems and the glass transition in particular have been the subject of intense research for the past 25 years. However, many phenomena are still poorly understood. The only microscopic theory so far is the mode-coupling theory (MCT) [39]. Our study of the dynamics will include tests of this theory. We give here a brief introduction to MCT. For more details see the review articles [40, 38, 41, 42, 43]. MCT has been extended to orientational degrees of freedom [26, 27, 28], called Molecular Mode-Coupling Theory (MMCT).

We will first discuss MCT with temperature as the control parameter, because this is the more common situation; but glassy dynamics may just as well be induced by over-compression, rather than supercooling. At the end of this section, we will point out how all results apply to our situation, where density, or volume fraction, is the control parameter. Moreover, for simplicity we will first ignore orientational degrees of freedom, and discuss their inclusion at the end as well.

A remarkable feature of the dynamics of supercooled liquids is the stark increase of typical relaxation times τ upon cooling the liquid from its liquid state to the glass transition temperature T_g.[7] In the liquid state, τ is on the order of ps; near T_g, it may well be hundreds of seconds. But this slowing down is accompanied by no significant change in structure; e.g. there is no diverging length scale as in a second-order phase transition. MCT describes this slowing down as strongly increasing nonlinear feedback effects in the microscopic dynamics, whereby par-

---

[6] That time scale on which local processes occur (e.g. particle vibrations).

[7] T_g is here defined (arbitrarily) as the temperature at which the viscosity has reached 10^{13} Poise.

ticles are trapped in *cages* formed by their nearest neighbors. We emphasize that MCT is an equilibrium theory (ignoring crystallization); it does not apply to systems which have fallen out of equilibrium during cooling.

The appropriate observable for the slowing down of the relaxation dynamics in glassy systems is the *intermediate scattering function:*

$$F(\mathbf{q},t) = \frac{1}{N}\langle \rho^*(\mathbf{q},t)\rho(\mathbf{q},0)\rangle \quad \text{where} \quad \rho(\mathbf{q},t) = \sum_{i=1}^{N} \exp(i\mathbf{q}\cdot\mathbf{r}_i(t)), \tag{1.4}$$

where $\mathbf{q}$ is the wave vector, N the number of particles and $\mathbf{r}_i(t)$ the position of the ith particle at time t. $F(\mathbf{q},t)$ is a density-density correlator which is accessible in scattering experiments and may be calculated from simulation. It is therefore of practical interest.[8]

Starting from the Liouville equation, and using the Mori-Zwanzig projection operator formalism, one may derive an equation of motion for $F(\mathbf{q},t)$. For isotropic systems, this equation of motion, called *Mori–Zwanzig equation*, may be written as

$$\ddot{F}(q,t) + \Omega^2(q)F(q,t) + \int_0^t \underbrace{\left[M^0(q,t-t') + \Omega^2(q)m(q,t-t')\right]}_{\text{memory kernel}} \dot{F}(q,t')dt' = 0, \tag{1.5}$$

where $\Omega(q)$, a microscopic frequency, depends on the static structure factor $S(q)$ (see Section 4.2.2) via

$$\Omega^2(q) = \frac{q^2 k_B T}{mS(q)}, \tag{1.6}$$

where m is the mass of the particles and k_B Boltzmann's constant. So far the equation of motion for $F(q,t)$ is exact; the problem has been merely restated in a form which makes the following approximations possible.

The *memory kernel* consists of two parts: $M^0(q,t)$ describes the dynamics at short (i.e. microscopic) times and is important only near the triple point; $m(q,t)$ becomes important when the liquid is strongly supercooled. Assuming, then, that the only relevant contribution of $M^0(q,t)$ occurs at $t = 0$, we approximate

$$M^0(q,t) = \nu(q)\delta(t). \tag{1.7}$$

Eq. (1.5) then becomes that of a damped harmonic oscillator with the addition of a retarded friction term proportional to $m(q,t)$.

---

[8] We introduce it in detail in Section 4.3.2.1.

In the *factorization approximation* (see Götze [44]), $m(q,t)$ is taken to be a quadratic form of the correlators $F(q,t)$, i.e.

$$m(q,t) = \sum_{\mathbf{k}+\mathbf{p}=\mathbf{q}} V(\mathbf{q};\mathbf{k};\mathbf{p}) F(k,t) F(p,t). \tag{1.8}$$

This yields the so-called *mode-coupling equations* (first proposed by Bengtzelius et al. [39]), a closed set of coupled equations for $F(q,t)$, the solution of which is the full time dependence of the intermediate scattering functions. The vertices $V(\mathbf{q};\mathbf{k};\mathbf{p})$ can be calculated from $S(q)$ and static three-point correlation functions.

In this *idealized* version of MCT, it is believed that these equations (Eq. (1.5) through Eq. (1.8)) give a correct (self-consistent) description of the dynamics on time scales while particles typically remain trapped in *cages* formed by surrounding particles; and at long time scales, on which they typically manage to escape these cages and exhibit diffusive motion. Particles will not escape such a cage unless their destination cage has been vacated, which will not be the case before *its* inhabitant has found a new cage to go to, etc. Therefore, the motion of the particles is collective, and so the description of motion must incorporate feedback. The mode-coupling approximation (Eq. (1.8)), in conjunction with Eq. (1.5), satisfies that requirement [45].

The quantities $\Omega^2(q)$, $M^0(q,t)$ and $V(\mathbf{q};\mathbf{k};\mathbf{p})$ depend on temperature, the major influence ultimately stemming from $S(q)$. Correspondingly, lower temperature leads to longer times before escape from a cage occurs. We will see momentarily that in (idealized) MCT, one may pinpoint a critical temperature T_c at which particles hinder each other so much as to produce structural arrest of the system.

Due to the complexity of the mode-coupling equations, one must resort to numerical approaches. However, the situation improves significantly if we make another approximation, whereby the structure factor is replaced by a δ–function at its main peak; we call this position q_0. The mode-coupling equations then reduce to just one equation at q_0, all others vanish identically. Replacing $\Phi(t) = F(q_0,t)/S(q_0)$, we find

$$\ddot{\Phi}(t) + \Omega^2 \Phi(t) + \nu \dot{\Phi}(t) + \Omega^2 \int_0^t m\left[\Phi(t-t')\right] \dot{\Phi}(t') dt' = 0. \tag{1.9}$$

Here $m[\Phi]$ is a polynomial of low order in Φ. The temperature dependence of $S(q)$ enters here via a temperature dependence of the coefficients of the polynomial $m[\Phi]$. An equation obtained in this fashion is called *schematic model.* The appeal of such models is that the general features of their solutions, asymptotic laws in particular, are the same as the ones of the full MCT-equations. However, since they are significantly simpler, they facilitate a general overview on the possible time dependence of the solutions.

Now, if the nonlinear feedback, given by the kernel $m[\Phi]$, exceeds a certain threshold, the solution to Eq. (1.9), hence $F(q_0,t)$, no longer decays to zero (the system has become nonergodic). It is this condition which is identified with the glass transition; it occurs at a critical temperature T_c.

Before turning to the predictions of *idealized* MCT, we discuss an important limitation. Upon reaching very low temperatures (i.e. close to T_c), the dynamic behavior departs from that described by idealized MCT because *hopping processes* start to become important. They are processes whereby cages are left in an activated fashion, leading to structural relaxation, and idealized MCT neglects these. The result is that even at low T, the system is still ergodic, and correlators eventually decay to zero. The domain to which idealized MCT applies is thereby limited; it ranges from the liquid regime, where relaxation times are on the order of ps, down to tens of ns in the supercooled state, before hopping processes become important.

The so-called *extended version* of MCT incorporates such hopping processes; due to complications, however, the treatment does not yet include as much detail. We will focus our attention to idealized MCT and take note of hopping when necessary.

Let us turn to the predictions (for more detail see [42, 41, 46, 47, 44, 43]). Most of them concern the decay of correlation functions. In Figure 1.8 we demonstrate the general behavior of such functions. We distinguish three regimes: the *microscopic* regime, a time scale during which microscopic relaxation takes place; since it strongly depends on the details of microscopic interactions, hardly any general predictions are possible.[9] Next comes the β*-relaxation* regime, during which dynamics are dominated by caging - visible as a plateau which increases in width towards low temperatures; and the α*-relaxation* regime, which describes the decay of the correlators from the plateau to zero. One of the main predictions of MCT is the existence of these three regimes; and it makes detailed predictions about the latter two, as follows.

- There exists a critical temperature T_c, and in its vicinity the self-diffusion constant D and the inverse of the α–relaxation time τ vanish according to[10]

  $$D \propto \tau^{-1} \propto (T - T_\mathrm{c})^{\gamma}, \tag{1.10}$$

  where $\gamma > 1.5$ is universal for the system (i.e. the same for all correlators). Note that the following predictions all assume proximity of T_c.

---

[9] The microscopic regime is preceded by the *ballistic* regime, during which particles move with essentially constant velocity and (hence) decay of correlators is quadratic. The ballistic regime is absent in colloidal systems, where Brownian motion occurs.

[10] The α–relaxation time τ may be defined as the time when the correlator has decayed to 0.1 or another fixed value within the α–relaxation regime.

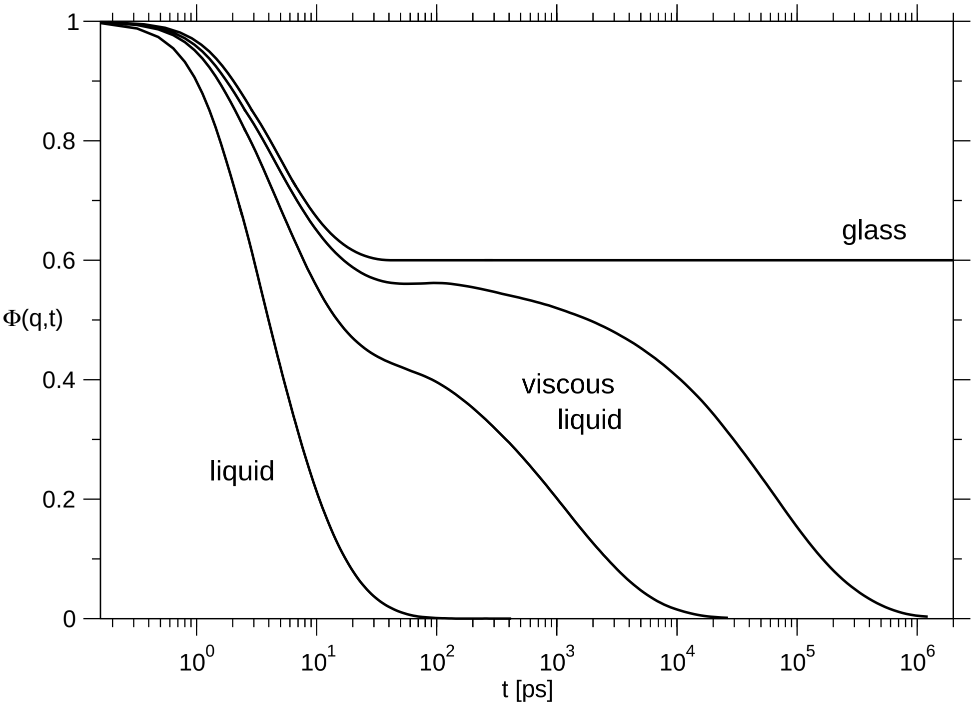

Figure 1.8: Schematic time dependence of correlators, for liquid to supercooled regimes and the glass case (high to low temperatures, or low to high densities).

- In the β- and α-relaxation regimes, the correlators obey the so-called time-temperature superposition principle (TTSP), which states that the correlators map onto a single curve by rescaling the time dependence using t/τ (τ being the α–relaxation time); that is,

$$\Phi(t) = \Psi(t/\tau(T)). \tag{1.11}$$

- Numerical predictions from MCT show that the *Kohlrausch–Williams–Watts function* may be used as a fit function for the master curve Eq. (1.11), with an effective exponent β

$$\Phi(t) = A\exp\left(-(t/\tau(T))^{\beta}\right), \tag{1.12}$$

  where β is the *stretching parameter.* It depends on the correlator (in particular, on q in $F(\mathbf{q},t)$).

- All correlation functions' α–relaxation times diverge according to a power law with exponent γ (see Eq. (1.10)). This exponent is related to two parameters a and b concerning the β–relaxation regime (discussed below):

$$\gamma = 1/(2a) + 1/(2b). \tag{1.13}$$

  Thus, from the temperature dependence of the α–relaxation time we can learn about the time dependence of the relaxation in the β-relaxation regime and vice versa. a and b are related to one another via

$$\Gamma^2(1-a)/\Gamma(1-2a) = \Gamma^2(1+b)/\Gamma(1+2b) = \lambda \tag{1.14}$$

  so that knowledge of one of these three exponents yields the other two. λ is called the *exponent parameter*.

- In the β–relaxation regime the correlators may be written as

$$\Phi(q,t) = f_q^c + h(q)g(t/\tau), \tag{1.15}$$

  where f_q^c, the height of the plateau at the transition, is termed *non-ergodicity parameter*. $h(q)$ is an amplitude. $g(t/\tau)$ does *not* depend on q; this entails the *factorization property.* Defining [48]

$$R(t) = \frac{\Phi(q,t) - \Phi(q,t'')}{\Phi(q,t') - \Phi(q,t'')} \tag{1.16}$$

  one finds that all q-dependence has been removed. This operation can be directly applied to $F(\mathbf{q},t)$ data, allowing one to check whether the factorization property holds: if it does, all $F(\mathbf{q},t)$ will fall onto a master curve.

- The late β–relaxation regime (when the curve slowly begins to leave the plateau) and the early α–relaxation regime in the intermediate scattering functions may be described by
$$\Phi(q,t) = f_q^c - h_q^{(1)} t^b + h_q^{(2)} t^{2b}. \tag{1.17}$$
f_q^c is again the non-ergodicity parameter. When dealing with coherent[11] intermediate scattering functions, f_q^c is also called the *Debye-Waller factor*; in incoherent intermediate scattering functions, it is the *Lamb-Mößbauer factor.* $h_q^{(1)}$ is referred to as *critical amplitude.* All quantities subscribed with q depend only on q, not on time t. The first two terms in Eq. (1.17) are called *von Schweidler law,* to which the last term is a leading-order correction; b is the *von Schweidler exponent,* and according to MCT it is independent of type of correlator (hence independent of q).

- The time scale of the β–relaxation regime (its width) is predicted by MCT to diverge as
$$t \propto |T - T_\mathrm{c}|^{1/2a}, \tag{1.18}$$
when T is close to T_c, and we have $0 < a < 1/2$. Light scattering experiments have confirmed the validity of Eq. (1.18) [49, 50].

- The relaxation dynamics are, apart from an overall shift in time scales, independent of the microscopic dynamics (e.g. Brownian vs. Newtonian dynamics). Hence, the above predictions are independent thereof.

In molecular systems, where there are orientational degrees of freedom, one can define orientational analogues of the intermediate scattering functions (see also Section 4.3.2.2),
$$L_i(t) = \langle P_i \{\cos[\theta(t)]\}\rangle \tag{1.19}$$
where P_i is the ith Legendre polynomial, and $\theta(t)$ is the angle between a molecule's orientation at time t and its initial orientation. These orientational correlation functions play the same role as the intermediate scattering functions, and the above MCT predictions apply analogously, if we bear in mind that q is replaced by the discrete index i. This analogy is limited, however: It is possible that orientational degrees of freedom are not affected by a positional glass transition, or even that different values of i are affected by separate glass transitions (see Section 1.3.2.3). This concerns the factorization property and the degree to which exponents are system-universal.

---

[11] For the distinction between coherent and incoherent intermediate scattering functions, see Section 4.3.2.1.

In hard-particle systems, temperature is a trivial, overall scaling parameter. The only relevant quantity for glassy dynamics is here particle density, or equivalently, volume fraction. To apply the above predictions to this case, supercooling translates to over-compression, and one must simply replace all expressions $T - T_c$ by $\phi_c - \phi$, where ϕ_c is the MCT critical volume fraction.

Many of the qualitative predictions of MCT have been confirmed for supercooled liquids. See, for example, [51, 52, 53, 54, 55, 56].

Chapter 2

Simulation - Theory and Technique

We have employed two techniques of simulation in our work, Monte Carlo simulation and molecular dynamics simulation. This allowed us to compare the two methods and test a MCT prediction about such a comparison (Sections 1.4.2 and 4.3).

Since we are interested in the bulk properties of our systems, all simulations were done with *periodic boundary conditions* to minimize boundary effects. The simulated system is perpetuated periodically in all directions by images of itself. A particle leaving the system on the right-hand side re-enters it on the left-hand side, and so on. Each particle interacts either with the original of other particles in the box or with the closest image in a neighboring image box, whichever is closer. The absolute position of the particles is irrelevant in such a setup [57].

2.1 Monte Carlo Simulation (MC)

2.1.1 General Features

In Monte Carlo simulation as introduced by Metropolis et al. [58], phase space is traversed, or *sampled*, by a random walk. The underlying random process is a Markov process, i.e. the $(n+1)$th state is a function of the nth state only. The next state is tested by a trial move in one or more phase space coordinates, and in the canonical ensemble accepted with probability

$$\mathrm{acc}_{n\to n+1} = \min(1, \exp[-(E_{n+1} - E_n)/k_\mathrm{B}T]) \tag{2.1}$$

where E_i is the energy of state i, k_B Boltzmann's constant and T the temperature. In practice, a random number is generated in the interval $[0,1]$, and the move is accepted if the number is smaller than $\mathrm{acc}_{n\to n+1}$. Eq. (2.1) is also called acceptance criterion or acceptance rule.

Properties of interest are monitored on the way and their average or full distribution is the final result. Note that the value of an integral, e.g. the volume of phase space (hence the partition function) *cannot* be evaluated in this way.

The sampling must be with known or with no bias in order to produce meaningful results[1]. This concerns the choice of trial move and the acceptance criterion Eq. (2.1). A sufficient condition is to maintain *detailed balance*, i.e. the reverse of a move must occur with equal probability. A deliberate bias is at the heart of the method, since one can restrict the sampling to the statistically relevant regions of phase space (*importance sampling*); in fact the above acceptance criterion implies a bias which reproduces the Boltzmann distribution of energies. The implementation of importance sampling also entails that the simulation must first equilibrate, i.e. reach the important parts of phase space, before calculations can begin.

The classical way to generate trial moves proceeds by first picking, at random, a small subset of degrees of freedom; e.g. one particle's position. For the position, a displacement vector is chosen from a box. The size of this box is important for the simulation's efficiency, and is held fixed to yield an acceptance rate of typically 20% to 40%, depending on the computational bottlenecks of particle interactions. The same pattern is applied to other degrees of freedom, such as orientational moves for molecules or box-shape variations; more details are given below.

A central feature of the Monte Carlo method is the use of more elaborate moves which take the system through phase space efficiently, despite the presence of barriers. A move which represents a large step in phase space (e.g., a cluster move), but still achieves sufficient acceptance rates, can significantly expedite a simulation.

For a thorough introduction to Monte Carlo see Frenkel and Smit [57] or Landau and Binder [59].

2.1.2 Constant-Pressure-and-Tension Ensemble

Monte Carlo simulation of this ensemble has been first described by Najafabadi and Yip [60] and in more detail by Yashonath and Rao [61]. It is based on the corresponding molecular dynamics invented by Parrinello and Rahman [62]. The essence is that the simulation box may vary in size and shape (take a preview of Figure 2.1). This is critical for the equilibration of solids, where the box shape has a direct influence on the lattice geometry. If oblique shapes are not allowed, the solid will in general be under stress.

---

[1] As David Landau would have it, "... and unless you're very careful, you will get results, it's just they don't mean anything."

2.1.2.1 Partition Function

For the case relevant to us, namely zero tension, the configurational part of the partition function in the named ensemble may be written as

$$\begin{aligned} Z(N,P,T) &= \int_{-\infty}^{\infty} dh_{11}\cdots dh_{33} \int_{\mathbf{H}} d\mathbf{r}^N \int_{4\pi} d\mathbf{u}^N \cdot \\ &\quad \exp\{-[U(\{\mathbf{r}_i\},\{\mathbf{u}_i\})+PV(\mathbf{H})]/k_{\mathrm{B}}T\} \end{aligned} \tag{2.2}$$

where we have ignored the prefactors $(N!\lambda^{6N})^{-1}$ which have no influence on the equilibrium behavior. h_{ij} are all 9 elements of the matrix $\mathbf{H}$ describing the box shape. Each column vector in $\mathbf{H} = [\mathbf{h}_1\mathbf{h}_2\mathbf{h}_3]$ corresponds to one box edge, in the same way as unit cell vectors correspond to the edges of the unit cell in a crystal lattice. Hence, $\mathbf{H}$ completely specifies the box. It also follows that the box volume $V = \det\mathbf{H}$. The integral over particle coordinates is over the box as determined by $\mathbf{H}$.

For convenience and clarity we introduce scaled particle coordinates $\mathbf{s}$ so that $\mathbf{r} = \mathbf{H}\mathbf{s}$. $\mathbf{s}$ is in the unit cube, and $\mathbf{H}$ provides the mapping to the simulation box. Eq. (2.2) becomes

$$\begin{aligned} Z(N,P,T) &= \int_{-\infty}^{\infty} dh_{11}\cdots dh_{33} \int_{0}^{1} d\mathbf{s}^N \int_{4\pi} d\mathbf{u}^N \cdot \\ &\quad \exp\{-[U(\{\mathbf{s}_i\},\mathbf{H},\{\mathbf{u}_i\})+PV(\mathbf{H})]/k_{\mathrm{B}}T\}(\det\mathbf{H})^N \\ &= \int_{-\infty}^{\infty} dh_{11}\cdots dh_{33} \int_{0}^{1} d\mathbf{s}^N \int_{4\pi} d\mathbf{u}^N \cdot \\ &\quad \exp\{-[U(\{\mathbf{s}_i\},\mathbf{H},\{\mathbf{u}_i\})+PV(\mathbf{H})]/k_{\mathrm{B}}T + N\ln V(\mathbf{H})\} \\ &= \int_{-\infty}^{\infty} dh_{11}\cdots dh_{33} z_{PT}^{-V(\mathbf{H})} Z_0(N,\mathbf{H},T) \end{aligned} \tag{2.3}$$

where we have introduced the isochoric partition function

$$Z_0(N,\mathbf{H},T) \equiv \int_{0}^{1} d\mathbf{s}^N \int_{4\pi} d\mathbf{u}^N \exp\{-U(\{\mathbf{s}_i\},\mathbf{H},\{\mathbf{u}_i\})/k_{\mathrm{B}}T + N\ln V(\mathbf{H})\}$$

and defined a “fugacity” $z_{PT} = e^{P/k_{\mathrm{B}}T}$ for brevity.

In principle, Eq. (2.3) can be the starting point for the simulation. However, it is from the programming point of view more convenient to keep $\mathbf{H}$ upper-triangular[2], which is identical to fixing the global orientation of the box. Given

---

[2] Another possibility is to keep $\mathbf{H}$ symmetric.

the orientational degeneracy of configurations, this should pose no problem. $\mathbf{h}_1$ is then parallel to the x-axis, and $\mathbf{h}_2$ resides in the xy-plane. The expression for the volume simplifies to $V = \det \mathbf{H} = h_{11}h_{22}h_{33}$.

We would like to point out a subtlety in this step which has gone unnoticed in the literature. The proper removal of orientational degeneracy is integrating it out. For $\mathbf{h}_1$ this implies a change of coordinates to spherical ones $(r_{h1}, \theta_{h1}, \phi_{h1})$, followed by integration over the angular variables. Eq. (2.3) becomes[3]:

$$Z(N,P,T) = 4\pi \int_0^\infty dr_{h1} \int_{-\infty}^{\infty} dh_{12}dh_{13}dh_{22}dh_{23}dh_{32}dh_{33}r_{h1}^2 z_{PT}^{-V(\mathbf{H})} Z_0(N,\mathbf{H},T)$$

Now we may fix $\mathbf{h}_1$ to be parallel to the x-axis, i.e. we may replace r_{h1} with h_{11} (and drop the prefactor):

$$Z(N,P,T) = \int_0^\infty dh_{11} \int_{-\infty}^{\infty} dh_{12}dh_{13}dh_{22}dh_{23}dh_{32}dh_{33}h_{11}^2 z_{PT}^{-V(\mathbf{H})} Z_0(N,\mathbf{H},T) \quad (2.4)$$

As of now, the system is still free to rotate about the x-axis. This remaining degeneracy is integrated out in $\mathbf{h}_2$. To do so, $\mathbf{h}_2$ must be changed to cylindrical coordinates about the x-axis, i.e. $(h_{12}, \rho_{h2}, \phi_{h2})$. Angular integration follows. Eq. (2.4) now reads

$$Z(N,P,T) = 2\pi \int_0^\infty dh_{11}d\rho_{h2} \int_{-\infty}^{\infty} dh_{12}dh_{13}dh_{23}dh_{33}h_{11}^2 \rho_{h2} z_{PT}^{-V(\mathbf{H})} Z_0(N,\mathbf{H},T)$$

Now we may fix $\mathbf{h}_2$ into the xy-plane, i.e. we may replace ρ_{h2} with h_{22} (and drop the prefactor):

$$Z(N,P,T) = \int_0^\infty dh_{11}dh_{22} \int_{-\infty}^{\infty} dh_{12}dh_{13}dh_{23}dh_{33}h_{11}^2 h_{22} z_{PT}^{-V(\mathbf{H})} Z_0(N,\mathbf{H},T) \quad (2.5)$$

It is these factors $h_{11}^2 h_{22}$ which have been, to our knowledge, overlooked[4]: in the literature, the matrix $\mathbf{H}$ is simply restricted to be triangular or symmetric, without regard to the implied integration over the orientational degeneracy. But the resulting weight factors $h_{11}^2 h_{22}$ must be properly included into the acceptance criterion (below) for a bias-free simulation. Their presence favors larger values of

---

[3] In principle, $\mathbf{h}_2$ and $\mathbf{h}_3$ should be changed to variables relative to $\mathbf{h}_1$. But since the integrals in $\mathbf{h}_2$ and $\mathbf{h}_3$ are over all space, ignoring this has no consequences. The integration over the angular part in $\mathbf{h}_1$ nevertheless implies the integration over global orientations of the whole system.

[4] Or their analogues when $\mathbf{H}$ is kept symmetric.

h_{11} and h_{22} in the partition sum. One can see that this must be so: The phase space volume orthogonal to h_{11}, which we integrated out, is the surface area swept out by $\mathbf{h}_1$ if it was still free to rotate. Hence, larger magnitudes of $\mathbf{h}_1$ would be visited more often if the box was still free to rotate. Now that it is fixed, we must favor larger magnitudes with the given weight factor. The analogous argument applies to h_{22}.

There is an equivalent set of configurations for positive and negative h_{33}. We may remove this degeneracy, which is to keep h_{33} nonnegative. Eq. (2.5) picks up an irrelevant factor of 2.

Next, we express the remaining off-diagonal terms as follows:

$$\begin{aligned} h_{12} &= g_{12}h_{22} \\ h_{13} &= g_{13}h_{33} \\ h_{23} &= g_{23}h_{33} \end{aligned} \tag{2.6}$$

Eq. (2.5) then becomes

$$\begin{aligned} Z(N,P,T) &= \int_0^\infty dh_{11}dh_{22}dh_{33} \int_{-\infty}^\infty dg_{12}dg_{13}dg_{23} \cdot \\ &\quad h_{11}^2 h_{22}^2 h_{33}^2 z_{PT}^{-V(\mathbf{H})} Z_0(N,\mathbf{H},T) \\ &= \int_0^\infty dh_{11}dh_{22}dh_{33} \int_{-\infty}^\infty dg_{12}dg_{13}dg_{23} \cdot \\ &\quad V(\mathbf{H})^2 z_{PT}^{-V(\mathbf{H})} Z_0(N,\mathbf{H},T) \end{aligned} \tag{2.7}$$

The advantage of introducing the variables g_{ij} lies in the separation of size variables and pure shape variables. h_{ii} specify the separation of box walls, while g_{ij} specify box shear. For example, $g_{12} = h_{12}/h_{22} = dx/dy$ is the change in x-direction of box edge $\mathbf{h}_2$ as one moves along the y-direction. The same separation occurred in the process of integrating out orientational degeneracy, as the angular variables also no longer carried size information. It is reassuring that the corresponding factors h_{ii} in Eq. (2.7) combine to factors of volume.

The set of variables h_{ii} and g_{ij} are also the relevant parameters in crystal lattices, associated with distinct moduli of elasticity (bulk and shear, respectively), and we anticipate that they will require individual MC move sizes.

Finally, we follow the literature in changing from integrating (hence sampling) over dh_{ii} to $d\ln h_{ii}$:

$$\begin{aligned} Z(N,P,T) &= \int_{-\infty}^{\infty} d\ln h_{11} d\ln h_{22} d\ln h_{33} dg_{12} dg_{13} dg_{23} \cdot \\ & \quad h_{11}h_{22}h_{33}V(\mathbf{H})^2 z_{PT}^{-V(\mathbf{H})} Z_0(N,\mathbf{H},T) \\ &= \int_{-\infty}^{\infty} d\ln h_{11} d\ln h_{22} d\ln h_{33} dg_{12} dg_{13} dg_{23} \cdot \\ & \quad V(\mathbf{H})^3 z_{PT}^{-V(\mathbf{H})} Z_0(N,\mathbf{H},T) \end{aligned}$$

The advantage is here one of efficiency. The sampling will naturally occur in smaller step sizes of the original h_{ii} for smaller volumes; this is desirable since smaller volumes, associated with larger pressures in the system, make these degrees of freedom stiffer. Once more we appreciate the advantage of keeping size and shear apart. The final form of the partition sum is then

$$\begin{aligned} Z(N,P,T) &= \int_{-\infty}^{\infty} d\ln h_{11} d\ln h_{22} d\ln h_{33} dg_{12} dg_{13} dg_{23} \int_0^1 d\mathbf{s}^N \int_{4\pi} d\mathbf{u}^N \cdot \\ & \quad \exp\left\{-\left[U(\{\mathbf{s}_i\},\mathbf{H},\{\mathbf{u}_i\}) + PV(\mathbf{H})\right]/k_\mathrm{B}T + (N+3)\ln V(\mathbf{H})\right\} \end{aligned} \tag{2.8}$$

and the matrix $\mathbf{H}$ reads

$$\mathbf{H} = \begin{bmatrix} h_{11} & h_{22}g_{12} & h_{33}g_{13} \\ & h_{22} & h_{33}g_{23} \\ & & h_{33} \end{bmatrix} \tag{2.9}$$

All weighting in Eq. (2.8) is absorbed into the exponential, so we can immediately write down the acceptance rule:

$$\mathrm{acc}_{n\to n+1} = \min(1, \exp\left\{-\left[U_{n+1} - U_n + P(V_{n+1} - V_n)\right]/k_\mathrm{B}T + (N+3)\ln\frac{V_{n+1}}{V_n}\right\}) \tag{2.10}$$

If we keep $g_{ij} = 0$ and $h_{11} = h_{22} = h_{33}$, the present results reduce to those of the known constant-pressure ensemble—apart from the factor $(N+3)$ where $(N+1)$ is found instead [57], "+1" coming from sampling $d\ln V$. We show in Appendix A that $(N+3)$ is the correct result derived from the present, more general basis. This correction, of order $1/N$, surely does not render useless all simulations which used $(N+1)$. We find it important for the understanding of the derivation, and indeed in small simulations the difference may be noticeable.

Finally, we write down the simpler hard-particle results. Eq. (2.8) becomes

$$\begin{aligned} Z(N,P,T) \quad = \quad & \underset{\text{no overlap}}{\int_{-\infty}^{\infty}\int_{0}^{1}\int_{4\pi}} d\ln h_{11} d\ln h_{22} d\ln h_{33} dg_{12} dg_{13} dg_{23} d\mathbf{s}^N d\mathbf{u}^N \cdot \\ & \exp\left\{ -\frac{P}{k_\mathrm{B}T} V(\mathbf{H}) + (N+3)\ln V(\mathbf{H}) \right\} \end{aligned}$$

Monte Carlo moves are accepted if no overlap results, and within the no-overlap phase space according to

$$\mathrm{acc}_{n\to n+1} = \min(1, \exp\left\{ -\frac{P}{k_\mathrm{B}T}(V_{n+1} - V_n) + (N+3)\ln\frac{V_{n+1}}{V_n} \right\}) \quad \text{no overlap} \tag{2.11}$$

Note that Eq. (2.11) must be evaluated only for moves which change $\ln h_{ii}$ since $V = h_{11}h_{22}h_{33}$.

2.1.2.2 Monte Carlo Moves

Having established the acceptance rule Eq. (2.11), we turn to the generation of MC moves as implemented in this work. Figure 2.1 serves as illustration for rectangular boxes (left), often synonymous with constant-pressure MC, and the full zero-tension case (right).

There are particle moves and box shape moves; and the particle moves are either displacement moves or orientational moves. First, the kind of move is randomly chosen so that for N particle moves, there is on average one box shape move. For the case of a particle move, a particle is chosen at random, and a coin is flipped to decide between displacement move and orientational move.

To construct the displacement vector for the displacement move, a random vector on the unit sphere is generated and then scaled by $\Delta_\mathrm{d} \cdot (V)^{\frac{1}{3}}$, where Δ_d is a parameter and V the box volume. Δ_d was automatically adjusted during equilibration to achieve an acceptance rate near 30%. $(V)^{\frac{1}{3}}$ is included to relate the size of the displacement to the present density. The acceptance rate then becomes less sensitive to the density, and hence more stable; this also expedites the adjustment of Δ_d. Next, the component of the vector parallel to the symmetry axis of the ellipsoid is scaled by $1.7 \cdot l/w$, where 1.7 is an empirical factor. This adjustment accounts for the fact that a prolate ellipsoid can move a larger distance along its symmetry axis than perpendicular to it without causing overlap (vice versa for oblate ellipsoids). The resulting vector is added to the current position vector (in unscaled **r**-space) of the ellipsoid. The move is accepted if no overlap results from the displacement. The factor of 1.7 was obtained by monitoring the acceptance

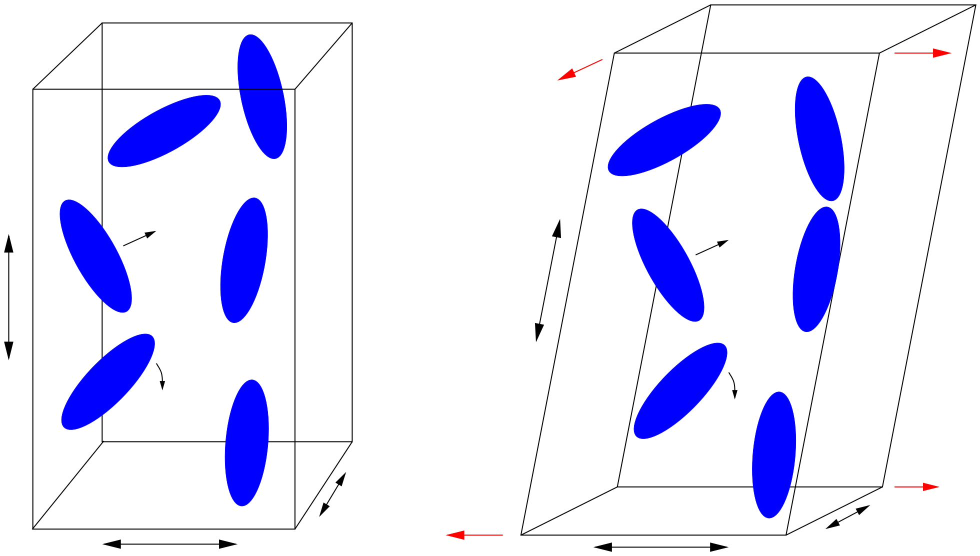

Figure 2.1: Illustration of Monte Carlo moves. In addition to particle moves, changes of the box shape are indicated. Left: Constant-pressure MC. Right: Constant-pressure-and-tension MC.

rates of purely longitudinal and purely transverse moves (occasionally carried out for this purpose), and adjusting the factor until the acceptance rates were about equal. In this way we achieved that the longitudinal and the transverse parts of a regularly attempted displacement contribute roughly equally to causing rejection. This optimizes local exploration of phase space.

The orientation of an ellipsoid is represented as a unit vector along the symmetry axis. For an orientational move, we add to this vector a random vector on the unit sphere, scaled by Δ_o. This number we also automatically set during equilibration to achieve an acceptance rate near 30%. The resulting vector is reduced to unit length to obtain the new orientation. The move is accepted if no overlap results. (For dilute, nearly spherical systems, the maximal $\Delta_\mathrm{o} = 1$ would still produce acceptance rates somewhat larger than 30%.)

Box shape moves are composed of two sub-moves: compression moves, which change the vertical separation of the walls (i.e. $\ln h_{ii}$), and shear moves, which shear the box (i.e. change g_{ij}). At the beginning, these moves are independent from each other, and shear moves are (on average) carried out twice as often to accelerate the move size adjustment (below). In each case, a random vector is chosen from the unit cube and scaled by a factor Δ_p for compression moves and Δ_s for shear moves; they are once more automatically adjusted to reach 30% acceptance. When this is done, Δ_p and Δ_s are held fixed, and the two moves no longer occur as such[5]. Only combined versions are carried out: A random vector is chosen for each sub-move and scaled by the corresponding factor; then both are scaled again, by a factor Δ_c, which is adjusted to obtain 30% acceptance for this combined version. All shape-changing moves are affine, i.e. the particle positions are mapped to the new box geometry, so that the system remains homogeneous. In practice this means re-evaluating $\mathbf{r} = \mathbf{H}\mathbf{s}$ for all particles.

In addition, we introduced an efficiency gain by rotating the particles according to changes in shear. A change in shear in a real suspension of anisometric particles causes these particles to reflect the curl in the flow field. We found that up to twice as large shear moves were possible (while keeping the acceptance ratio near 30%) if the particles were rotated according to a rotation vector

$$\omega = \begin{bmatrix} \Delta h_{23}/\bar{h}_{33} \\ -\Delta h_{13}/\bar{h}_{33} \\ \Delta h_{12}/\bar{h}_{22} \end{bmatrix}$$

where the direction of ω is the axis of rotation and the empirical $0.7|\omega|$ specifies the angle in radians. Δh_{ij} denotes the change in the corresponding component of $\mathbf{H}$, while $\bar{h}_{ii}$ denotes the arithmetic mean of the old and new value. This construction satisfies detailed balance since exchange of old and new components reverses the sign of the rotation.

After all move sizes have been adjusted, the parameters are held fixed because automatic adjustment violates detailed balance each time it occurs [63]. While this did no harm during equilibration, no such risk was desired during measurement.

2.1.3 Other Monte Carlo Versions

The first spontaneous transition from sFCC to SM2 (Chapter 3) in fact occurred in conventional constant-pressure MC (left part of Figure 2.1). The acceptance rule Eq. (2.11) was used (but using $N+1$, by tradition). The translational moves were generated by choosing a random vector from a box of linear size δ, and δ was automatically adjusted for 30% acceptance ratio. The rotational moves were as described in the previous section. Regarding box shape, only compression moves were done; they were carried out the same way as the corresponding sub-move above (but aiming for 20%; no significant efficiency gain or loss was found).

For the equilibration of the glassy systems, the box was held cubic (not only rectangular), i.e. only isotropic volume changes were done, for computational convenience regarding correlation functions. The MC production runs of the glassy systems held the box fixed [(N,V,T)-ensemble]. Particle moves were carried out as described in the previous paragraph. Only overlap decided acceptance.

---

[5] Except rarely for monitoring purposes.

The moves were made small to mimic Brownian motion and to render grazing collisions unimportant (Section 4.1 has more details). The time unit “MC step” refers to N attempted moves.

2.1.4 Testing for Overlaps

Particle overlap was checked by a routine [23] which uses the Vieillard-Baron [10] and Perram-Wertheim [11, 12] criteria to test whether a pair of ellipsoids, given the separation vector and the orientations, overlaps. It does so by progressing from the circumscribed and inscribed spheres tests, which permit early decision, to an evermore detailed examination.

The checking of particle overlap was made more efficient by implementing a cell system [64]. The minimum cell wall separation is kept at least as large as the longest axis of the ellipsoids. The consequence is that an ellipsoid can overlap only with others of the same cell or of the 26 neighboring ones. This keeps the search for overlapping neighbors local, and improves the scaling of the algorithm from $O(N^2)$ to $O(N)$.

2.2 Molecular Dynamics Simulation (MD)

2.2.1 General Features

Molecular dynamics (MD) simulation amounts to numerically integrating Newton’s equations of motion:

$$m_i \ddot{\mathbf{r}}_i = -\nabla_i V(\{\mathbf{r}_k\}) \equiv \mathbf{F}_i \tag{2.12}$$

where m_i is the mass of particle i, $\mathbf{r}_i$ its position, and $\mathbf{F}_i$ the force on it. $V(\{\mathbf{r}_k\})$ is the potential. $\{\mathbf{r}_k\}$, $k = 1, \ldots, N$ denotes the set of all position vectors, with N the total number of particles. We ignore orientational degrees of freedom for brevity. For ellipsoids of revolution the analogue of Eq. (2.12) is a system of $5N$ coupled linear partial differential equations. Its solution is a trajectory in phase space. Eq. (2.12) are solved numerically by an appropriate integration scheme, which we will discuss below. MD simulations rely on ergodicity, i.e. the equivalence of time and ensemble averages, and care must be taken that the simulation is in fact ergodic. For fluids, i.e. our case, this requires sufficient equilibration.

A thorough introduction to molecular dynamics simulation is given by Frenkel and Smit [57] and Allen and Tildesley [65].

2.2.2 Event-driven MD

The situation in hard-particle models is special in that the potential is not differentiable, so that usual integration schemes fail. The method of choice is an event-driven algorithm, which progresses through time from collision to collision. One such algorithm was described by Allen et al. [23], and we are indebted to Mike Allen for providing us with the code. The description in Ref. [23] is quite detailed so that the following brief outline shall suffice.

As mentioned, the general approach is to advance from collision to collision. Collisions are implemented to obey the conservation of linear and angular momentum, and of energy. Between collisions, the particles translate and rotate freely. The ellipsoids are taken to have a smooth surface, so that the angular momentum about the symmetry axis is constant and kept zero. The moment of inertia associated with end-over-end rotation is commonly (and in this work) chosen according to uniform mass distribution, $I = {}^{1}\!/_{20} \left[({}^{l}\!/_{w})^2 + 1 \right] mw^2$.

The equation determining the next collision (if any) of a pair of particles is quadratic in t for hard spheres, but in general (and for ellipsoids) a transcendental one. Therefore, its root must be found numerically. The MD by Allen et al. solves this problem retrospectively, so that an MD step proceeds as follows: First, a small free-flight advance of the system is performed. The system is then examined for overlaps, implying missed collisions. The times of those collisions are determined by numerical root-finding (using the Newton-Raphson method [66]), and the collisions are sorted in chronological order. Each colliding pair is then rewound to the time of its collision, the collision is performed, and the pair is brought forward in time again. Resulting overlaps are checked. Their presence is met with abandoning the attempted step, and trying half the step. The same holds for any other complexity. If the step was halved, and carried out successfully, the remainder is attempted in the same fashion. If not, the step is halved again, and so on.

The advantage of this approach is that collisions will not be missed apart from small grazing ones, and the root-finding is always begun with knowledge that a root exists in the time interval considered. The size of the initial attempt is a matter of efficiency only, and set so that abandoning and halving is infrequent. As we also find in our work, this MD algorithm is efficient.

The program of Allen et al. [23] was adapted slightly for numerical stability and to meet our data-taking requirements (Section 4.1).

The length of an MD step was $0.0005\,\sqrt{m/k_{\mathrm{B}}T}\,\sqrt[3]{l/w}w$. At $\phi = 0.598$ (the highest volume fraction simulated with MD in our work), about four collisions per particle took place in 100 MD steps.

Chapter 3

Simple Monoclinic Crystal Phase

Here we report our findings on the solid phases of hard ellipsoids. In an exercise aiming to reproduce the equilibrium results of Frenkel and Mulder [1], we constructed an sFCC system of aspect ratio $l/w = 3$ (and others) and used constant-pressure Monte Carlo to perform an expansion run. That is, we lowered the pressure between successive simulations, causing the density to settle at a lower value each time. Already at the second simulated pressure, an unexpected rise in density called for attention. Inspection of a snapshot, followed by double-checking all data and parameters, lead to the suspicion that a new solid phase was found, replacing sFCC in parts of the equilibrium phase diagram. The snapshot is shown in Figure 3.1. We then implemented constant-pressure-and-tension MC to ensure that stresses were not an issue, and proceeded to repeat the transition and to study the properties of the crystal.

3.1 Overview of Simulations

Simulations were performed at constant particle number N, pressure P and temperature T. The shape of the periodic box was allowed to fluctuate, so that the crystal unit cell could find its equilibrium shape. This was achieved by implementing the Monte Carlo equivalent of the simulation method by Parrinello and Rahman (PR) [62, 60, 61], explained in Section 2.1.2. Some simulations kept the box rectangular, i.e. employed constant-pressure MC. The simulations were started with sFCC crystals identical to the ones studied by Frenkel and Mulder [1] (Section 1.3.2.1).

Table 3.1 summarizes all simulations performed for this part of the project. The runs are labeled in column “#” with an index for easy reference, column “l/w” indicates the aspect ratio, “runs” the number of independent runs, column “MC” specifies the method of simulation (see legend), and “N” shows the particle

#	l/w	runs	MC	N	P	Equilibration	Production	Phases ($P_{\mathrm{transition}}$)
1	3.00	1	NPT	768	48-2	$2 \cdot 10^4$-$1 \cdot 10^6$	$5 \cdot 10^4$-$1 \cdot 10^6$	sFCC/SM2/N/I (46; 28; 22)
2	3.00	1	NPT	784	2-48	$5 \cdot 10^4$-$1 \cdot 10^6$	$1 \cdot 10^4$-$6 \cdot 10^6$	I/N (24)
3	4.00	1	NPT	1200	46	$1 \cdot 10^6$	$1 \cdot 10^6$	sFCC/SM2* (46)
4	4.00	1	PR	1200	46, 36	$1 \cdot 10^5$	$1 \cdot 10^6$	SM2*
5	4.00	2	PR	1200	32	$1 \cdot 10^5$	$2 \cdot 10^6$	SM2*
6	0.33	8	PR	1296	50-26	$3 \cdot 10^6$	$2 \cdot 10^6$	sFCC/N (28-26)
7	2.00	8	PR	1728	50-30	$2 \cdot 10^6$	$3 \cdot 10^6$	sFCC/N (34)
8	2.00	8	PR	1728	52-70	$2 \cdot 10^6$	$3 \cdot 10^6$	sFCC
9	3.00	8	PR	1728	48-26	$2 \cdot 10^6$	$2 \cdot 10^6$	sFCC/SM2/N (48-46; 28-26)
10	6.00	8	PR	2352	46-38	$3 \cdot 10^5$	$3 \cdot 10^6$	sFCC/SM2* (46)
11	6.00	8	PR	3072	46	$1 \cdot 10^6$	$2 \cdot 10^6$	sFCC/SM2[*] (46)
12	3.00	9	PR	432	46, 36	$1 \cdot 10^6$	$2 \cdot 10^8$-$4 \cdot 10^8$	SM2
13	2.95-1.15	9	PR*	432	46	$3 \cdot 10^5$	-	SM2/other (1.50-2.00)
14	2.50	9	PR	432	46	-	$1 \cdot 10^8$-$3 \cdot 10^8$	SM2
15	2.00	2x9	PR	432	46	$1 \cdot 10^6$	$2 \cdot 10^8$-$4 \cdot 10^8$	SM2
16	1.75	2x8	PR	432	46	$2 \cdot 10^6$	$2 \cdot 10^8$-$6 \cdot 10^8$	SM2
17	1.55	2x3	PR	432	46	-	$3 \cdot 10^8$-$7 \cdot 10^8$	SM2
18	1.55	2	PR	1728	46	$2 \cdot 10^7$	$4 \cdot 10^8$	sFCC

Methods		Phases	
PR	const.-pressure-and-tension MC	SM2	simple-monoclinic crystal
PR*	PR with g_{23} held fixed	SM2*	SM2 with planar defect
NPT	const.-pressure MC	SM2[*]	some runs SM2, some SM2*
		sFCC	stretched FCC
		N	nematic
		I	isotropic

Table 3.1: Overview of the simulations of phase equilibria.

number in each run. "P" indicates the pressure or range of pressures[1] simulated in each run. When a range is shown, the separation of successive runs is $\Delta P = 2$. "Equilibration" and "Production" indicate the minimum lengths of the mentioned parts of each run, in MC steps. One MC step consisted of N attempts to move or rotate a particle and one attempt to change the box shape, on average. The last column lists the simulated phases (see legend) and, in parentheses, the pressures at which transitions took place. Ranges of pressures are given when the transition occurred at various pressures in independent runs.

Run #1 is the constant-pressure expansion run of ellipsoids with $l/w = 3$ which first showed the transition from sFCC to the new crystal phase, called SM2. Equilibration and production run lengths were on the order of 10^4-10^6 MC steps, where lower densities required shorter runs. During the expansion, the transition from sFCC to SM2 occurred, followed later by melting to the nematic (N) and isotropic (I) phases. Run #2 was a compression run which began isotropic and ended in an over-compressed nematic phase. Runs #1 and #2 yielded equation-of-state data for the isotropic and nematic phases.

In #3, we simulated $l/w = 4$ at $P = 46$ which displayed a transition from sFCC to SM2 with a planar defect. This system was later simulated using the PR constant-pressure-and-tension MC at the same and lower pressures (#4 and #5).

In runs #6-11 we attempted the transition sFCC/SM2 for aspect ratios $l/w = \frac{1}{3}, 2, 3, 6$ using PR and larger systems. We simulated eight independent systems in each case, performing expansion runs (#6-10 except #8), compression runs (#8) and single-pressure runs (#11 at $P = 46$).

Runs #12: Realizing that the study of the soft angle of inclination in the SM2 crystal required much longer runs, we set up smaller systems ($N = 432$) for $l/w = 3$ at various angles of inclination, and ran them for $\sim 10^8$ MC steps at pressures $P = 46, 36$.

Runs #13: Since the transition to SM2 did not spontaneously occur for $l/w < 3$, but stability was expected on theoretical grounds, we performed runs decreasing the aspect ratio in small steps $\Delta(l/w) = 0.05$. Nine independent such series of runs were performed, which differed by the angle of inclination. It was held fixed, so that SM2 phases with various inclinations were obtained at lower aspect ratios. Transitions to strained sFCC and plastic solid phases took place in the range $1.50 < l/w < 2.00$ (indicated in Table 3.1 where otherwise transition pressures are written). Three inclinations remained SM2 down to $l/w = 1.55$. The output of these series were used for long runs (#14-17) at various aspect ratios in the spirit of runs #12. The inclination was allowed to vary again. "2x9" means that two independent long runs were done for each of nine initial inclinations.

Finally, in #18 two runs with $N = 1728$, $P = 46$ at the possible stability limit

---

[1] The units of pressure are $k_B T / [(l/w) w^3]$. See also pg. xx

$l/w = 1.55$ were initialized with sFCC and run for $\sim 10^8$ MC steps, to see whether a spontaneous transition to SM2 would occur here.

As for efficiency, in a simulation of a system with $l/w = 3$ and $N = 1728$, 1 million MC steps took about twelve hours of CPU time on a 1.8 GHz processor.

3.2 The SM2 Phase at Aspect Ratio 3

All systems with aspect ratios $l/w \geq 3$ left the initial sFCC structure in favor of a simple-monoclinic lattice with a basis of two ellipsoids (SM2). We will now study its properties for $l/w = 3$.

3.2.1 Characterization of Structure

Figure 3.1 compares the initial sFCC structure (top) to a subsequent snapshot of the system in the SM2 phase (bottom) as first observed. The color code distinguishes orientations. The sFCC was constructed as described at the end of Section 1.3.2; all ellipsoids were oriented along the [111] direction (left: perpendicular to the plane of the page; middle and right: vertical). After a collective re-orientation, a different structure emerged, which has two distinct directions of orientation. They alternate in layers which are inclined with respect to the [111] direction. Within layers perpendicular to the [111] direction, the centers of mass of the ellipsoids still form a nearly triangular lattice. It differs from the initial sFCC crystal by a distortion, resulting from the slightly closer spacing of equally oriented ellipsoids. The *tips* of the ellipsoids, however, no longer form a triangular lattice; the collective re-orientation displaced the tips in such a way that they now form a rectangular lattice. This can be discerned in the lower-left part in Figure 3.1. The tips of the neighboring layers interlace. As a result, each ellipsoid now has four nearest neighbors above and below, whereas in sFCC, it had three. The total number of nearest neighbors has increased from 12 to 14, which is indicative of a higher packing efficiency.

The initial triangular symmetry about the [111] direction allows for two additional, equivalent SM2 configurations, which are rotated with respect to the one in Figure 3.1 by $\pm 60^\circ$. We observed these possibilities as well. Figure 3.2 (left) shows a snapshot of SM2 ($P = 46$, $N = 1728$, #9) in which the collective re-orientation took place along an oblique angle with respect to the box walls. The choice of color and contrast highlights here also the arrangement of the tips on a rectangular lattice. Figure 3.2 (right) illustrates the possible directions of re-orientation from sFCC. The yellow line indicates the one the system on the left had chosen, the red ones indicate the other two possibilities. In fact, only two out of our eight systems with $N = 1728$ (#9) assumed the global orientation seen

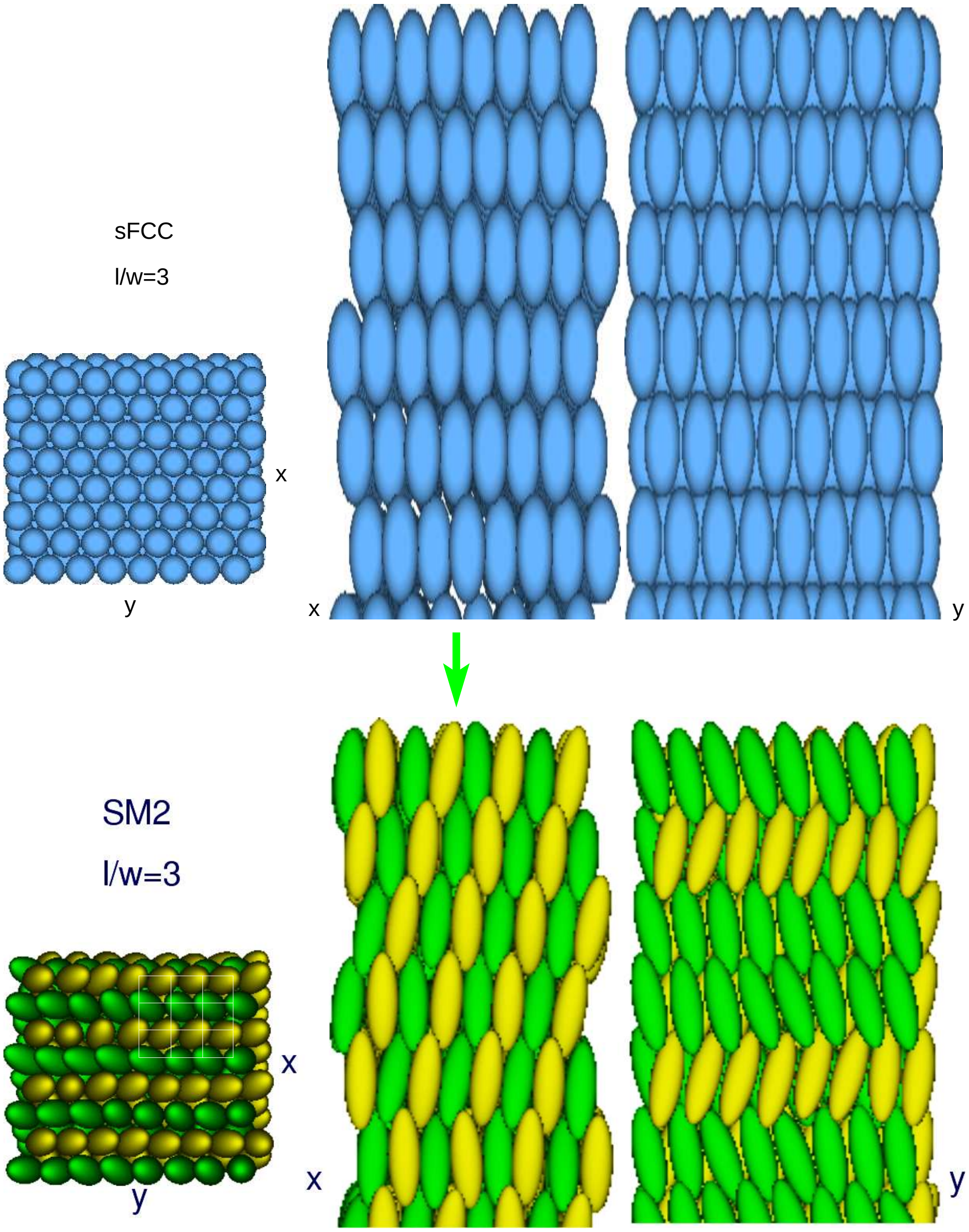

Figure 3.1: Top: Constructed sFCC (cf. Figure 1.4) which was input. Bottom: Snapshot of the SM2 crystal which spontaneously formed from it. The color code distinguishes orientations.

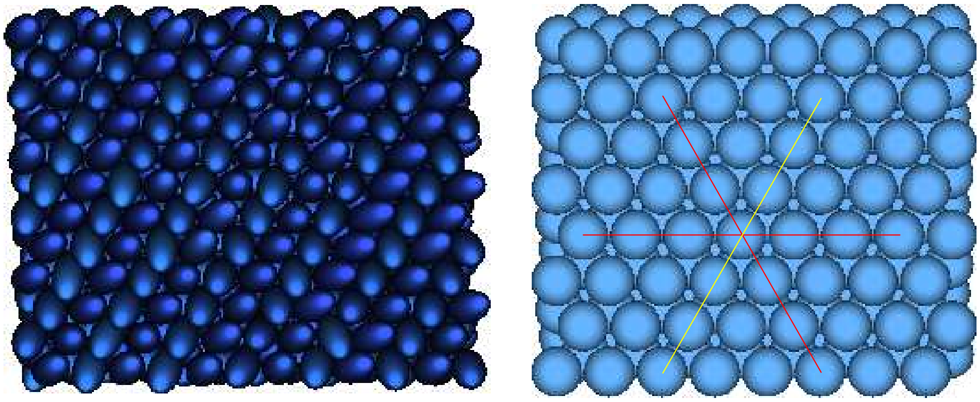

Figure 3.2: Left: Snapshot of SM2 ($P = 46$, $N = 1728$) in which the collective re-orientation took place along an oblique angle with respect to the box walls. The arrangement of tips on a rectangular lattice is clearly visible. Right: Illustration of the possible directions of re-orientation from sFCC. The yellow line indicates the one the system on the left had chosen, the red ones indicate the other two possibilities.

in Figure 3.1. It is reassuring that our algorithm has no preference regarding the global orientation.

We determined the unit cell of SM2 following standard conventions [67, 68, 69]. It is shown in Figure 3.3. The open circles indicate the centers of the two ellipsoids which form the basis. The yellow one forms the origin, the green one is at $\frac{1}{2}(\mathbf{a}+\mathbf{b})$. The parameters used to produce parts a) and b) of Figure 3.3 are thermal average values obtained from simulations #9 ($N = 1728$) at $P = 46$. They are (statistical errors in parentheses): $\alpha = 90.01(3)^\circ$ and $\gamma = 90.00(2)^\circ$, making the cell monoclinic; $\beta = 105.2(4)^\circ$; $|\mathbf{a}| = 1.907(1)$, $|\mathbf{b}| = 1.0695(1)$, and $|\mathbf{c}| = 2.400(4)$; the calculated position of the green ellipsoid is $0.49998(1)\mathbf{a} + 0.50002(3)\mathbf{b} + 0.00003(6)\mathbf{c}$, suggesting that its equilibrium position is exactly $\frac{1}{2}(\mathbf{a}+\mathbf{b})$; the orientations of the ellipsoids form an angle of $27.2(6)^\circ$, which is bisected by the *ac*-plane; both orientations form an angle of $10.6(9)^\circ$ with the *bc*-plane.

The angle of inclination β is very soft, and it did not settle to an equilibrium value in runs #9 or elsewhere in the regime $l/w > 2$. We will see below that it may assume a wide range of values in a single simulation. The values for the cell geometry are thus exemplary and are valid *provided* that $\beta = 105.2(4)^\circ$. However, the cell always remained monoclinic, even when the pressure was lowered to the melting transition into the nematic phase. The same holds for the symmetry in orientation and the placement of the green ellipsoid. We conclude that the crystal structure is simple-monoclinic with a basis of two ellipsoids, hence the name "SM2."

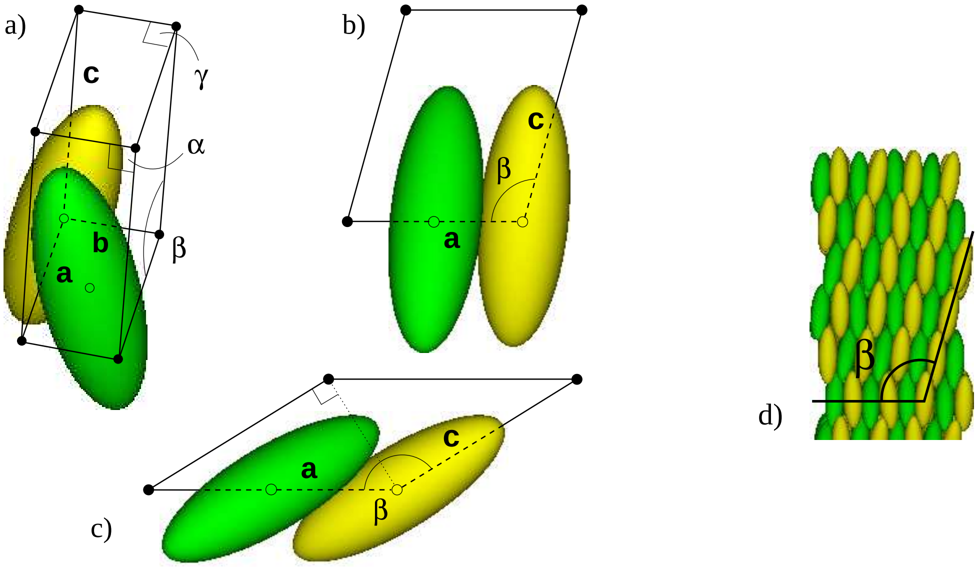

Figure 3.3: Unit cell of SM2 for $l/w = 3$. The open circles indicate the centers of the two ellipsoids which form the basis. The yellow ellipsoid is at the origin, the green one is at $\frac{1}{2}(\mathbf{a}+\mathbf{b})$. The orientations are symmetric about the *ac*-plane. The cell is monoclinic. β exhibits large variations. The parameters in Parts a) and b) are average values for $N = 1728$ and $P = 46$. Part c) shows the cell at close-packing with $\beta \approx 148.3^\circ$, where it is an instance of the family of packings introduced by Donev et al. [2]. Part d) illustrates that β specifies the angle which the planes of equal orientations form with the basis of the simulation box from Figure 3.1.

Figure 3.3c) shows an instance of the unit cell with an additional symmetry, which allows for the maximum packing fraction (Section 3.2.2). Finally, part d) demonstrates that β specifies the angle which the planes of equal orientations form with the basis (the “floor”) of the simulation box from Figure 3.1. This holds whenever **a** and **b** are parallel to the box edges, which is the result of the collective re-orientation parallel to one edge (i.e. along the horizontal red line in the right part of Figure 3.2).

3.2.2 Close-Packing Limit

The simulations #1-9, displaying the relatively steep unit cell of Figure 3.3a) and b), raised the question of how SM2 is related to the close-packings of ellipsoids described by Donev et al. [2] (Section 1.3.2.2). Recall that they also have two orientations and 14 touching neighbors. Related is the question of what the maximum density of SM2 is. The Donev packings achieve a packing fraction of

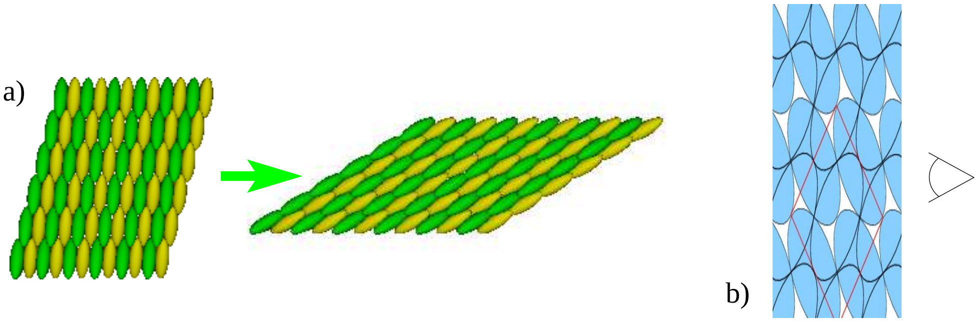

Figure 3.4: a) Maximizing the density of SM2. β increases and planes of equal orientations slide past each other in the process. The resulting structure is an instance of the family of packings reported by Donev et al. [2]. b) Perspective from which to view the Donev packing to identify it with close-packed SM2.

$\phi \approx 0.7707$, which is larger than that of sFCC, $\phi = \pi/\sqrt{18} \approx 0.7405$. To answer both questions, we generated a system in which all ellipsoids are at their ideal lattice positions and orientations, and performed simulations sampling only the unit cell parameters and collective particle orientations, and imposing all symmetries of (steep) SM2. This procedure produces a lower bound for the maximum density of SM2. The initial parameters were average values obtained from the simulations #9 with $N = 1728$ and $P = 46$. In the process of maximizing the density, β increased from 105° to about 150°, and the common tilt of the ellipsoids with respect to the *bc*-plane disappeared. Figure 3.4a) illustrates the process. Inspection of the resulting structure revealed that it is very similar to the Donev construction when the latter is viewed from an in-plane perspective [Figure 3.4b)], and identical if one has the right angle in the unit cell shown in Figure 3.3c). We then imposed this right angle, i.e. that $(\mathbf{a} - \mathbf{c})$ be perpendicular to $\mathbf{c}$. Here $\beta \approx 148.3^\circ$. This optimization achieved the highest packing fraction, differing from $\phi \approx 0.770732$ (the value reported by Donev et al.) by only 3 parts per million, confirming the identification with the Donev construction. We emphasize that this identification holds for the limit of infinite pressure only—the equilibrium value of β may be a different one at lower pressures.

Interestingly, we found a jamming density of 99.663% of the maximum already at $\beta \approx 105^\circ$. Simulations at intermediate values indicate a smooth approach towards the maximum density as β increases. Thus, the close-packing density varies very weakly for $105^\circ < \beta < 148^\circ$. While this range is traversed, ellipsoids of one orientation move past neighbors of the other orientation by almost half their length. This can be seen by comparing Parts b) and c) of Figure 3.3. For reasons of symmetry, this translation may even continue by the same amount while the density remains above 99.663% of the maximum. These observations are in accord with the fact that β is soft at finite pressures, which we discuss next.

3.2.3 Softness of Inclination

The angle of inclination, β, relaxes extremely slowly. The simulations #9 with $N = 1728$ were too slow to equilibrate this degree of freedom. To learn more about it, we carried out a set of very long simulations for a smaller system ($N = 432$, $P =$ 46 and 36, #12) with nine initial values of β in the range $105^\circ < \beta < 150^\circ$. Figure 3.5 reports the inclination in terms of the shear variable $g_{23} = \tan(90^\circ + \beta)$ (g_{23} belongs to the matrix $\mathbf{H}$ introduced in Section 2.1.2). After more than 300 million Monte Carlo steps, there was still no clear evidence for a preferred geometry. Variations of g_{23} corresponding to 15° in β were typical at both pressures even within a single simulation. Hence, we expect the shear modulus of elasticity in this degree of freedom to be very small.

The other two angles, α and γ, were stable at 90°, with fluctuations of $< 1^\circ$. The curves of g_{13}, corresponding to γ, are shown in blue in Figure 3.5. They remain near zero and fluctuate much less. We conclude that the associated shear moduli are much larger.

The runs at $P = 36$ (lower plot in Figure 3.5) raise the suspicion that *two* angles are at least metastable, one for steep SM2, and one centered near (but still different from) the Donev geometry. For β we have $105^\circ \lesssim \beta \lesssim 120^\circ$ and $138^\circ \lesssim \beta \lesssim 148^\circ$, respectively. For comparison, the value for the Donev geometry is $\beta \approx 148$ at $P = 36$.[2] Free-energy calculations, assessing the relative stability of steep SM2 with SM2 at the Donev geometry, are underway at the time of this writing [70]. Preliminary results [71] place an upper bound on the difference, $|\Delta G|/N < 0.3\,k_{\mathrm{B}}T$ ($P = 36$) and $|\Delta G|/N < 0.2\,k_{\mathrm{B}}T$ ($P = 46$), with the Donev geometry *less* stable. Also interesting would be the application of a histogram-reweighting technique to determine the full dependence $G(\beta)$. Given the large fluctuations, we expect the free energy to be a weak function of β; recall the similar behavior of the jamming density. And in addition to the equilibrium value of β, one could extract from $G(\beta)$ an effective modulus of elasticity via $c_\beta = dG(\beta)/d\beta$.

We conclude that SM2 with $l/w = 3$ is soft in one direction only. The reason for this interesting rheological property is that planes of equal orientation slide well past each other in the **c**-direction, and only in that direction. We illustrate this sliding in Figure 3.6a). The softness manifests itself also in another way. In some of the long simulations, we found undulations of the lattice in the **c**-direction

---

[2] The value cannot be quoted exactly since it is a function of other unit cell parameters. We quote the average value obtained while the symmetry in the unit cell [Figure 3.3c)] was approximately obeyed. This was not meaningful for $P = 48$, given the large fluctuations.

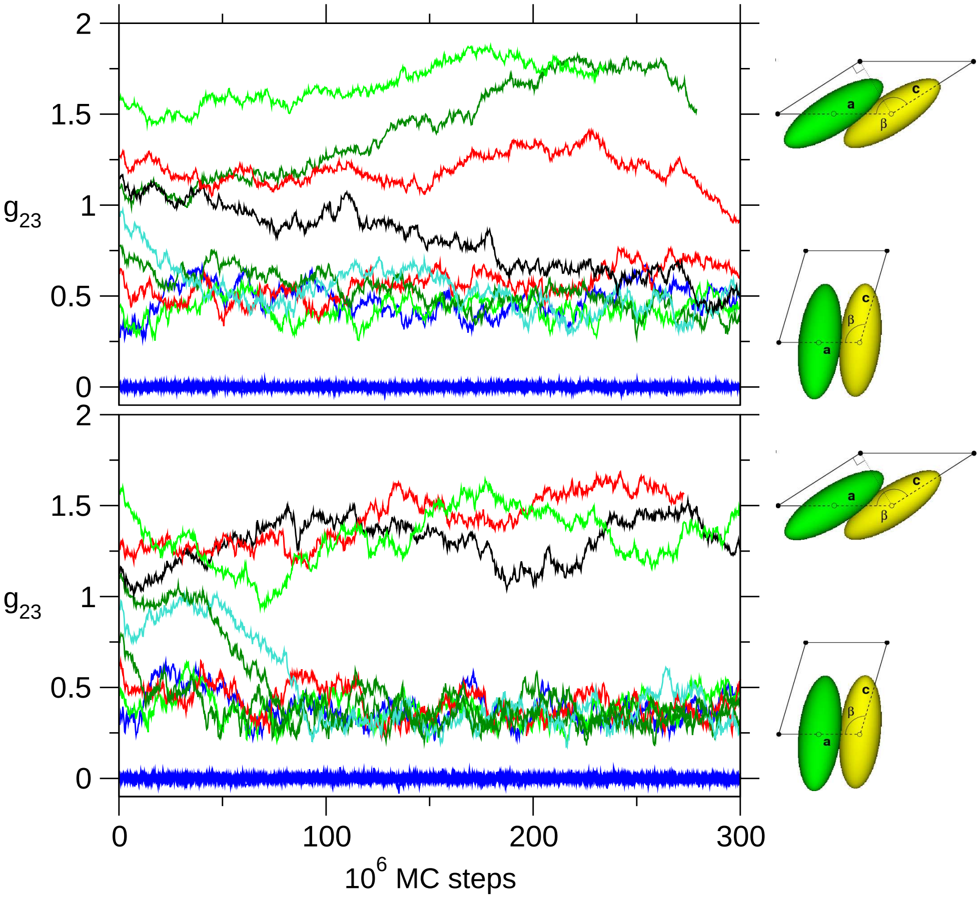

Figure 3.5: Inclination as monitored by the shear variable g_{23}, for the runs $l/w = 3$, $N = 432$, $P = 46$ (top) and $P = 36$ (bottom). g_{23} fluctuates over a broad range, corresponding to values of β in the range $105^\circ < \beta < 150^\circ$. Variations of g_{23} corresponding to 15° in β were typical at both pressures even within a single simulation. This implies a small shear modulus of elasticity. Also shown for comparison is g_{13} (blue) which remains near zero (i.e. the angle γ remains near 90°); it fluctuates much less, corresponding to a much larger shear modulus. The lower plot ($P = 36$) suggests metastability of two angles.

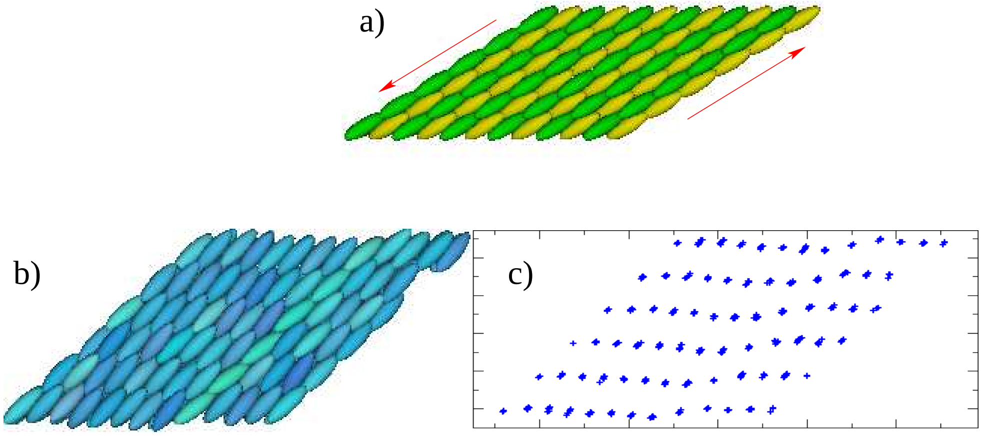

Figure 3.6: a) Planes slide well past each other in the direction indicated by the arrows. b) Defect as a result of the softness. The orientations in one plane (fifth from right) have slightly changed. c) Centers of mass of the same configuration, exposing the undulations in the lattice.

to the point of planar defects, which would spontaneously heal again. A snapshot of such a defect is shown in Figure 3.6b). The slightly different color of one plane (the fifth from the right) shows that the defect also affects the orientations. In Figure 3.6c) we show the centers of mass of the same configuration, and we clearly see the mentioned undulations.

3.2.4 Equation of State Data

Figure 3.7 shows equation of state data of SM2 (blue solid squares) from our simulations with $N = 1728$ particles (runs #9). The density of SM2 is higher than that of sFCC (red open squares [1]) for all pressures. Five of the eight systems #9 underwent the transition to SM2 already at the highest simulated pressure $P = 48$, the remaining three at $P = 46$. Note also that in all our expansion runs, SM2 melted to the nematic phase without ever re-visiting the sFCC phase from which it developed; this is strong evidence that SM2 is lower in free energy than sFCC. Free-energy calculations are in progress also for this comparison [70], and the preliminary data [71] confirm the greater stability of SM2 with $|\Delta G|/N = 0.4(2)\, k_{\mathrm{B}}T$ ($P = 46$), with some evidence that this difference becomes small on reaching the solid/nematic transition.

We also show in Figure 3.7 the nematic branch (triangles) from the (N, P, T)

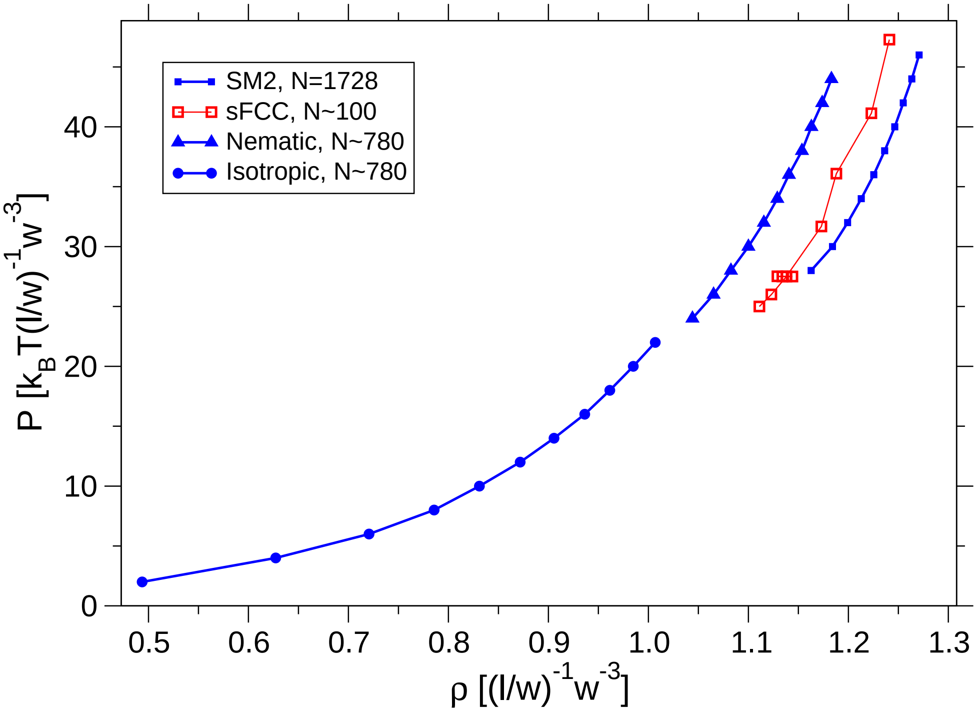

Figure 3.7: Equation of state data for hard ellipsoids at $l/w = 3$. Errors are smaller than symbol size. Lines guide the eye. The density of SM2 (blue solid squares) is higher than that of sFCC (red open squares [1]) for all pressures. SM2 melts directly to the nematic phase without revisiting the sFCC phase. The nematic branch (triangles) is shown including over-compressed states. The isotropic fluid states are shown as circles.

compression run with $N = 784$ particles (#2) and up to 6 million MC steps per run. Even at strong over-compression, no spontaneous crystallization took place. This indicates that the nucleation barrier to the SM2 phase is high. Also shown is the isotropic fluid branch (circles) as obtained from (N,P,T) compression and expansion runs with $N \approx 780$ (#1 and #2). The isotropic/nematic transition, by contrast, readily occurs in simulation.

3.3 Other Aspect Ratios and Phase Diagram

3.3.1 Aspect Ratios Greater Than 3

All eight simulations (#11) at $l/w = 6$ formed SM2 as well, at $P = 46$, and the transitions from sFCC occurred along all of the possible directions of re-orientation. However, four of the systems retained a planar defect. Different regions in the

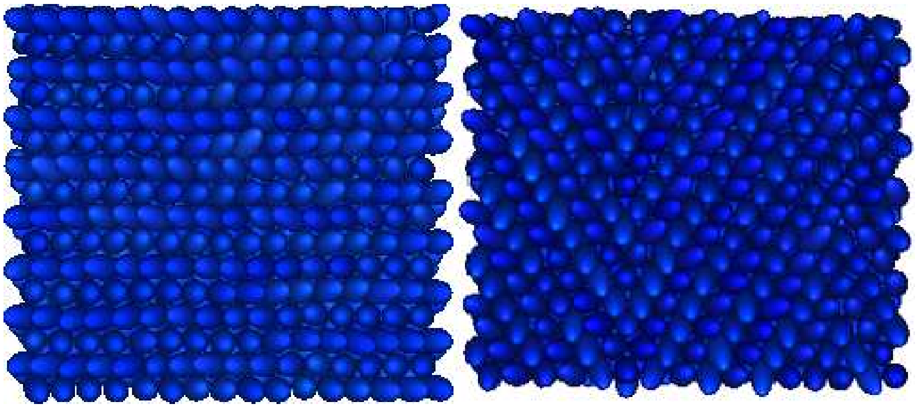

Figure 3.8: SM2 with aspect ratio $l/w = 6$, $N = 3072$, and $P = 46$. Left: defect-free structure. Right: two vertical planar defects, separating two conflicting orientations of SM2.

periodic box were able to simultaneously develop different global orientations of SM2 as the systems were larger ($N = 3072$) than those with $l/w = 3$ ($N = 1728$). Figure 3.8 displays the defect-free case (left) and an example of two domains with unequal orientations of SM2. One can see two planar defects, or grain boundaries, separating the two regions.

The series #11 was preceded by the eight runs #10 ($l/w = 6$, $N = 2352$, $P \leq 46$) where SM2 formed with defects throughout, in this case related to a geometrical mismatch between the simulation box and the SM2 unit cell. A plane of one orientation did not find itself after one periodic length, but a plane of the other orientation. Figure 3.9 shows an example. Healing of this defect did not happen, at any simulated pressure, as it would require a change in box shape corresponding to a full particle displacement, and involving one of the stiff angles. Defect-free SM2 would have been accessible when re-orienting parallel to the box wall, but all systems chose the other two options.

We also simulated a system with $l/w = 4$, $N = 1200$ and $P = 46$, initially using conventional (N,P,T) sampling (#3), i.e. keeping the box rectangular. The system formed SM2 with a planar defect, also stemming from the geometrical mismatch between box and unit cell. Follow-up simulations of this system using constant-pressure-and-tension sampling at the same and lower pressures (#4 and #5) did not change this result. It is worth emphasizing that for $l/w = 3$ and 4, SM2 formed from sFCC even in simulations sampling only rectangular box shapes (#1 and #3). It is therefore more stable than sFCC even when subjected to the associated stress, and even in the presence of the discussed defect.

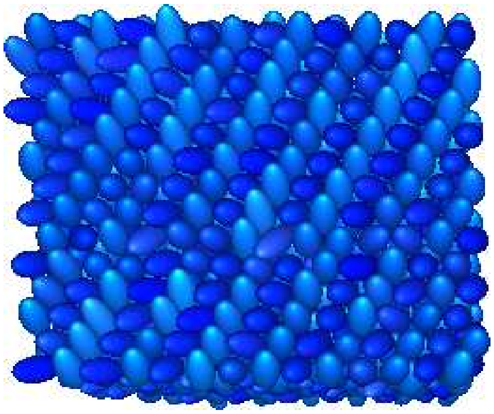

Figure 3.9: SM2 with defect due to a geometrical mismatch of the simulation box and the unit cell ($l/w = 6$, $N = 2352$, $P = 36$). Planes of one orientation meet with planes of the other orientation after one periodic length.

3.3.2 Aspect Ratios Smaller Than 3

By contrast, ellipsoids with $l/w = 2$ and the oblate $l/w = \frac{1}{3}$ showed no tendency to leave the initial stretched-FCC structure. We studied expansions of these systems with eight independent simulations each (#7 and #6, respectively). In none of them did two preferred directions of ellipsoid orientation develop. All of them melted to the nematic phase on expansion, directly from sFCC. Compressions of the system with $l/w = 2$ (#8) also stayed in the sFCC phase.

But note that the apparent stability of sFCC in our simulations may well be due to a free-energy barrier, rather than indicating genuine stability. The work of Donev et al. [2] supports this possibility, at least for high pressures, since the record volume fraction $\phi \approx 0.7707$ exists down to $l/w = \sqrt{3} \approx 1.73$. To study the properties of SM2 at shorter aspect ratios, we performed a series of runs at $P = 46$ with successive decreases of aspect ratio ($\Delta(l/w) = 0.05$, runs #13). Nine systems were set up with angles β in the range $105^\circ < \beta < 150^\circ$. With the stable value of β as a function of aspect ratio unknown, we held it fixed so as to have a range of values available at lower aspect ratios for further study. In the process, some systems left the SM2 phase in favor of a strained version of sFCC or plastic solid. Only SM2 was considered further (#14-17).

At $l/w = 2.50$, all systems were still SM2, and we performed long runs to study the behavior of β and to look for departures from SM2. The systems remained SM2, and the distribution of β appeared bimodal, similar to the lower part of Figure 3.5. We have $112^\circ \lesssim \beta \lesssim 129^\circ$ for the steep version and $139^\circ \lesssim \beta \lesssim 144^\circ$ for the Donev geometry, and here the cell was observed to fluctuate around the associated symmetry (recall that this was not the case for $l/w = 3$, $P = 36$). The analogous analysis for $l/w = 2.00$ found only the Donev geometry, with $132^\circ \lesssim \beta \lesssim 138^\circ$. The same holds for $l/w = 1.75$ and $l/w = 1.55$ ($126^\circ \lesssim \beta \lesssim 129^\circ$ for both).

These results admit the tentative conclusion that steep SM2 becomes unimportant for $l/w < 2.50$, and only one geometry remains, coinciding with the Donev one for $l/w \lesssim 2.50$. For $l/w = 3.00$, we point out that both geometries are distinct from the Donev case (as observed at $P = 36$), highlighting the limited information available from close-packing results.

We also see from the ranges of β that this soft angle in the crystal becomes harder during the traversal to low l/w, approaching the behavior of the stiffer angles α and γ. The fluctuations of the latter were observed to vary only weakly as a function of aspect ratio. The hardening of β is not surprising since the curvature of the particles becomes stronger, hindering the sliding of planes.

The last three systems still in the SM2 phase at $l/w = 1.55$ left the phase upon reduction to $l/w = 1.50$ (to plastic solid and in one case to sFCC). Since SM2 was still stable at $l/w = 1.55$ for up to 700 million MC steps, we suspect the end of (meta)stability of SM2 in the range $1.50 < l/w < 1.55$ at $P = 46$. At the possibly limiting $l/w = 1.55$, we performed two long simulations ($N = 1728$, $P = 46$, #18) to test whether the spontaneous transition from sFCC to SM2 would take place. It did not, sFCC was found metastable, for 400 million MC steps.

3.3.3 Phase Diagram

In Figure 3.10 we show a phase diagram of prolate hard ellipsoids of revolution. It includes part of the results of Frenkel and Mulder [1], and their suggested phase boundaries and coexistence regions. We have inserted our state points and a vertical dashed line to delimit the region in which we found SM2 more stable by spontaneous transition. To the left of it, and down to $l/w = 1.55$, both sFCC and SM2 are metastable. Assessing their relative stabilities requires free-energy calculations (in progress [70]). Preliminary results [71] show that SM2 is more stable at $l/w = 2$ [$|\Delta G|/N = 0.7(2)\,k_\mathrm{B}T$], but that sFCC is more stable at $l/w = 1.55$ [$|\Delta G|/N = 0.4(2)\,k_\mathrm{B}T$]. This implies that a phase boundary exists in the regime $1.55 < l/w < 2$. Further, recall that the work of Donev et al. [2] shows that the packing advantage over sFCC begins with arbitrarily small elongations. If sFCC is more stable at $l/w = 1.55$ and $P = 46$, there must be a solid-solid phase transition at a larger pressure, since the Donev version of SM2 must become more stable as $P \to \infty$. Further study is clearly warranted here. Finally, we remark that our solid state points are isobar at $P = 46$ (except for the lower SM2 one at $l/w = 3$, where $P = 30$).

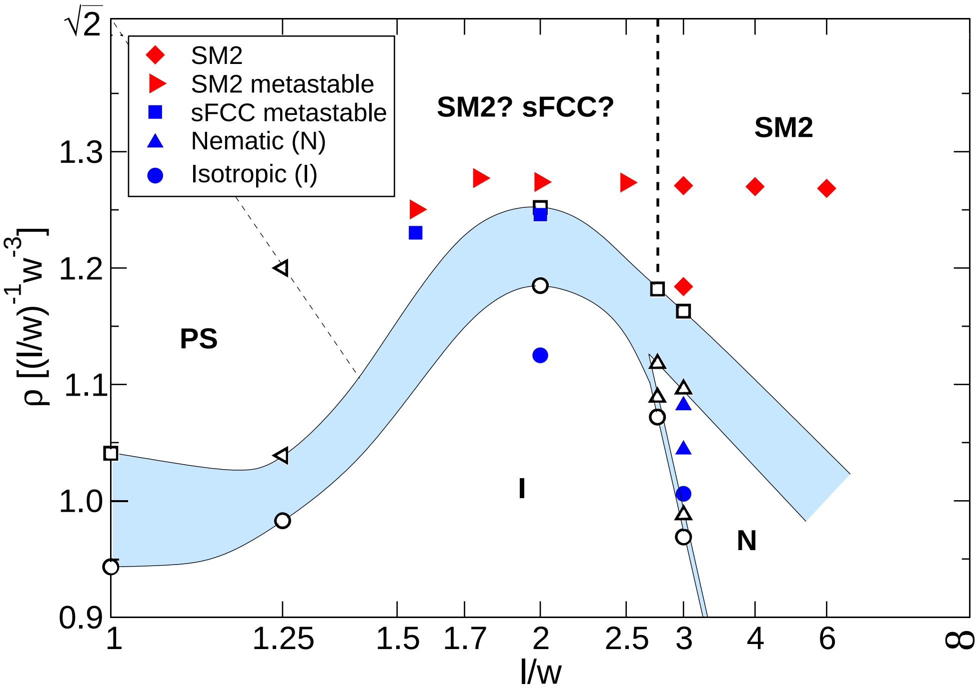

Figure 3.10: Phase diagram of hard, uni-axial ellipsoids ($l/w \geq 1$). The scaling of the abscissa is reciprocal. The diagram shows the results of Frenkel and Mulder [1] (open symbols), and their suggested phase boundaries and coexistence regions. The data points at $l/w = 1$ are taken from Hoover and Ree [72]. We have inserted our state points (filled symbols, errors less than symbol size) and a vertical dashed line to delimit the region in which SM2 was found more stable than sFCC. To the left of it, both sFCC and SM2 are metastable, and assessing their relative stabilities requires free-energy calculations (in progress [70]). Preliminary results [71] indicate that SM2 is more stable down to $l/w = 2$, but that sFCC is more stable at $l/w = 1.55$. Our solid state points are isobar at $P = 46$ (except for the lower SM2 one at $l/w = 3$, where $P = 30$).

3.3.4 Flipping Mode in SM2 at Aspect Ratio 1.55

Figure 3.11 (left) displays a snapshot of SM2 at $l/w = 1.55$ ($N = 432$, $P = 46$, #17). Since the elongation has become relatively short, larger fluctuations around the preferred orientation are expected. The more colorful appearance of the snapshot confirms this view. Note also that the two major orientations are at about 90° with respect to each other, consistent with the Donev geometry at this aspect ratio. The surprise comes with the actual distribution of orientations on the unit sphere (right), including the distinction between "up" and "down" (this is ignored in the color code to account for the head-tail symmetry of our ellipsoids). The existence of four preferred orientations implies that the particles have been able to flip upside-down since the beginning of runs #17 (where we found only two preferred orientations). It is expected that rotation eventually becomes possible on decreasing the aspect ratio (plastic solid phase). It is intriguing, however, that flipping becomes possible prior to that, in the crystal phase. Note that this result concerns the dynamics only since, given the head-tail symmetry, the structure is unaltered when ellipsoids are flipped upside-down. A closer investigation of flipping would be promising: Looking in the reverse direction, i.e. increasing l/w from values where flipping is possible, one should observe a slowing-down and arrest of flipping, which may lend itself to an interpretation in terms of glass physics. Or, given $l/w = 1.55$ (for instance), one should see a slowing-down and arrest upon increasing the density. In the following Chapter 4 (Section 4.3.2.2), we do study the behavior of flipping modes, but in the over-compressed isotropic phase. We will see that they play a special role there, too.

3.4 Summary

In the high density phase diagram of prolate hard ellipsoids of revolution we have found a crystal which is more stable than the stretched FCC structure proposed by Frenkel and Mulder [1]. The new phase, SM2, has a simple monoclinic unit cell containing a basis of two ellipsoids.

The angle of inclination β is a very soft degree of freedom for $l/w = 3$, whereas the other angles are not. This softness disappears with decreasing aspect ratio. A symmetric state of the unit cell exists which could be identified with an instance of the family of packings introduced by Donev et al. [2]. Evidence was found that this state is unstable for $l/w = 3$ with respect to steeper geometries. By contrast, the symmetric geometry becomes important for lower aspect ratios.

Our results unequivocally remove the stretched FCC structure for aspect ratio $l/w = 3$ from the phase diagram of hard, uni-axial ellipsoids. Our state points for $l/w = 4$ and 6 suggest that this holds for the entire range of $3 \leq l/w \leq 6$, and

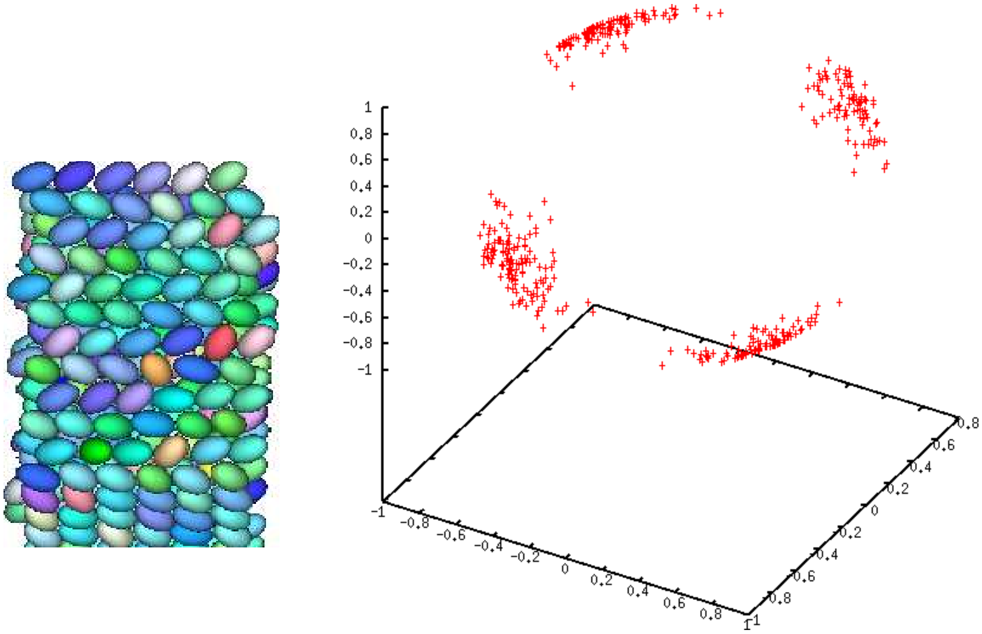

Figure 3.11: Left: snapshot of SM2 at $l/w = 1.55$ ($N = 432$, $P = 46$). The colorful appearance documents the expectedly large fluctuations around the preferred orientations. Right: distribution of orientations on the unit sphere from the same system. The existence of four preferred orientations shows that the particles have been able to flip upside-down (this does not reflect onto the color code of the snapshot).

possibly beyond. Preliminary free-energy calculations [71] indicate stability also for $l/w = 2$, and possibly that sFCC is more stable at $l/w = 1.55$. The latter result implies a phase boundary both for a limiting aspect ratio and a limiting density above the simulated one.

Finally, SM2 at $l/w = 1.55$ displays an interesting dynamical feature, in that flipping of ellipsoids is possible, warranting studies of the cross-over to where this is not possible. And certainly, the application of recent experimental advances in colloidal ellipsoids [36, 37] seems very promising.

Chapter 4

Glassy Dynamics in Almost Spherical Ellipsoids

We report here on our findings of glassy dynamics in hard ellipsoids. The study was motivated by the Molecular Mode-Coupling Theory (MMCT) predictions of Letz et al. [3], and as a complement to the molecular dynamics investigation of de Michele et al. [30] which did not focus on the over-compressed fluid states. Understanding the slowing-down of a system is also of interest outside the context of glass physics; for instance, it is critical for studies of nucleation. As we will see, nearly spherical ellipsoids display glassy dynamics in positional and orientational degrees of freedom. This by itself is surprising for a monodisperse, relatively simple system. Typically, polydispersity in size, a mixture of particle species, or network-forming covalent bonds are prerequisite to prevent the competing crystallization. We hence show that a slight particle anisometry acts as a sufficient source of disorder. This sheds new light on the question of which ingredients are required for glass formation.

This part of our work was done in collaboration with a visiting Master student, whose internship (two times two months) the author co-supervised. She prepared and performed the MD side of the simulations, and assisted with programming and data-analysis tasks. She also performed a modified repetition of an MC simulation ($l/w = 0.8$, $\phi = 0.614$), and early analysis thereof, for the study of heterogeneous dynamics.

4.1 Overview of Simulations

Figure 4.1 shows snapshots of the simulated systems. At first sight, they all look the same. However, the upper systems contain prolate ($l/w = 1.25$) ellipsoids, while the lower ones contain oblate ($l/w = 0.8$) ellipsoids; and the left-hand sys-

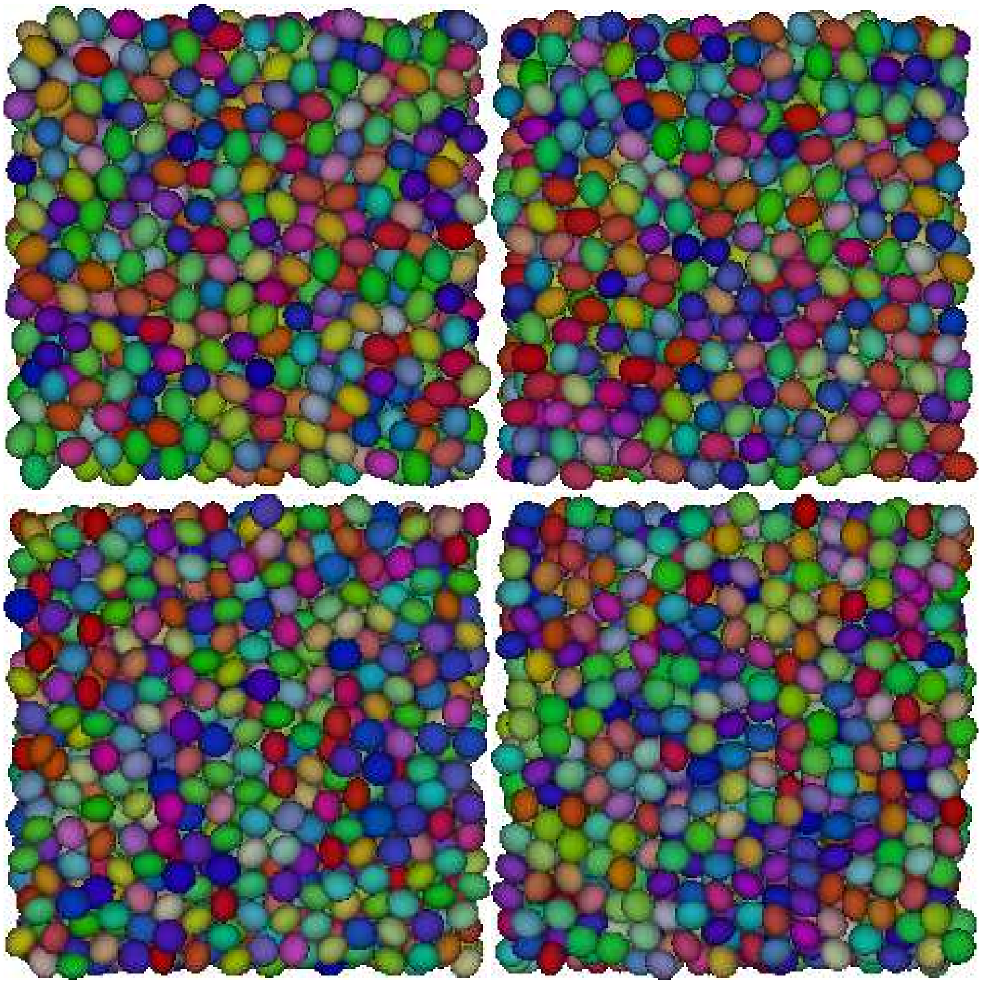

Figure 4.1: Snapshots of the simulated suspensions. The color code indicates orientation. At first sight, they all look the same. However, the upper systems contain prolate ($l/w = 1.25$) ellipsoids, while the lower ones contain oblate ($l/w = 0.8$) ellipsoids; and the left-hand systems are isotropic, while the right-hand systems are plastic solids. Especially for $l/w = 0.8$, the plastic solid is not easy to identify by eye.

tems are isotropic, while the right-hand systems are plastic solids. The similarity of the prolate and oblate systems will in fact recur in our results. This is, however, not trivial, since the two bodies are fundamentally different: In the limit of large anisometry, prolate ellipsoids approach one-dimensional needles, while oblate ellipsoids approach two-dimensional disks. Nevertheless, earlier work on ellipsoids (see Section 1.3.2) has found an approximate symmetry in properties under exchange of l/w with its inverse. Regarding the two phases "isotropic" and "plastic solid", we note that the distinction by eye is not easy, especially if the planes of symmetry are oblique with respect to the simulation box. In the Figure, the plastic solid in $l/w = 0.8$ is hard to see. An order parameter is in order, we describe it below.

Table 4.1 summarizes all simulations for the glassy dynamics work. The systems were equilibrated using MC at constant particle number N, pressure P and temperature T [73, 74] in a cubic box with periodic boundaries (see Section 2.1). Each system contained more than 3000 particles. For $l/w = 0.80$, a dilute, random configuration was compressed at $P = 4$ and $P = 7$[1] for 10^6 MC steps each, and the resulting configuration served as input for the run at $P = 10$. For $l/w = 1.25$, a dilute, random configuration was input for the run at $P = 10$ directly. The output of each equilibration run was used as the starting configuration for the next higher pressure.[2] During equilibration, the MC step size was automatically adjusted so that an acceptance rate close to 30% (20% for volume moves) was obtained. Up to $P = 23$ ($l/w = 1.25$) and $P = 17$ ($l/w = 0.80$), this was not done for rotation moves because even the largest possible setting resulted in a higher acceptance rate. This largest setting was used there, i.e. the sphere from which a random vector was chosen (and added to the current orientation, followed by normalization) had unit radius.

The systems were considered equilibrated[3] when the volume fraction had settled and all positional and the orientational correlators were independent of absolute simulation time. The latter requirement was verified in the production runs. Towards the end of each equilibration run, a configuration with a volume fraction close to the average volume fraction was chosen and scaled to the average volume fraction exactly. It served as the input for the production runs.

For production, we used MC and MD. In the MC simulations (now at constant volume) the step sizes were fixed to small values (displacement: $0.007w$; rotation: 0.1); the acceptance rate was then near 70% at the highest simulated volume fractions. The particles mimic Brownian motion, similar to colloidal ellipsoids suspended in a liquid. The step sizes were the same for all runs, hence a unique

---

[1] The units of pressure are ${k_\mathrm{B}T}/{[(l/w)w^3]}$. See also pg. xx.

[2] Equilibration runs at $P = 27, 28, 29$ were all based on the output of the run at $P = 26$.

[3] For the case of over-compression, "equilibrated" here means within the metastable isotropic basin.

l/w	1.25					0.80				
N	3072					3332				
P	ϕ	ρ	Equil.	Production		ϕ	ρ	Equil.	Production	
$\frac{k_B T}{(l/w)w^3}$	-	$\frac{1}{(l/w)w^3}$	MC steps	MC steps	MD steps	-	$\frac{1}{(l/w)w^3}$	MC steps	MC steps	MD steps
10	0.474	0.905	$2 \cdot 10^6$	$1 \cdot 10^6$	$4 \cdot 10^5$	0.473	0.903	$1 \cdot 10^6$	$4 \cdot 10^6$	$1 \cdot 10^6$
13						0.504	0.962	$1 \cdot 10^6$	$4 \cdot 10^6$	$1 \cdot 10^6$
14	0.511	0.976	$2 \cdot 10^6$	$1 \cdot 10^6$	$4 \cdot 10^5$					
17	0.533	1.019	$2 \cdot 10^6$	$4 \cdot 10^6$	$4 \cdot 10^5$	0.533	1.018	$2 \cdot 10^6$	$1 \cdot 10^7$	$1 \cdot 10^6$
20	0.551	1.052	$2 \cdot 10^6$	$4 \cdot 10^6$	$4 \cdot 10^5$	0.550	1.051	$1 \cdot 10^6$	$1 \cdot 10^7$	$1 \cdot 10^6$
23	0.565	1.079	$2 \cdot 10^6$	$1 \cdot 10^7$	$4 \cdot 10^5$	0.565	1.080	$2 \cdot 10^6$	$1 \cdot 10^7$	$1 \cdot 10^6$
26	0.578	1.103	$3 \cdot 10^6$	$1 \cdot 10^7$	$4 \cdot 10^5$	0.578	1.103	$2 \cdot 10^6$	$1 \cdot 10^7$	$5 \cdot 10^5$
27	0.581	1.110	$2 \cdot 10^6$	$1 \cdot 10^7$	$4 \cdot 10^5$					
28	0.585	1.117	$2 \cdot 10^6$	$1 \cdot 10^7$	$4 \cdot 10^5$					
29	0.588	1.124	$3 \cdot 10^6$	$6 \cdot 10^6$	$4 \cdot 10^5$	0.589	1.124	$2 \cdot 10^6$	$6 \cdot 10^6$	$1 \cdot 10^6$
32	0.598	1.143	$3 \cdot 10^6$	$1 \cdot 10^7$	$1 \cdot 10^5$	0.598	1.142	$2 \cdot 10^6$	$2 \cdot 10^7$	$4 \cdot 10^5$
35						0.606	1.158	$2 \cdot 10^6$	$3 \cdot 10^7$	
38						0.614	1.172	$2 \cdot 10^6$	$2 \cdot 10^7$	

Table 4.1: Overview of glassy dynamics simulations.

time scale could be established and unphysical grazing moves, violating the hard ellipsoid model, occurred to the same degree in all MC simulations. Comparison with the MD method shows that their effect is not significant.[4]

The MD simulations implemented free flight and elastic collisions [23]. The method is outlined in Section 2.2.2. The code of Allen et al. [23], kindly provided by M.P. Allen, was adapted to initialize uniformly-distributed angular momenta, to output configurations on the logarithmic time scale and reflecting the full displacements of particles, and to be numerically more stable for long runs with $N \approx 3000$. The moment of inertia for end-over-end rotation was set to $I = {}^{1}\!/_{20} \left[\left({}^{l}\!/_{w} \right)^2 + 1 \right] mw^2$, which corresponds to uniform mass distribution. The angular momentum about the symmetry axis was kept zero (smooth ellipsoid surfaces). The length of an MD step was $0.0005 \sqrt{m/k_\mathrm{B}T} \sqrt[3]{l/w}w$. At $\phi = 0.598$, about four collisions per particle took place in 100 MD steps. The input configurations were assigned Maxwell-Boltzmann velocity distributions at unit temperature, and then run for at least 10,000 steps so that local temperature and density fluctuations could come to correspond. Mismatches therein were visible in the intermediate scattering functions at short time scales.

The limitation in simulating glassy dynamics in our systems lies in the fact that upon over-compression, the time scale of crystallization eventually becomes comparable to that of the α-relaxation. Thus, our systems acquired a tendency to crystallize to the rotator phase at high volume fractions. To monitor crystallinity, we computed the local positional order using the bond-orientational order parameter q_6 [76]. It is based on the symmetry of the arrangement of neighboring particles around a given particle, by use of spherical harmonics. A neighbor is considered bonded if *its* arrangement is sufficiently similar in symmetry and orientation. A particle is considered solid if it has at least 4 bonded neighbors. Finally, a standard cluster algorithm identifies clusters of solid particles. In our systems used for the study of glassy dynamics, the fraction of particles which were part of crystalline clusters never exceeded 2.6% and was typically below 0.5%.

We used all of the production data summarized in Table 4.1, with the exception of the MC and MD runs of $l/w = 1.25$ at $\phi = 0.598$. In the MC case, aging could not be ruled out before $5 \cdot 10^6$ steps, and crystallization set in past $7.2 \cdot 10^6$ steps. In the MD case, crystallization set in past $1 \cdot 10^5$ steps.

With regard to efficiency, we found that both methods perform about equally, the MD method being slightly faster. The longest runs were on the order of several days on a single Pentium$^{\mathrm{TM}}$ 4 CPU. Equilibration was done more efficiently using standard MC. Decay of correlation functions took only $\sim 3/4$ as long there. The MD method had a slightly higher propensity towards crystallization, which for

---

[4] In fact, for the study of long-time dynamics, the independence from microscopic details even allows for considerably larger MC steps, increasing efficiency [75].

our purposes was a disadvantage.

Interestingly, the mentioned symmetry of the prolate and oblate systems breaks down with regard to crystallization. The prolate system crystallizes more readily. The details of this, however, are the subject of future studies.

4.2 Structure

4.2.1 Local Order: Pair Correlation Function

To gain insight into the local structure, we first consider the *pair correlation function*. It is defined as follows:

$$g(r) = \frac{1}{4\pi r^2 \rho} \frac{1}{N-1} \left\langle \sum_{i,j}^{N} \delta(r - |\mathbf{r}_i - \mathbf{r}_j|) \right\rangle , \tag{4.1}$$

where $|\mathbf{r}_i - \mathbf{r}_j|$ is the separation between particles i and j. N is the number of particles, ρ is the number density; the average is the ensemble average. $g(r)$ is also called *radial distribution function.* It is a special kind of density, which can be summarized as follows: From the point of view of a particle, there will be (on average) $\rho g(r)$ particles at distance r per element of volume. In Figure 4.2 we show the pair correlation functions for both the prolate and the oblate systems, for several volume fractions ϕ. MC and MD data fully agree and so their average was taken. The pair correlation function shows the nearest neighbor shells as individual peaks. The higher the volume fraction, the larger the distance at which we can still see such peaks. $g(r)$ approaches unity as $r \to \infty$. The maximum represents the nearest-neighbor distance; it moves to smaller values and becomes sharper as the volume fraction is increased. Its location for the highest volume fraction is 1.131 (prolate system, $\phi = 0.598$) and 0.994 (oblate system, for both $\phi = 0.598$ and $\phi = 0.614$).

4.2.2 Intermediate Range: Static Structure Factors

The static structure factor is defined as

$$S(\mathbf{q}) = \frac{1}{N} \langle \rho^*(\mathbf{q}) \rho(\mathbf{q}) \rangle = \frac{1}{N} \left\langle \sum_{i,j}^{N} \exp[i\mathbf{q} \cdot (\mathbf{r}_i - \mathbf{r}_j)] \right\rangle , \tag{4.2}$$

where

$$\rho(\mathbf{q},t) \equiv \sum_{i=1}^{N} \exp(i\mathbf{q} \cdot \mathbf{r}_i(t))$$

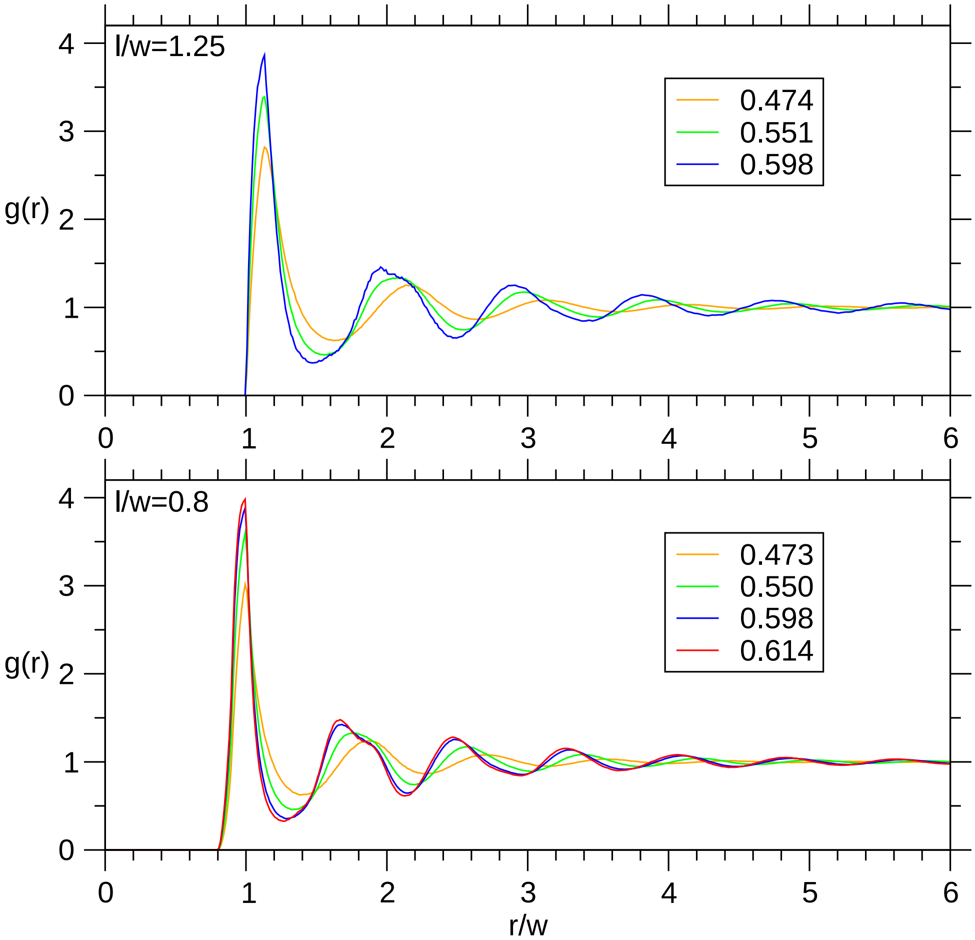

Figure 4.2: Pair correlation functions $g(r)$ for the prolate (top) and the oblate (bottom) systems, for several volume fractions ϕ (see legend). MC and MD data fully agree and so their average was taken. The maximum represents the nearest-neighbor distance; it moves to smaller values as the volume fraction is increased. Its location for the highest volume fraction is 1.131 (prolate system, $\phi = 0.598$) and 0.994 (oblate system, for both $\phi = 0.598$ and $\phi = 0.614$).

is the Fourier transform of the particle density.

$S(\mathbf{q})$ is essentially the Fourier transform of the pair correlation function. In isotropic systems, it is a function of the magnitude q only, and so we can spherically average over the directions of $\mathbf{q}$.

$S(q)$ enables us to examine structure on intermediate length scales. Even when placed in a disordered fashion, repetitiveness produced by structural units such as tetrahedra, and larger features, will produce corresponding peaks in $S(q)$. It is thus a good variable to study inhomogeneities—or prove their absence.

In Figure 4.3 we show the structure factors for both the prolate and the oblate systems, for several volume fractions ϕ. MC and MD data again fully agree and so their average was taken. The maximum represents a recurring length scale due to the neighbor spacing. It moves to higher values of q and becomes more pronounced as the volume fraction is increased. The black dotted line indicates the value $q_{\max}$ used for much of the analysis of the dynamics. It was chosen to be near the maximum over a range of volume fractions. Its value for $l/w = 1.25$ is $q_{\max} = 6.85$, and for $l/w = 0.8$ it is $q_{\max} = 7.85$. At first, it is surprising to consider the corresponding length scales: 0.92 for $l/w = 1.25$ and 0.80 for $l/w = 0.8$. How can particles be closer together than their width? The reason is that $S(q)$ does not place emphasis on the *nearest* neighbors. While the nearest neighbors are at least w (prolate) or about w (oblate) apart, the second (or nth) neighbor shell is less than $2w$ (nw) away due to the gap-filling packing geometry.[5] So $q_{\max}$ is an important length scale for the system beyond the local scale.

What we also see from Figure 4.3 is that there are no features on length scales larger than the neighbor spacing, as there are no peaks in $S(q)$ for $q < q_{\max}$. An exciting feature of glassy dynamics is that nonetheless, the dynamics *does* have correlations on larger length scales.

4.3 Average Dynamics

4.3.1 Mean Squared Displacement and Diffusion

The mean squared displacement (MSD)

$$\langle r^2(t)\rangle = \left\langle \frac{1}{N}\sum_{i=1}^{N} |\mathbf{r}_i(t) - \mathbf{r}_i(0)|^2 \right\rangle \tag{4.3}$$

is a measure of how far (on average) a particle has come after time t has elapsed. Several points in time may serve as starting points of measurement ($t = 0$), so that

---

[5] It is for this reason that we use the term “neighbor spacing”, rather than “nearest-neighbor spacing”.

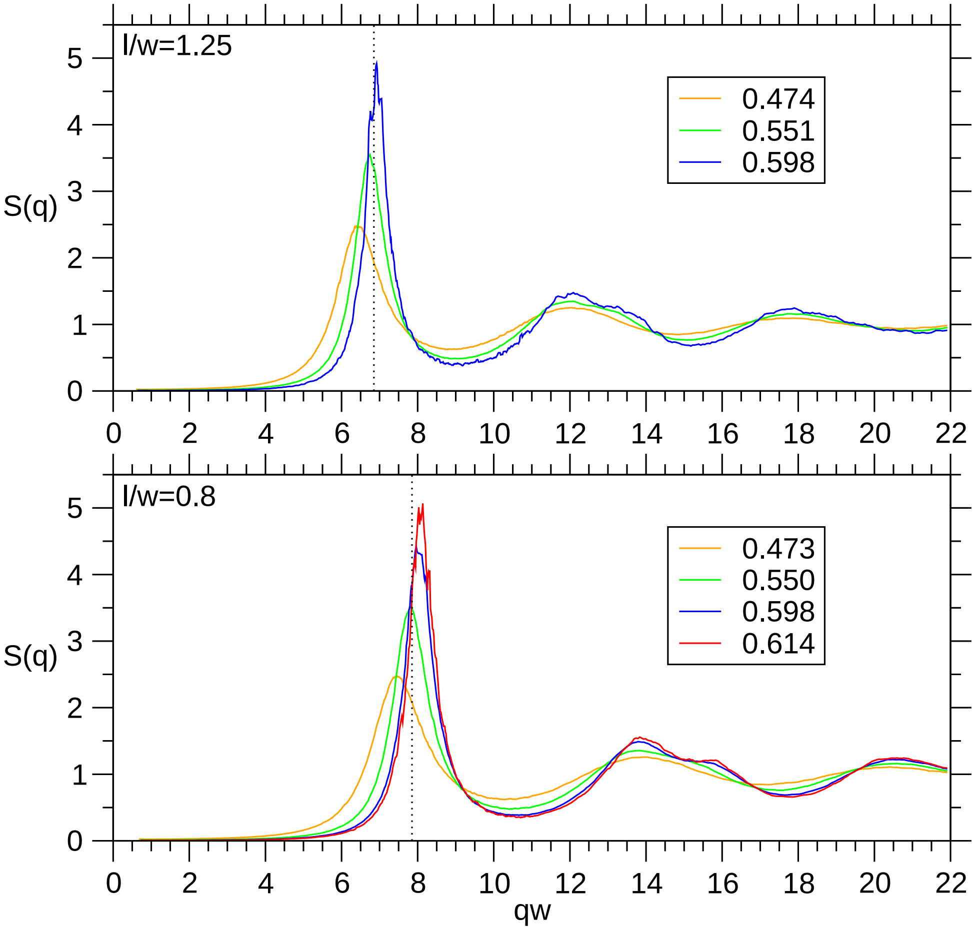

Figure 4.3: Static structure factors $S(q)$ for the prolate (top) and the oblate (bottom) systems, for several volume fractions ϕ (see legend). MC and MD data fully agree and so their average was taken. The maximum represents a recurring length scale due to the neighbor spacing; it moves to higher values of q as the volume fraction is increased. The black dotted line indicates q_{max} used for the analysis of the dynamics ($l/w = 1.25$: $q_{\text{max}} = 6.85$; $l/w = 0.8$: $q_{\text{max}} = 7.85$). There are no features for $q < q_{\text{max}}$, i.e. on length scales larger than the neighbor spacing.

we obtain several measurements during the same run. They will not be entirely uncorrelated, but nevertheless improve statistics significantly when we average over them. The angle brackets therefore indicate the ensemble average and the time average in this special sense. In our simulation, configurations were stored on logarithmic time scales, one such scale beginning at the start, and three more after $1/4$, $1/2$, and $3/4$ of the run had passed.

In Figure 4.4 we demonstrate the properties of the MSD. Each curve of the MD simulations begins with the ballistic regime, where the MSD rises quadratically, and ends with the diffusive regime, where it rises linearly in time. In the MC simulations, the initial regime also corresponds to a diffusive one, owing to the Brownian motion-like evolution. In both simulations, the transition between the initial and final regimes ranges from a slight bend at low volume fractions to a pronounced sub-diffusive regime, growing longer for increasing volume fractions. This plateau marks here the β-relaxation regime, the time scale during which particles typically remain localized (in their cages). The onset of the diffusive regime corresponds to the α-relaxation. We can thus identify features of glassy dynamics in the MSD. We note that the increase in plateau width is predicted by MCT (even quantitatively [38]). Furthermore, from the plateau height we may estimate the mean radius of the cages r_{MSD}. We obtain it by evaluating the root of the plateau height, i.e. the root-mean-squared displacement. It is near $r_{\mathrm{MSD}} \approx 0.2w$ for all systems at $\phi \geqslant 0.598$. But see Section 4.3.2.1 for our discussion on cages.

From the MSD one can compute the self-diffusion constant D, by means of the Einstein relation

$$D = \lim_{t \to \infty} \langle r^2(t) \rangle / 6t. \tag{4.4}$$

In practice, we fitted straight lines to the MSDs at large values of t and used the slopes of the fits to evaluate $D = \frac{1}{6} \cdot d\langle r^2(t) \rangle / dt$. The results are presented in Section 4.3.3.

4.3.2 Relaxation

4.3.2.1 Intermediate Scattering Functions

The intermediate scattering function is defined as follows:

$$F(q,t) = \langle \frac{1}{N} \rho^*(\mathbf{q},t) \rho(\mathbf{q},0) \rangle = \left\langle \frac{1}{N} \sum_{i,j}^{N} \exp\left[i\mathbf{q} \cdot \left(\mathbf{r}_i(t) - \mathbf{r}_j(0) \right) \right] \right\rangle \tag{4.5}$$

where $\rho(\mathbf{q},t))$ is again the Fourier transform of the number density. The average is the ensemble average (and treated numerically in the same fashion as was done

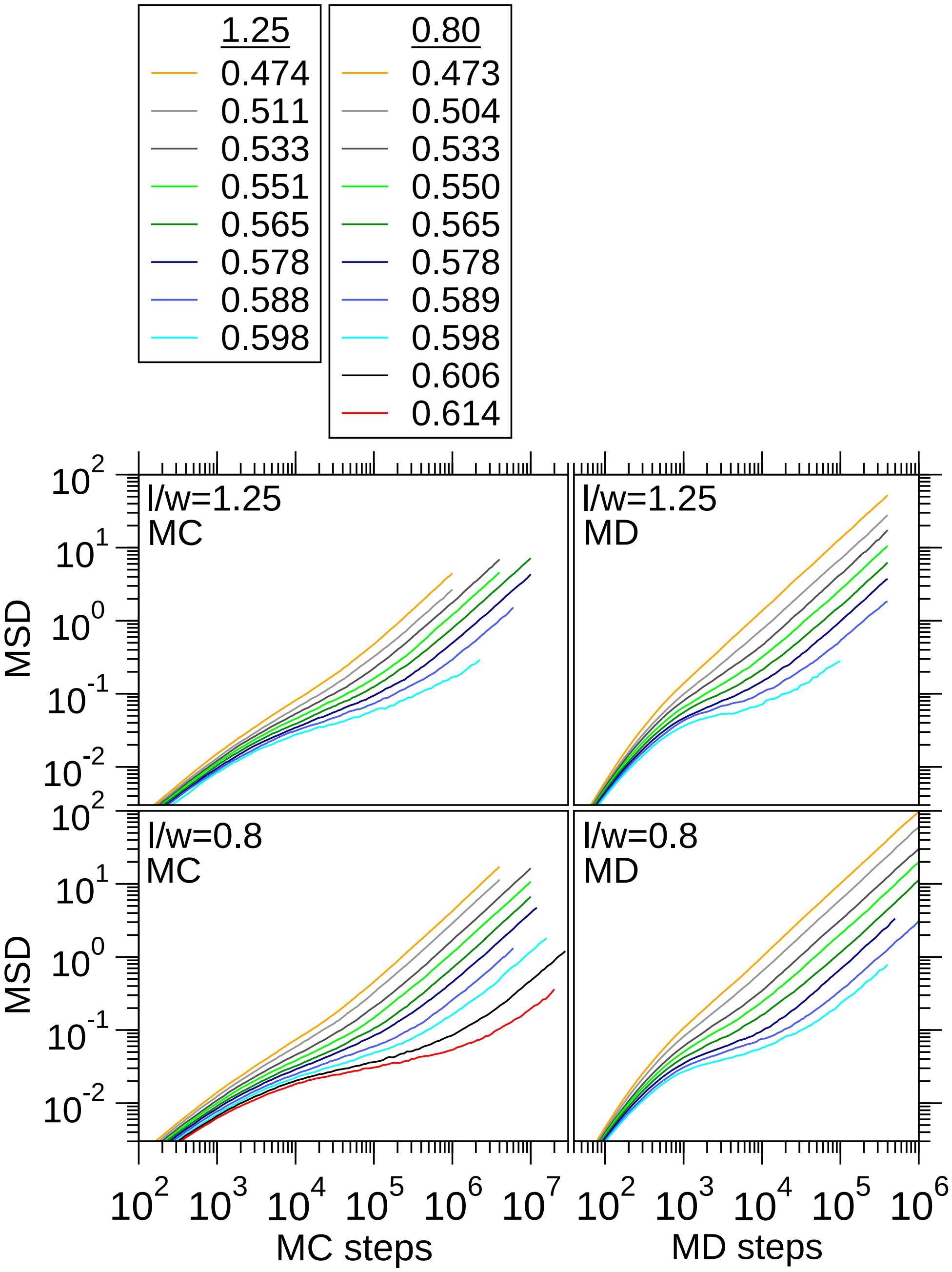

Figure 4.4: Mean-squared displacements (MSD) of all systems at several volume fractions ϕ (see legend). One can see the ballistic regime (MD only) at early time scales and the diffusive regime at late time scales. Towards high volume fractions there is a sub-diffusive regime on intermediate time scales, indicative of glassy dynamics.

for MSDs), and a spherical average over all directions of $\mathbf{q}$, once more exploiting that our systems are isotropic. Thus, $F(q,t)$ also depends only on the magnitude q of the wave vector.

We can extract from the double sum the diagonal terms, and hence write

$$F(q,t) = F_\mathrm{s}(q,t) + F_\mathrm{d}(q,t), \tag{4.6}$$

where

$$\begin{aligned} F_\mathrm{s}(q,t) &= \left\langle \frac{1}{N} \sum_{i=1}^{N} \exp\left[i\mathbf{q}\cdot(\mathbf{r}_i(t) - \mathbf{r}_i(0))\right] \right\rangle \\ F_\mathrm{d}(q,t) &= \left\langle \frac{1}{N} \sum_{i\neq j}^{N} \exp\left[i\mathbf{q}\cdot\left(\mathbf{r}_i(t) - \mathbf{r}_j(0)\right)\right] \right\rangle \end{aligned} \tag{4.7}$$

are the *self part* and the *distinct part*, respectively. These are also called *incoherent* and *coherent* intermediate scattering functions. Note that $F(q,0) = S(q)$. We will in fact always normalize $F(q,t)$ by $S(q)$ so that they start at unity and in the end decay to zero.

Roughly speaking, the self part is a measure of how much the position of the average particle is related to its own initial position, when we look at a resolution specified by q. For example, if we choose $q = 2\pi/w$, it makes essentially no difference when the particles have moved on a scale much smaller than w, so F_s is still close to unity. And it makes a big difference when the particles have moved on the order of their width w, and so F_s approaches zero. The latter condition implies that structural relaxation has occurred on that length scale. The distinct part plays the same role, but relating the position of the particle to the initial position of the average *other* particle. We do not consider it in this study.

In Figure 4.5 we show $F_\mathrm{s}(q_\mathrm{max},t)$ for all simulations, with q_max near the maximum of the static structure factor (Section 4.2.2); i.e. it corresponds to the neighbor spacing. One can clearly see the development of a plateau with increasing volume fraction. This means that there are two distinct stages of relaxation, and the later one slows down dramatically upon increase of volume fraction (note the logarithmic time scale). This two-step decay is the hall mark in glass formers [29]. As already mentioned, the conventional interpretation is in terms of particles being trapped in cages formed by their nearest neighbors. The initial decay corresponds to motion within the traps, and the final decay to escape. At high volume fractions, exceedingly cooperative rearrangements are required for escape, making such processes rare. We note that indicators of caging have not been seen in hard ellipsoids before (unless the moment of inertia was strongly increased [77]). The presence of cages is demonstrated in Section 4.4.2 (Figure 4.20 on page 90).

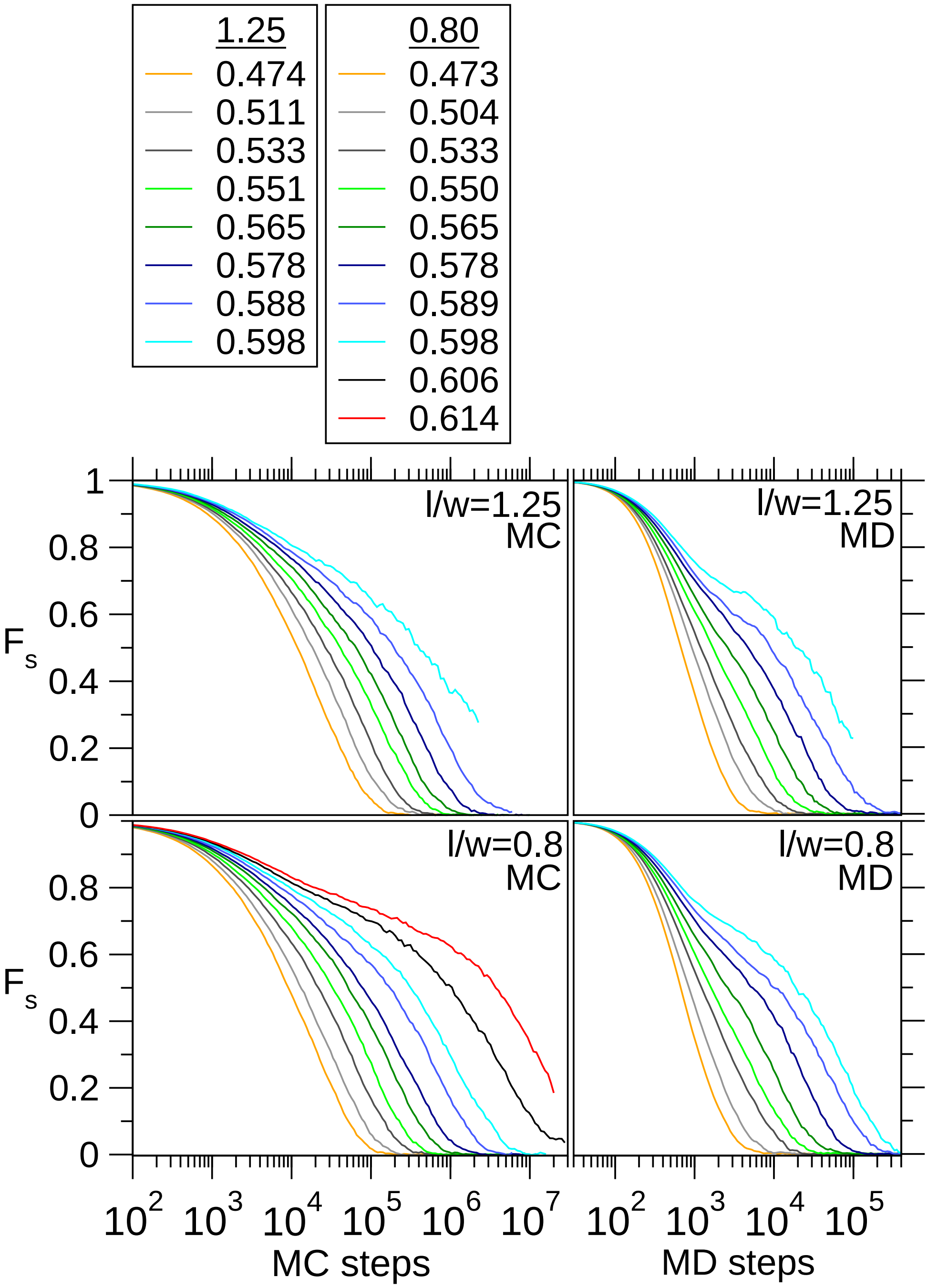

Figure 4.5: Self-intermediate scattering functions $F_s(q_{\max}, t)$ at several volume fractions ϕ (see legend), with $q_{\max}$ near the maximum of the static structure factor (see Figure 4.3). Towards high volume fractions there develops a plateau on intermediate time scales. The final relaxation is slowed down strongly with increasing volume fraction, indicative of glassy dynamics.

Inspired by Berthier and Kob [75], and in an attempt to refine the notion of cages, we consider sizes associated with the cages. We already saw in Section 4.3.1 that the localization on intermediate time scales, the “cage size”, is $r_{\mathrm{MSD}} \approx 0.2w$ in our systems. It is instructive to compare the volume which is instantaneously available to the particles; i.e. the volume with fixed nearest neighbors. We may estimate it from the end of the MC equilibration runs: The attempted translational move was randomly chosen out of a cube of volume δ_{max}^3, and δ_{max} was set in such a way that the acceptance ratio $R_{\mathrm{A}} \approx 0.3$. That is, about 30% of the moves would be accepted. Geometrically, this means that 30% of the volume of the cube δ_{max}^3 is free, on average. This fraction is small enough that the boundaries of the available volume are mostly inside δ_{max}^3, and so the product $R_{\mathrm{A}} \cdot \delta_{\mathrm{max}}^3$ yields a good estimate of this volume. In the MC production runs with small steps and $R_{\mathrm{A}} \approx 0.75$, this is no longer the case. Assuming an approximately spherical shape of the “instantaneous cage”, we may obtain its radius r_{I}:

$$\begin{aligned} R_{\mathrm{A}} \cdot \delta_{\mathrm{max}}^3 &\approx \frac{4\pi}{3} r_{\mathrm{I}}^3 \\ r_{\mathrm{I}} &\approx \sqrt[3]{\frac{3R_{\mathrm{A}}}{4\pi}}\,\delta_{\mathrm{max}} \end{aligned} \tag{4.8}$$

For $\phi = 0.598$, the prolate system has $r_{\mathrm{I}} = 0.015w$ and the oblate one $r_{\mathrm{I}} = 0.013w$, and for $\phi = 0.614$ we have $r_{\mathrm{I}} = 0.011w$ in the oblate system. This is up to a factor of 20 (!) smaller than the cage size $r_{\mathrm{MSD}} \approx 0.2w$. This has consequences for the nature of the motion within the range $r_{\mathrm{MSD}} \approx 0.2w$, local motion usually thought of as “rattling in the cage”. It must be cooperative, involving particles well beyond the nearest-neighbor shell. Cages should thus be understood as soft objects, their softness allowing motion in the range $r_{\mathrm{MSD}} \approx 0.2w$ even though the local packing is more tight at any instant.

The picture that the decay of $F_{\mathrm{s}}(q_{\mathrm{max}}, t)$ to the plateau corresponds to “rattling in the cage” was recently challenged by Berthier and Kob [75], although based on slightly different evidence. Their Monte Carlo simulations of a binary Lennard-Jones mixture (the Kob-Andersen model [51, 52]) used step sizes on the order of $\delta_{\mathrm{max}} \approx r_{\mathrm{MSD}} \approx 0.15\sigma$, but up to 10^4 MC steps were needed by the particles to actually explore the volume associated with r_{MSD}. More complex motion than vibrations in a cage was inferred.

Finally, we define the relaxation time τ associated with $F_{\mathrm{s}}(q,t)$ as the time when the named function has reached the value 0.1. We fitted a Kohlrausch-Williams-Watts function Eq. (1.12) to each curve to improve precision and to allow extrapolation for the cases when $F_{\mathrm{s}}(q,t) = 0.1$ was not reached during production.

4.3.2.2 Orientational Correlation Functions

Dynamics in the orientational degrees of freedom is observed in terms of the second-order orientational correlator [22]

$$L_2(t) = \left\langle \frac{1}{N} \sum_{i=1}^{N} \left[\frac{3}{2} \cos^2 \theta_i(t) - \frac{1}{2} \right] \right\rangle \tag{4.9}$$

where $\theta_i(t)$ is the angle between the orientation at time t and the original orientation of ellipsoid i. Since $L_2(t)$ is an even function in $\cos\theta(t)$, the head-to-tail symmetry of the particles is taken into account. Decay of this function indicates that relaxation of orientational degrees of freedom has taken place, that a substantially different orientation has been assumed by most particles. Figure 4.6 shows the orientational correlation functions. As in the intermediate scattering functions, plateaus develop at high volume fractions. Evidently, the cages hinder rotations of the ellipsoids. As a consequence, orientational and positional degrees of freedom are coupled. This is in contrast with the decoupling found at lower volume fractions [30]. The hindrance is relatively weak, however, since the plateau height is quite low.

The dip after the initial decay in the MD plots is a remnant of the free-rotator behavior of $L_2(t)$ [78, 30]. Its presence is not surprising given the low anisometry. At long times, the curves do not differ significantly among MD and MC (see Section 4.3.4.1).

As with $F_s(q,t)$, we define the relaxation time τ associated with $L_2(t)$ as the time when the named function has reached the value 0.02. Given the low plateau height, such a small number was needed to capture the α-relaxation. Also here, we fitted a Kohlrausch-Williams-Watts function Eq. (1.12) to each curve to improve precision. Extrapolation was not necessary.

The *third*-order orientational correlation function is defined as

$$L_3(t) = \left\langle \frac{1}{N} \sum_{i=1}^{N} \left[\frac{5}{2} \cos^3 \theta_i(t) - \frac{3}{2} \cos \theta_i(t) \right] \right\rangle$$

Figure 4.7 shows $L_3(t)$ for all systems, comparing it to $L_2(t)$ which is shown in grey. Unlike $L_2(t)$, the third-order correlator $L_3(t)$ shows insignificant slowing-down in the range of volume fractions studied. The implication is that head-to-tail flips, to which $L_3(t)$ is sensitive, are not affected by the slowing-down of the overall re-orientation. This is in accord with the MMCT prediction of Letz et al. [3], according to which a separate glass transition for the flipping mode occurs at a higher volume fraction. The same behavior has also been found for the case of diatomic Lennard-Jones dumbbells [79], and symmetric Lennard-Jones dumbbells [80]. The explanation [79] of this phenomenon relates to cages, in that

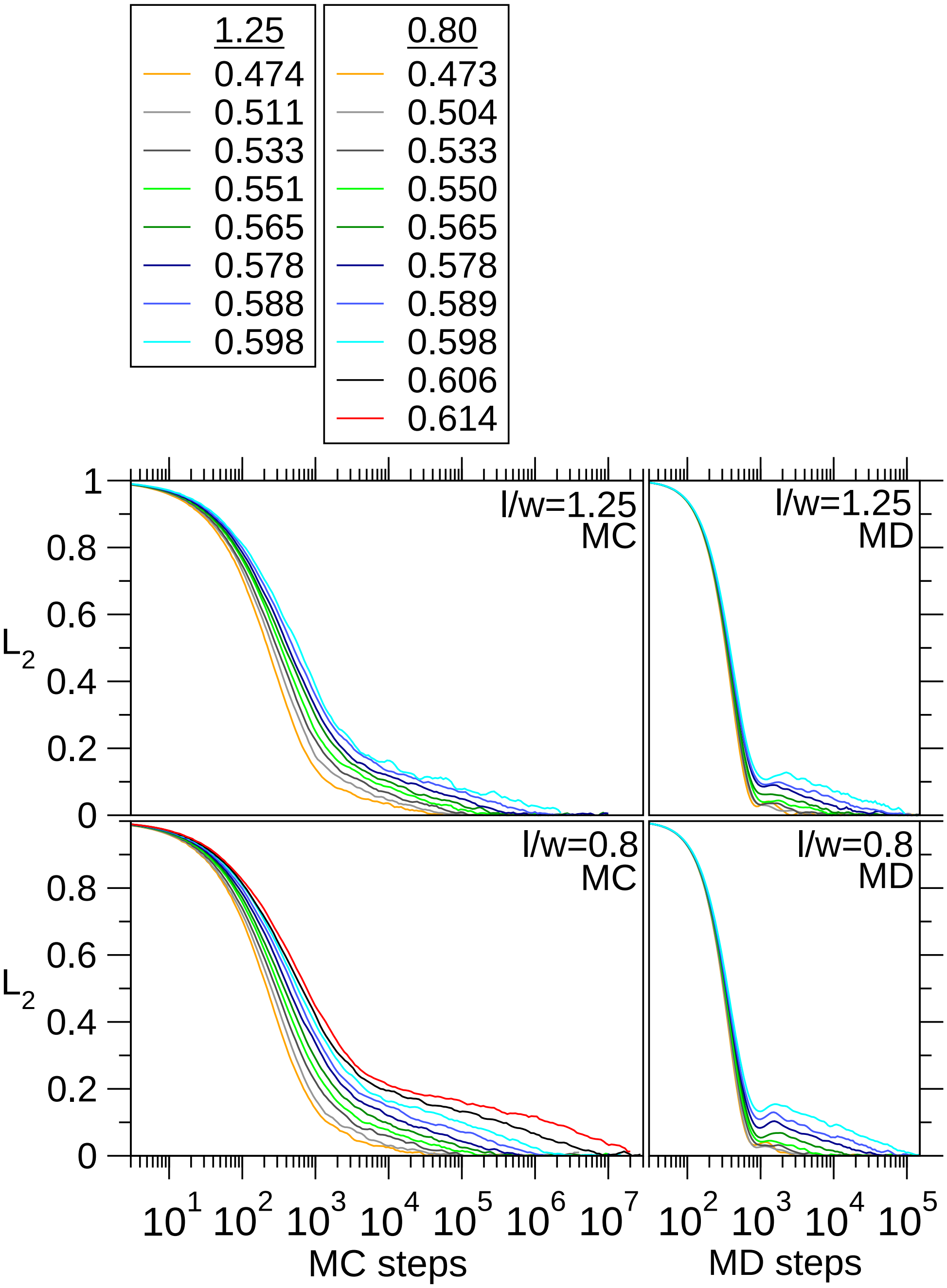

Figure 4.6: Second-order orientational correlators $L_2(t)$ at several volume fractions ϕ (see legend). Again a plateau develops with increasing volume fraction, i.e. the glassy dynamics affects the orientational degrees of freedom as well. Hence, orientational degrees of freedom are coupled to positional ones.

their fluctuating shape makes flips possible, but not significant re-orientation. This is in full agreement with the softness of cages we discussed above.

We note in passing that crystallization, if it occurs, releases the orientational degrees of freedom: The orientational correlators accelerate by three orders of magnitude and no longer have a plateau.

4.3.3 Slowing-down of Diffusion and Relaxation

We now turn to the slowing-down of diffusion and relaxation as a function of volume fraction. Figure 4.8 presents inverse relaxation times τ^{-1} obtained from $F_{\rm s}(q_{\rm max},t)$ (triangles) and from $L_2(t)$ (circles), and diffusion constants D (squares), as a function of volume fraction ϕ, for all systems. MC data: filled symbols (with lines to guide the eye); MD data: open symbols. The MC values have been multiplied by a factor of 24 (prolate) and 18 (oblate) to match the MD time scale [$L_2(t)$: 19 and 16, respectively]. Note that in each system, one common factor for the positional variables yields excellent agreement between MC and MD. According to MCT, there should be only one such value. The factor for the orientational relaxation times need not be the same since it depends on the choice of orientational move size (MC) and moment of inertia (MD). The errors are of symbol size or less. D is in units of $(2\pi/q_{max})^2/[t]$; this choice is discussed in the next paragraph. The slowing down of all variables is super-Arrhenius. According to MCT, it should approach a power law, which we will test in Section 4.3.4.4.

In Figure 4.9, we compare diffusion constants (squares) and inverse relaxation times ($F_{\rm s}$: triangles, L_2: circles) of the prolate (red, open symbols) and the oblate (blue, solid symbols) system. Having established the agreement between MC and MD, we use MC data only. The values are extremely similar, indicative of the previously observed symmetry under exchange of l/w with its inverse [1, 30, 3]. For the case of D, this is only true because of our choice of units $[D] = (2\pi/q_{max})^2/[t]$. It was in fact motivated by the discrepancy in D when using $[D] = w^2/[t]$, despite the match in the other variables. Motion in the system entails rearrangement on the micro-structural scale. Its significance is therefore best measured in terms of a structural length scale, for which the one given by q_{max} is the natural choice. We mention that using the position of the maximum in the pair correlation function $g(r)$ yields a similar agreement, while the use of the unit of length $\sqrt[3]{(l/w)}w$ (as in e.g. [23, 30]) yields an inferior agreement for our data.

4.3.4 Testing Mode-Coupling Theory

We have seen in the previous sections that dynamical variables in our systems bear the features of glassy dynamics. In the following, we demonstrate that these features are pronounced enough that predictions of MMCT can be tested.

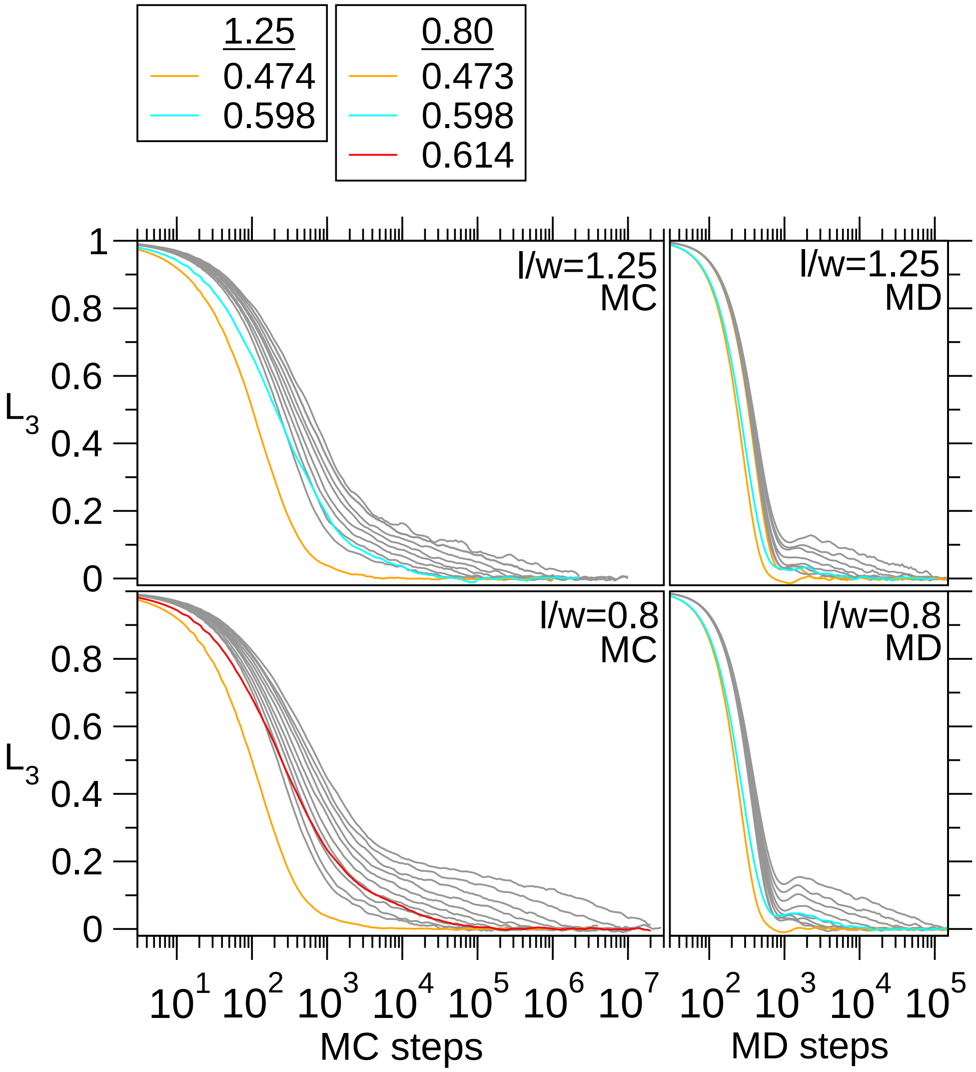

Figure 4.7: Third-order orientational correlators $L_3(t)$ at the lowest and highest simulated ϕ (see legend). Comparing to $L_2(t)$ (grey curves), they do not slow down significantly, indicating that flipping modes are not affected by the onset of glassy dynamics.

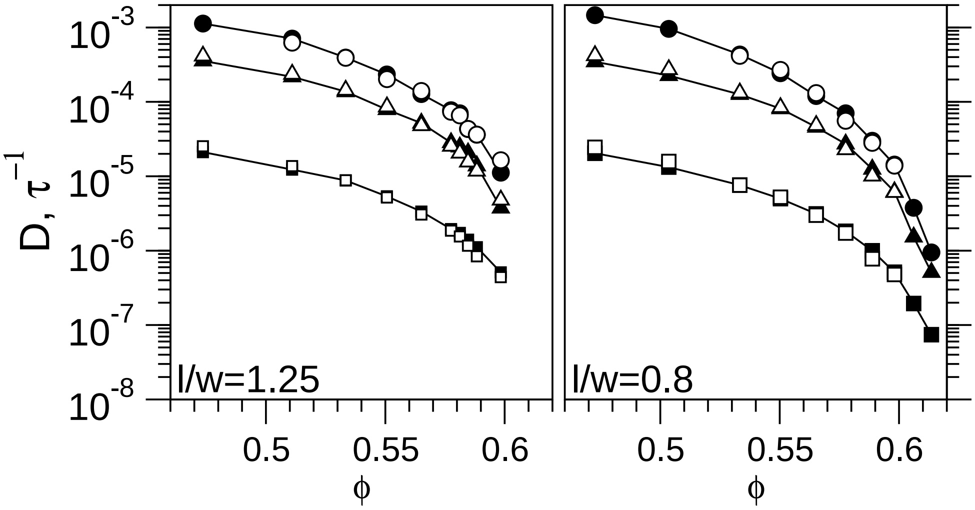

Figure 4.8: Inverse relaxation times τ^{-1} obtained from $F_s(q_{\text{max}}, t)$ (triangles) and from $L_2(t)$ (circles), and diffusion constants D (squares), as a function of volume fraction ϕ, for all systems. MC data: filled symbols (with lines to guide the eye); MD data: open symbols. The MC values have been multiplied by a factor of 24 (prolate) and 18 (oblate) to match the MD time scale [$L_2(t)$: 19 and 16, respectively]. D is in units of $(2\pi/q_{max})^2/[t]$ to account for the structural length scale given by the neighbor spacing. See Figure 4.3 for the definition of q_{max}. The plots show excellent agreement between MD and MC.

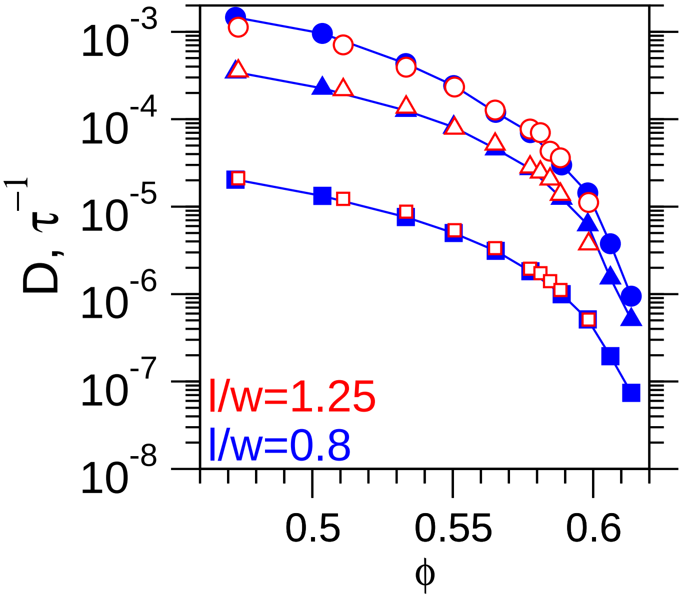

Figure 4.9: MC data of diffusion constants (squares) and inverse relaxation times (F_s: triangles, L_2: circles), comparing the prolate (red, open symbols) and the oblate (blue, solid symbols) system. The data are extremely similar, indicative of symmetry under exchange of l/w with its inverse; this is seen in D as well, thanks to the choice of units $[D] = (2\pi/q_{max})^2/[t]$.

4.3.4.1 MD vs. MC

As mentioned in Section 1.4.2, MCT (and MMCT) predicts that the long-time dynamics of a system is independent from the microscopic dynamics (i.e. simulation method), apart from an overall time shift. In Section 4.3.3 we already established that this holds for relaxation times and diffusion constants. The statement goes further, however, in that the shape of correlators should also not depend on simulation method. This property has been verified in the Kob-Anderson model [81] and the polydisperse hard-sphere glass [56]. We now check whether our two simulation methods also produce the same shape of correlators on long time scales.

In Figure 4.10, we superpose the intermediate scattering functions $F_{\mathrm{s}}(q_{\max},t)$ from MC (black) and MD (green) for all volume fractions ϕ. The lowest and highest volume fractions are annotated. The MD functions have been rescaled in t to match with the MC data at long times. For $\phi < 0.598$ the ratio of individual relaxation times was used; for $\phi = 0.598$, more precise adjustment lead to multiplication of MD times by 21.0 ($l/w = 1.25$) and 16.67 ($l/w = 0.8$). This individual rescaling is superior to using the overall shift since the fluctuations in decay time may obscure the fact that the shapes match well. From the Figure we see excellent agreement with the MMCT prediction.

We perform the analogous test for the orientational correlators $L_2(t)$ (Figure 4.11). The lowest three volume fractions have been omitted since there is essentially no long-time regime. As before, the MD functions have been rescaled in t to match with the MC data at long times (the ratio of relaxation times was used except for $l/w = 1.25$, $\phi = 0.598$, where we multiplied MD times by 19). Apart from statistical fluctuations, the long-time dynamics are confirmed to be independent of the microscopic dynamics. To our knowledge, this is the first test of this MMCT prediction for orientational degrees of freedom.

Finally, we return to $F_{\mathrm{s}}(q,t)$ and compare the long-time shapes for $\phi = 0.598$ and wave vectors in the range $2.8 \leq qw \leq 18$. The MD functions of each system have been rescaled in t by one common factor to match with the MC data at long times ($l/w = 1.25$: multiplied by 21.0; $l/w = 0.8$: multiplied by 16.67). The shapes match well over this wide range of wave vectors after 10^5 time units, even for the case of $l/w = 1.25$ which has poor statistics.

4.3.4.2 Time-Volume Fraction Superposition Principle

Asymptotically close to the glass transition, all correlators should obey the time-volume fraction superposition principle. It states that the correlators map onto a single curve in the β- and α-relaxation regimes when rescaled in their time dependence using t/τ (τ is the α–relaxation time). Thus, a master curve should be seen after the initial decay to the end of the final decay.

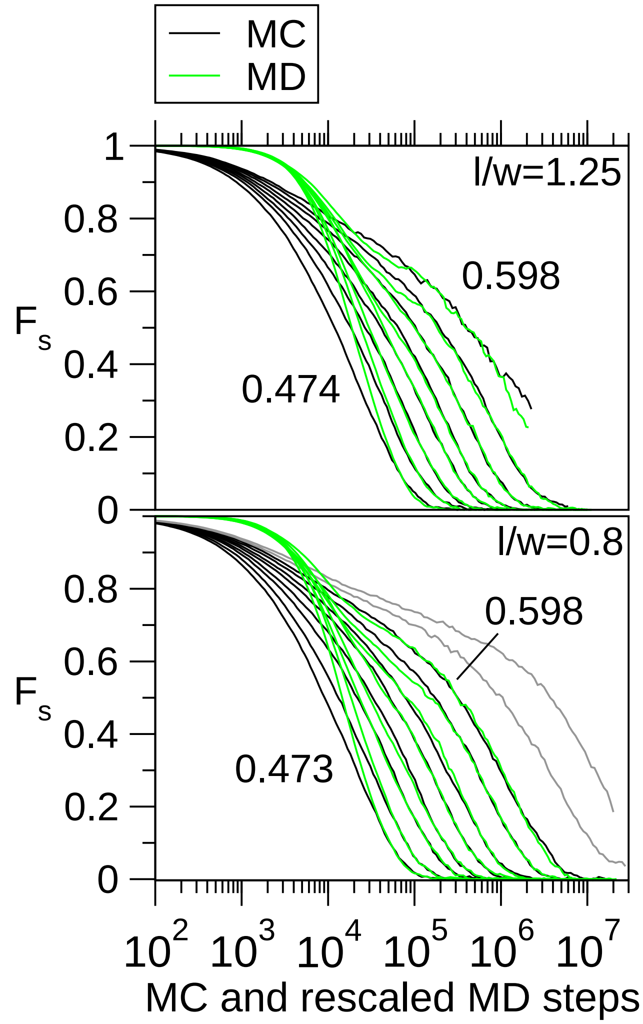

Figure 4.10: Comparing the long-time shapes of the intermediate scattering functions $F_s(q_{\max}, t)$ from MC and MD for all volume fractions ϕ. The lowest and highest volume fractions are annotated. The MD functions have been rescaled in t to match with the MC data at long times [for $\phi < 0.598$ the ratio of relaxation times was used; for $\phi = 0.598$, more precise adjustment lead to multiplication of MD times by 21.0 ($l/w = 1.25$) and 16.67 ($l/w = 0.8$)]. Excellent agreement is found with the (M)MCT prediction that the long-time dynamics not depend on microscopic dynamics (i.e. simulation method).

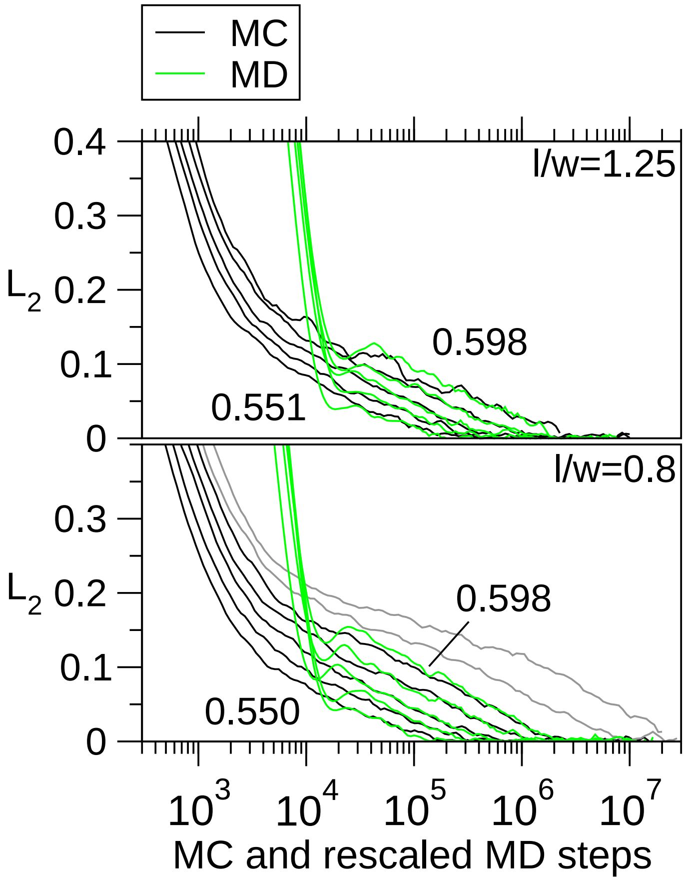

Figure 4.11: Comparing the long-time shapes of the second-order correlators $L_2(t)$ from MC and MD for the range of ϕ as annotated. The MD functions have been rescaled in t to match with the MC data at long times (the ratio of relaxation times was used except for $l/w = 1.25$, $\phi = 0.598$, where we multiplied MD times by 19). Apart from statistical fluctuations, the long-time dynamics are confirmed to be independent of the microscopic dynamics.

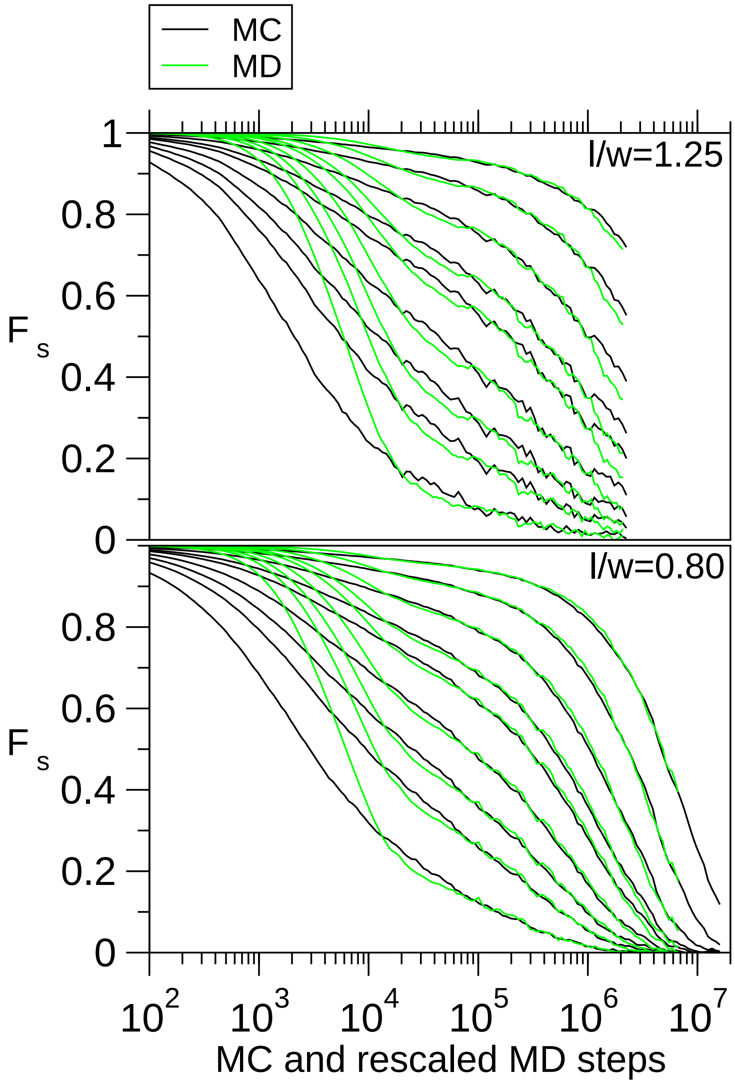

Figure 4.12: Comparing the long-time shapes of the intermediate scattering functions from MC and MD, for $\phi = 0.598$ and wave vectors in the range $2.8 \leq qw \leq 18$. The MD functions of each system have been rescaled in t by one common factor to match with the MC data at long times ($l/w = 1.25$: multiplied by 21.0; $l/w = 0.8$: multiplied by 16.67). The shapes match well over this wide range of wave vectors after 10^5 time units, even for the case of $l/w = 1.25$ which has poor statistics.

In Figure 4.13, we display all $F_\mathrm{s}(q_\mathrm{max}, t/\tau)$, to look for the collapse to a master curve for the highest volume fractions. Two curves seem to violate the prediction: the cyan one in $l/w = 1.25$ MC ($\phi = 0.598$), and the black one in $l/w = 0.80$ MC ($\phi = 0.606$). The deviation of both is of statistical origin, since it has the size of the fluctuations in the curves along absolute simulation time. The effect is more drastic for the cyan curve in $l/w = 1.25$ MC since the relaxation time had to be determined by extrapolation. This extrapolation poses an additional source of error to the calculated relaxation time. The two outliers do not change the conclusion that the superposition principle holds.

Analogously, we have rescaled all $L_2(t)$, to look for the same property in orientational degrees of freedom. The results are reported in Figure 4.14. In the MD data, some of the lowest volume fractions' curves are not considered as the near-vanishing plateau made it impossible to extract the relaxation time. The MMCT prediction is clearly confirmed.

4.3.4.3 Von Schweidler Law and Factorization Property

Next, we focus on the q-dependence of the intermediate scattering functions at high volume fractions ϕ. The upper panels of Figures 4.15 and 4.16 present these functions for all systems at the highest available volume fraction, with wave lengths in the range $2.8 < qw < 18$. The plateau height is a monotonic function of q. For larger q (i.e. smaller length scales), the plateau is lower, since local motion will already lead to significant decay of $F_\mathrm{s}(q,t)$. For smaller q, the plateau is higher, since the same local motion is insignificant on larger length scales and thus will lead to little decay. We test two MMCT predictions for the vicinity of the glass transition (see Section 1.4.2), the von Schweidler law and the factorization property.

For the late stages of the plateau and the early stages of the final decay, these functions should be well-fitted by the von Schweidler law (incl. the second-order correction), $F_\mathrm{s}(q,t) = f_q^c - h_q^{(1)} t^b + h_q^{(2)} t^{2b}$. f_q is the plateau height, and is called non-ergodicity parameter. $h_q^{(\mathrm{i})}$ are amplitudes, and b is a system-universal exponent, also independent of the microscopic dynamics. Agreement is excellent, as shown for the examples in Figures 4.15 and 4.16 (red lines). The ranges for the fits are presented in Table 4.2. MC and MD data of both the prolate and the oblate system are consistent with $b = 0.65 \pm 0.2$. The range of values for b is so large because the quality of the fits is rather insensitive to b.

Figure 4.17 shows the q-dependence of the fit parameters in the von Schweidler law. Given the same shape of $F_s(q,t)$, but shifted by a constant factor in time, $h_q^{(\mathrm{i})}$ will be trivially different; to allow for a comparison of the MC and MD results, we rescaled $h_q^{(\mathrm{i})}$ of the MD fits to match time scales. $h_q^{(1)}$ of $l/w = 1.25$

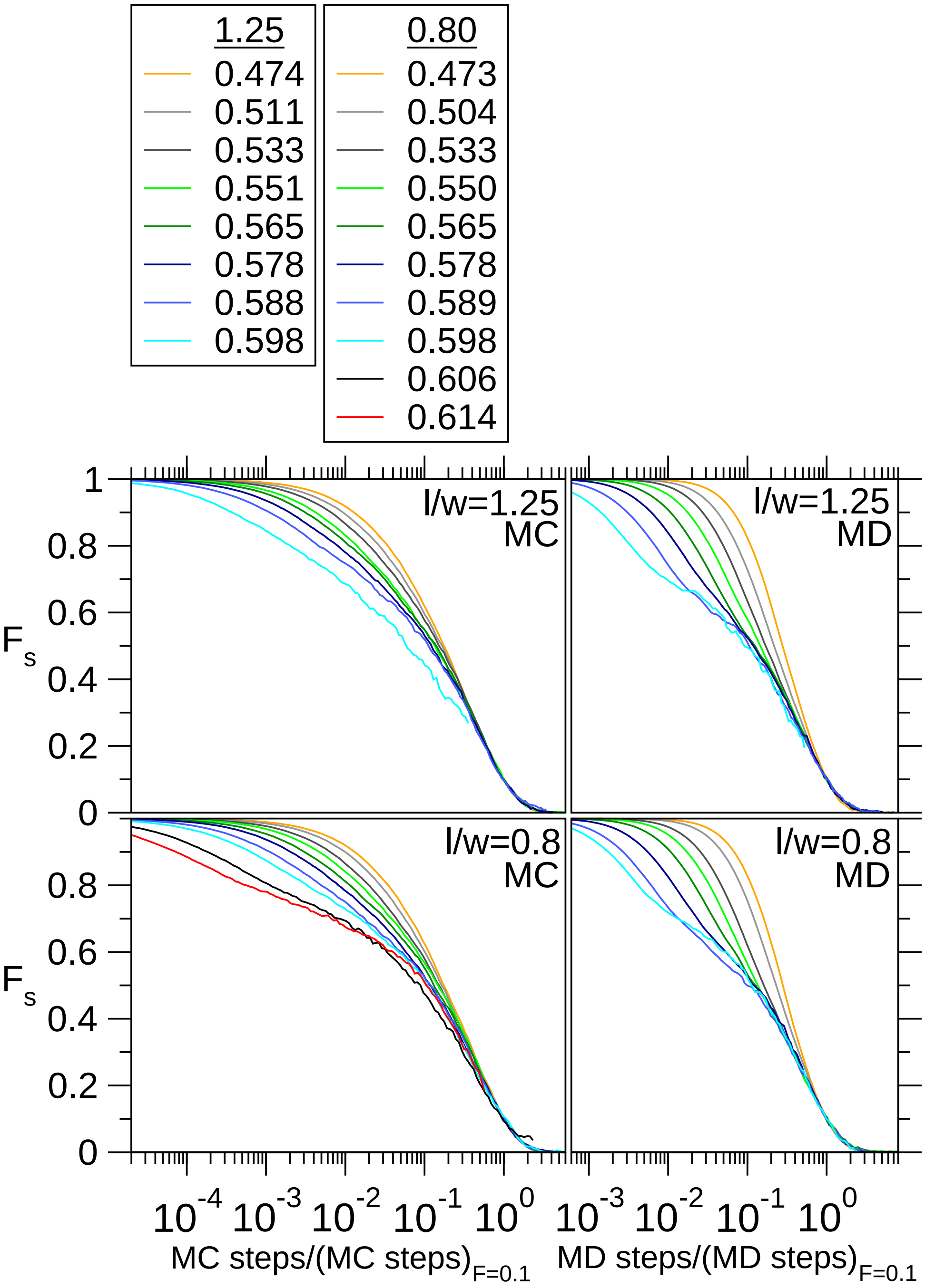

Figure 4.13: Time-volume fraction superposition principle for $F_s(q_{\max}, t)$. All curves have been rescaled by their relaxation time τ to check whether a master curve results, as MCT predicts for the vicinity of the glass transition. Two curves seem to violate the prediction: the cyan one in $l/w = 1.25$ MC ($\phi = 0.598$), and the black one in $l/w = 0.80$ MC ($\phi = 0.606$). The deviation of both is of statistical origin, and the deviation of the former is aggravated by the uncertainty due to extrapolation when determining τ. The two outliers do not change the conclusion that the superposition principle holds.

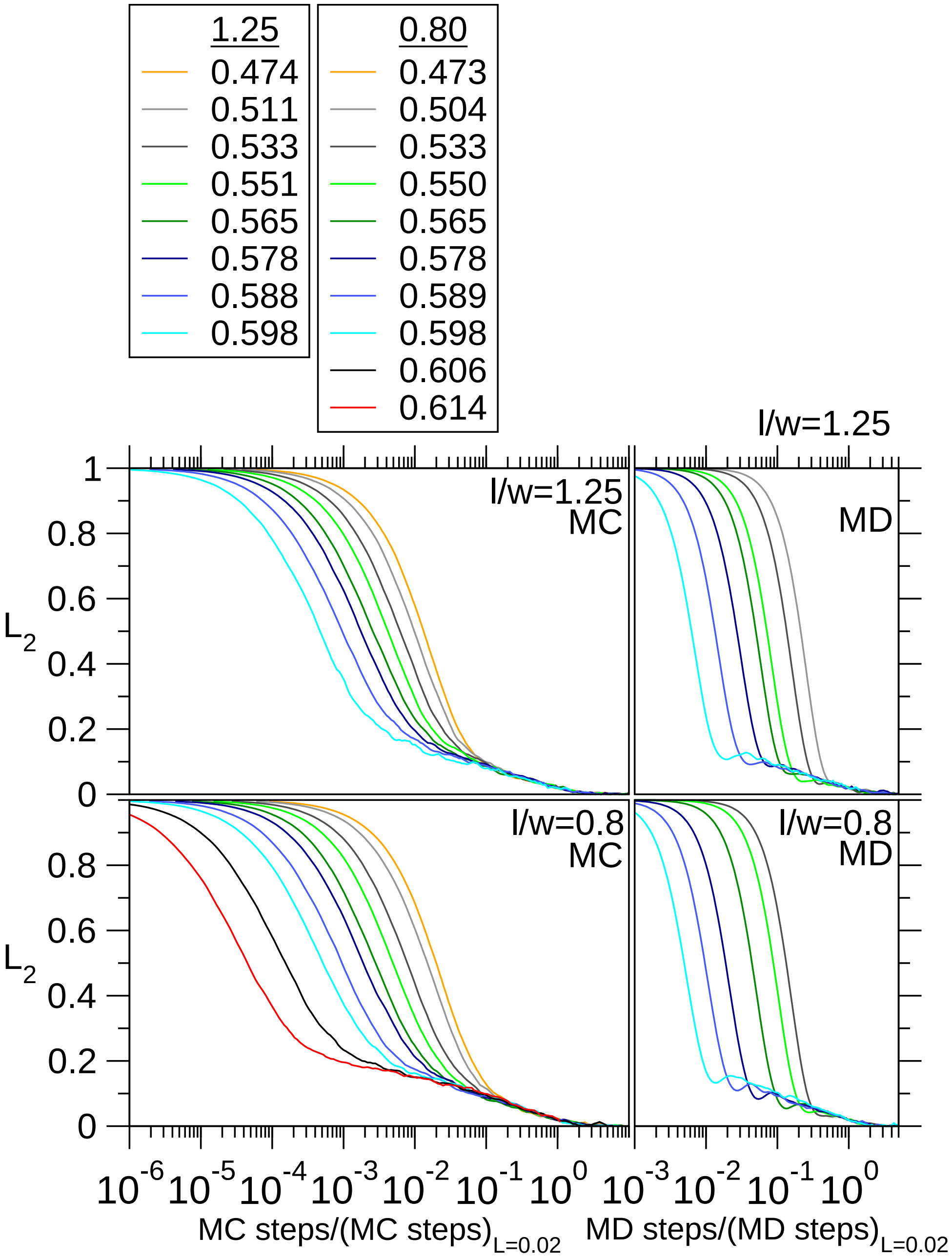

Figure 4.14: Time-volume fraction superposition principle for $L_2(t)$. All curves have been rescaled by their relaxation time to check whether a master curve results, as MMCT predicts for the vicinity of the glass transition. In the MD data, some of the lowest volume fractions' curves are not considered as the near-vanishing plateau made it impossible to extract the relaxation time. The MMCT prediction is clearly confirmed.

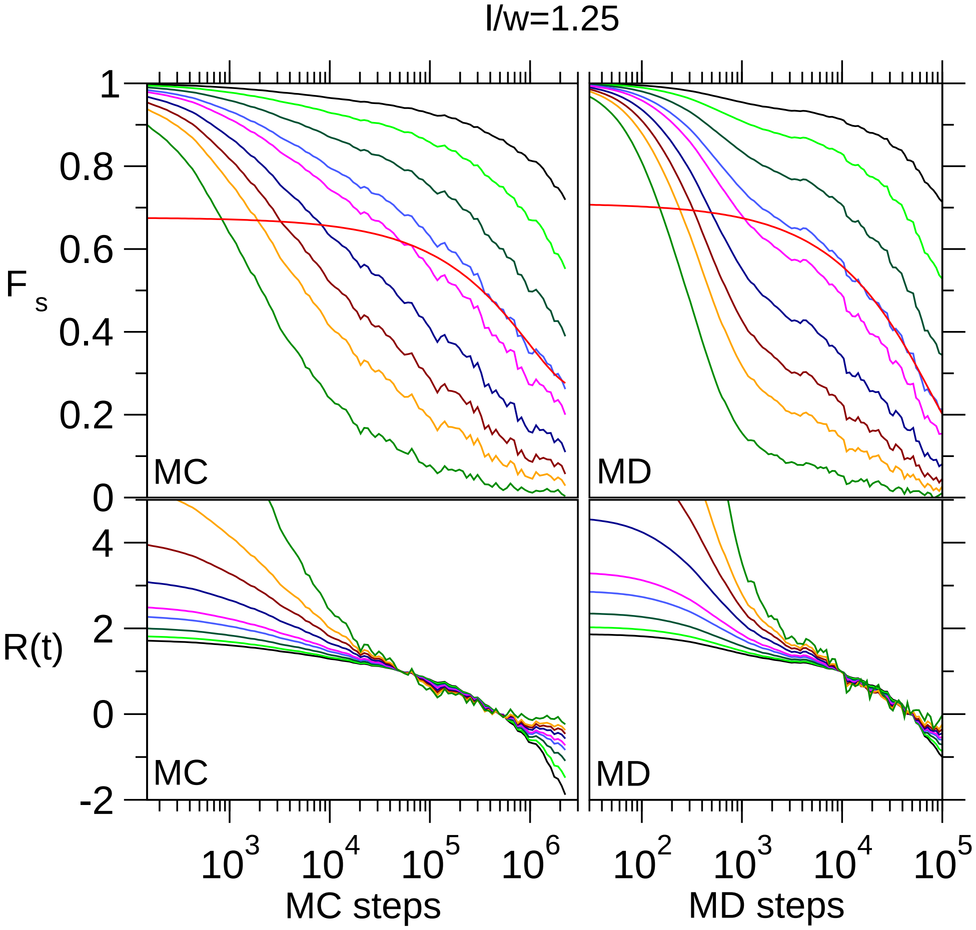

Figure 4.15: Upper panels: $F_s(q,t)$ for $l/w = 1.25$ and the highest volume fraction $\phi = 0.598$, and for q-vectors (from top) 2.8, 4.0, 5.5, 7.1, 8.1, 10.1, 12.1, 14.1, 18.1. The red lines show examples of the von Schweidler fit $F_s(q,t) = f_q - h_q^{(1)} t^b + h_q^{(2)} t^{2b}$ with $b = 0.65$. Lower panels: the same correlators after transformation to $R(t) = [F_s(q,t) - F_s(q,t_1)]/[F_s(q,t_2) - F_s(q,t_1)]$, demonstrating the factorization property. The color code, distinguishing wave vectors, shows that the curves remain ordered, i.e. a curve which is above another one before the collapse is above the other one after as well.

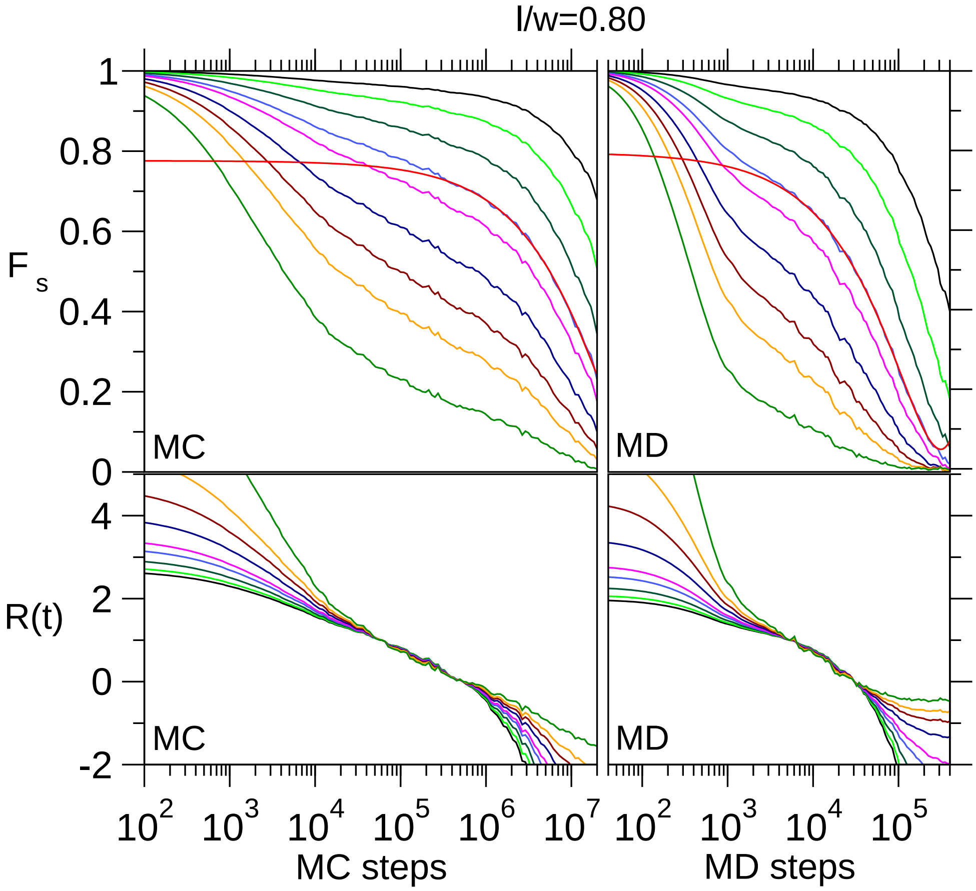

Figure 4.16: Same as Figure 4.15, but for $l/w = 0.80$; $\phi = 0.614$ for MC and $\phi = 0.598$ for MD.

	1.25				0.80			
	MC		MD		MC		MD	
	t_1	t_2	t_1	t_2	t_1	t_2	t_1	t_2
fit range	$4 \cdot 10^5$	$2 \cdot 10^6$	$1 \cdot 10^4$	$1 \cdot 10^5$	$2 \cdot 10^5$	$2 \cdot 10^6$	$7 \cdot 10^3$	$3 \cdot 10^5$
			$\phi = 0.614$:		$3 \cdot 10^5$	$2 \cdot 10^7$		
fact. prop.	$5 \cdot 10^4$	$5 \cdot 10^5$	$1 \cdot 10^4$	$5 \cdot 10^4$	$6 \cdot 10^4$	$5 \cdot 10^5$	$5 \cdot 10^3$	$3 \cdot 10^4$

Table 4.2: Fit ranges for the von Schweidler fits and reference times for the transformation to $R(t)$ testing the factorization property. $\phi = 0.598$ unless otherwise indicated.

(MD) was rescaled by 21.0^b, and of $l/w = 0.8$ (MD) by 16.67^b (the same factors as in Section 4.3.4.1); $h_q^{(2)}$ was rescaled by the squared value in each case. f_q^c resembles a Gaussian in all cases. For the highest $\phi = 0.614$, $l/w = 0.8$ (MC), the curve can in fact be well fitted by $f_q^c = \exp(-r_\mathrm{L}^2 q^2)$, with the localization length $r_\mathrm{L} = 0.072$ (red dashed line). Only for $q > 16$ arises notable deviation.

Even though a fit to a Gaussian is less satisfactory for the systems at $\phi = 0.598$, we observe qualitatively similar behavior from Figure 4.17. And to have an estimate for the localization length in the prolate $l/w = 1.25$ system, we quote the fitted values: $r_\mathrm{L} = 0.087$ (MD) and $r_\mathrm{L} = 0.091$ (MC). All these values are close to the Lindemann criterion for the melting of a solid [82]. These results are similar to MCT calculations and simulations of hard spheres [83, 56], and simulations of asymmetric Lennard-Jones dumbbells [53, 84], and silica [55]. We confirm $r_\mathrm{L} = r_\mathrm{MSD}/\sqrt{6}$, which one expects from power-expanding the exponential in $F_s(\mathbf{q}, t)$ and performing the spherical average. Finally, we remark that the curves of the MC and MD data deviate from one another, but this deviation is within the error resulting from changes in b or the fitting range.

The fitted values of $h_q^{(\mathrm{i})}$ are presented in the lower two panels of Figure 4.17. They are more sensitive to b and the fitting range, and accordingly, MC and MD results deviate appreciably. Qualitatively, we find the same behavior as in other glass formers throughout [83, 56, 53, 55], consisting of a maximum and for $h_q^{(2)}$ a zero-crossing at small values of qw. In summary, then, the q-dependence in the von Schweidler fits bears strong similarity with those in other glass formers.

We now turn to the factorization property. Recall that where the $F_\mathrm{s}(q,t)$ are near their plateaus, they should obey $F_\mathrm{s}(q,t) = f_\mathrm{q}^c + h_\mathrm{q} G(t)$, where h_q is an amplitude, and $G(t)$ is a system-universal function. This relation entails that $F_\mathrm{s}(q,t)$ can be split into a q-dependent and a t-dependent part. To test this property for our systems, we transform $R(t) = [F_\mathrm{s}(q,t) - F_\mathrm{s}(q,t_1)]/[F_\mathrm{s}(q,t_2) - F_\mathrm{s}(q,t_1)]$, as done in Gleim and Kob [48], where t_1 and t_2 are times in the regime where the property holds. Since $R(t)$ is not a function of q, all correlators should fall onto a single master curve. Moreover, the curves should remain ordered, i.e. a curve which is above another on the left-hand side remains above the other on the right-hand side. The lower panels of Figures 4.15 and 4.16 demonstrate the validity of the factorization property, and from the color we see that indeed they remain ordered. The property holds for one decade, and in $l/w = 0.8$ (MC) at $\phi = 0.614$ for two decades. Table 4.2 has the reference times t_1 and t_2 we used.

4.3.4.4 MCT Glass Transition Volume Fraction

We noted in Section 4.3.3 that the slowing-down of diffusion and relaxation is stronger than an Arrhenius law. According to MMCT, it should approach a power

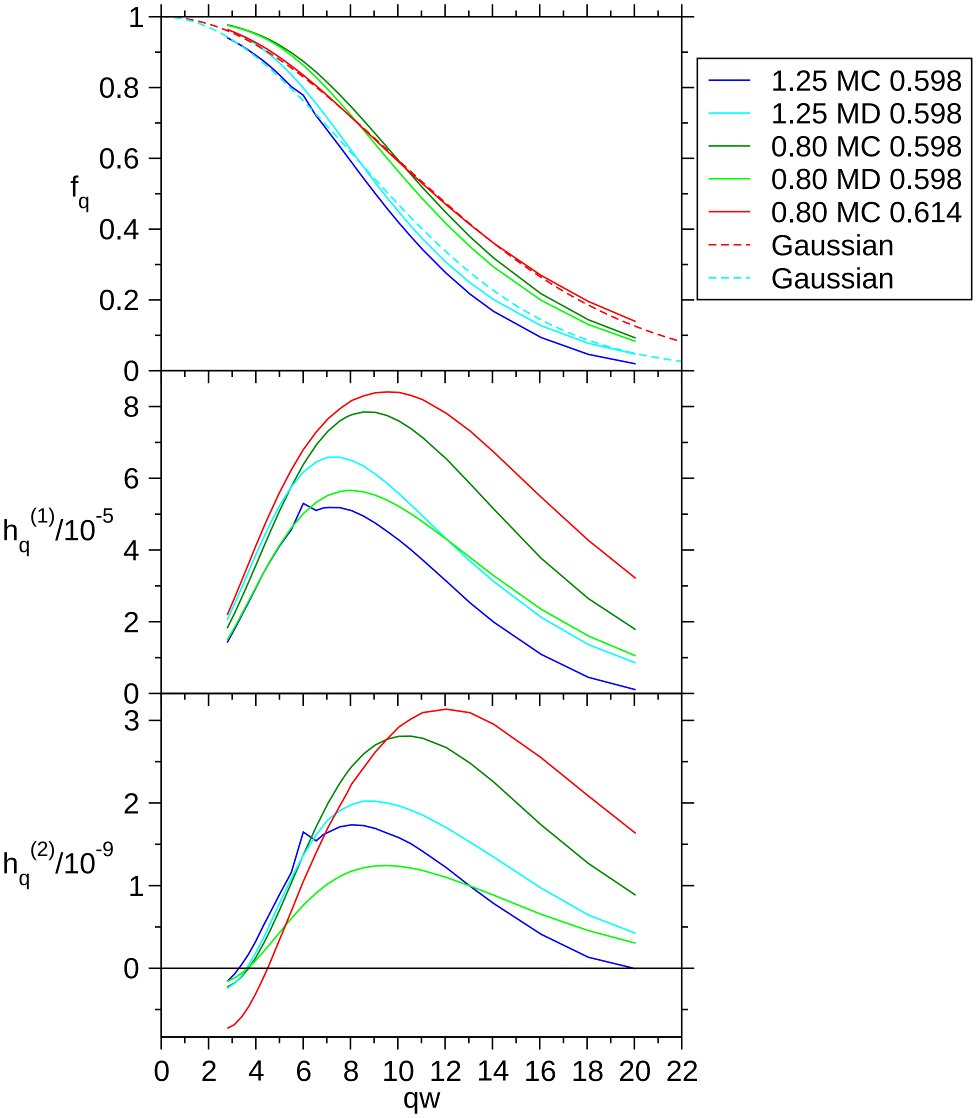

Figure 4.17: q-dependence of the fit parameters in the von Schweidler law $F_s(q,t) = f_q - h_q^{(1)} t^b + h_q^{(2)} t^{2b}$. See legend for aspect ratio, simulation method, and volume fraction. $h_q^{(1)}$ of $l/w = 1.25$ (MD) was rescaled by 16.67^b, and of $l/w = 0.8$ (MD) by 21.0^b; $h_q^{(2)}$ was rescaled by the squared value in each case. f_q resembles a Gaussian, and for $\phi = 0.614$, $l/w = 0.8$ (MC) the curve can in fact be well fitted, up to $q = 16$, by $f_q = \exp(-r_L^2 q^2)$, with the localization length $r_L = 0.072$ (red dashed line). For $\phi = 0.598$, $l/w = 1.25$ (MD) we show the corresponding fit (cyan dashed line, $r_L = 0.087$) which is less satisfactory.

law of the form $D \propto \tau^{-1} \propto (\phi_\mathrm{c} - \phi)^\gamma$, where ϕ_c is the MMCT glass-transition volume fraction, and γ is related to the von Schweidler exponent b via Eq. (1.13). Both ϕ_c and γ should be system-universal. In Figure 4.18 we demonstrate the validity of this prediction for $F_\mathrm{s}(q,t)$ for several values of q (from top: $l/w =$ 1.25: qw = 6.85, 11, 16; $l/w = 0.8$: qw = 7.85, 16, 20) and for L_2 (bottom). The exponent $\gamma = 2.3$ was chosen in agreement with $b = 0.65$. The straight-line fits comply with a common $\phi_\mathrm{c} = 0.615 \pm 0.005$ for the prolate system and with $\phi_\mathrm{c} = 0.618 \pm 0.005$ for the oblate system. The fact that there is a common value for positional and orientational relaxation times further demonstrates the strong coupling of these degrees of freedom. We also note the agreement of MC and MD data. The values we found for ϕ_c differ from the MMCT predictions of Letz et al. [3], viz. $\phi_\mathrm{c} = 0.540$ and 0.536 ($l/w = 1.25$ and 0.8, respectively). The mismatch between the numerical MCT calculations based on static structure, and scaling law fits based on simulated dynamics is, however, not unusual [52, 85] and has been attributed to activated ("hopping") processes for which MCT does not account. A similar mismatch is found in the hard-sphere system [56]. We will find in Section 4.4.2 that the dynamics has features of hopping. Hopping (or jumps) has a second consequence for the present discussion: the associated events have a strong effect on the diffusion constant, causing the scaling law $D \propto (\phi_\mathrm{c} - \phi)^\gamma$ to produce a different exponent. For this reason D is not included in Figure 4.18. This decoupling of diffusion and structural relaxation is also common in glass formers [86, 87, 88].

4.4 Heterogeneous Dynamics

4.4.1 Non-Gaussian Parameter

As the volume fraction is increased, and the dynamics become more glassy, the mobility of the particles is no longer the same everywhere in the system. This dynamical heterogeneity [89, 90] can be detected [90] with the non-Gaussian parameter (NGP) [91], which is defined as follows:

$$\alpha_2(t) = \frac{3\left\langle r(t)^4 \right\rangle}{5\left\langle r(t)^2 \right\rangle^2} - 1 \tag{4.10}$$

where $r(t) = |\mathbf{r}(t) - \mathbf{r}(0)|$ is the scalar displacement of a particle during the time interval t. The NGP measures the deviation of the distribution of particle displacements from a Gaussian one. In a perfectly homogeneous system, the Central Limit Theorem implies that this distribution must be Gaussian. However, if there are now several classes of particles with various mobilities, the distribution becomes more complicated and deviates from a Gaussian one.

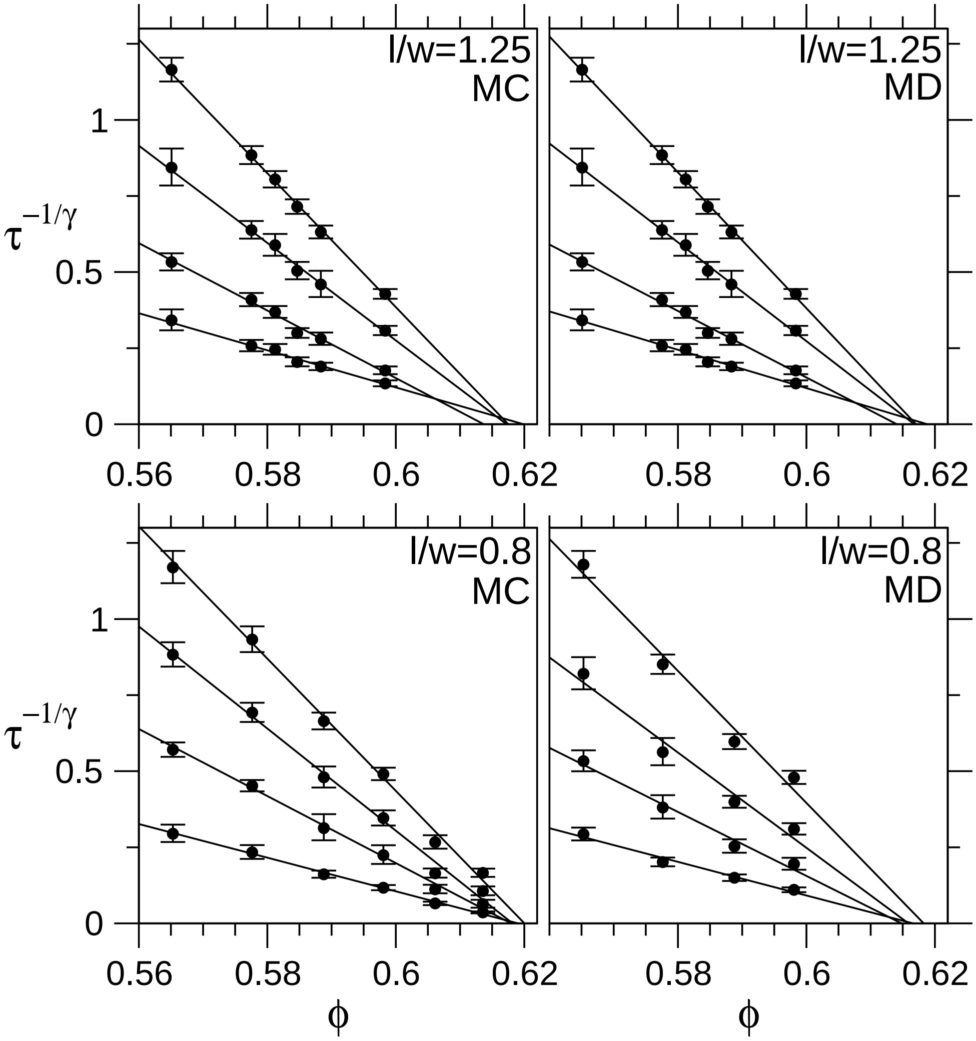

Figure 4.18: $\tau^{-1/\gamma}$ multiplied by arbitrary factors for clarity, from $F_s(q,t)$ (from top: $l/w = 1.25$: qw = 6.85, 11, 16; $l/w = 0.8$: qw = 7.85, 16, 20) and L_2 (bottom), demonstrating the validity of the MCT scaling law $\tau^{-1} \propto (\phi_c - \phi)^{\gamma}$. The exponent $\gamma = 2.3$ was chosen in agreement with $b = 0.65$. The straight-line fits indicate a glass transition volume fraction of $\phi_c = 0.615 \pm 0.005$ (prolate system) and $\phi_c = 0.618 \pm 0.005$ (oblate system). MC and MD data agree.

Figure 4.19 shows the NGP for all systems. On short time scales, the distribution of displacements is close to the Gaussian one, so that the NGP is near zero. Towards higher volume fractions, a maximum develops, and its position on the time axis coincides with the departure from the plateau in the intermediate scattering function, i.e. with the onset of the α-relaxation, when particles begin to leave cages. On long time scales, when cages have been left by most particles, the Central Limit Theorem applies to the correspondingly larger displacements, and the Gaussian distribution is recovered. The curves for all systems are similar in magnitude for equal volume fractions.

Hence, the dynamics becomes heterogeneous when the development of the system is governed by the cage effect. Given that there are classes of particle mobility[6], the question is in what way the fast particles' motion differs from that of slower ones. We consider this issue in the following section. The spatial correlations of mobility are the subject of a future publication.

4.4.2 Jumps

It has in other glass formers been demonstrated that as the glass transition is approached, the systems' evolution is dominated by non-Fickian, jump-like motion [92, 93, 94, 95, 96, 97, 98, 88]. In particular, Chaudhuri et al. [88] have recently proposed a model whereby localized motion (in the cage) combines with quasi-instantaneous jumps (cage-to-cage) to produce an exponential tail in the self-part of the van Hove correlation function; the tail was confirmed for several glass formers. Although we have insufficient data to study the tail in our system, we have studied the trajectories of individual particles in our most over-compressed system, the MC simulation of $l/w = 0.8$ at $\phi = 0.614$, to test for the presence of jumps.

From the non-Gaussian parameter (lower left panel in Figure 4.19) we see that dynamical heterogeneities in this system are strongest after about $5 \cdot 10^6$ MC steps. Thus, if jumps make fast particles fast, then we should find them in their trajectories during such intervals. In Figure 4.20 we show a representative trajectory of a fast particle, i.e. whose scalar displacement is large over that period. The individual positions are separated by 10^4 MC steps. One can clearly see the particle's visits to three cages, and that such visits last much longer than transit from one cage to another. Hence the cage picture is confirmed for this system. The size of the cages agrees with the result from the mean-squared displacement, $r_{\mathrm{MSD}} \approx 0.2w$ (Section 4.3.1). For a slow particle, only one such cage would be visible. We also observe that moving to a new cage may later be followed by the

---

[6] Or at least a systematic variation of mobility, which may be continuous and hence defy the definition of classes.

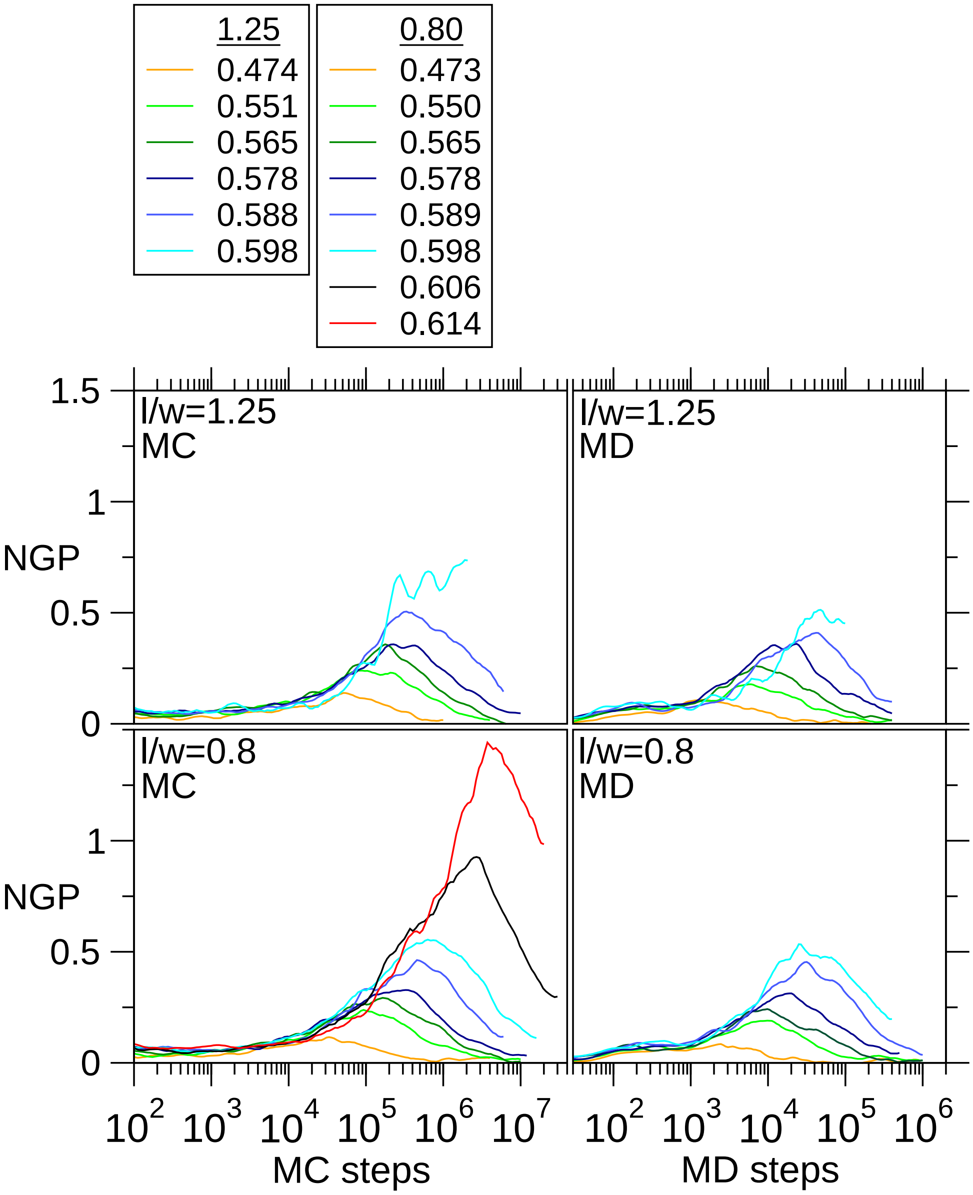

Figure 4.19: Non-Gaussian parameter for all systems. Towards higher volume fractions, a maximum develops, and its position on the time axis coincides with the departure from the plateau in the intermediate scattering function. Hence, the dynamics becomes heterogeneous when the development of the system is governed by the cage effect. When most particles escaped from their cages, the associated larger displacements dominate and follow a Gaussian distribution, making the non-Gaussian parameter zero again.

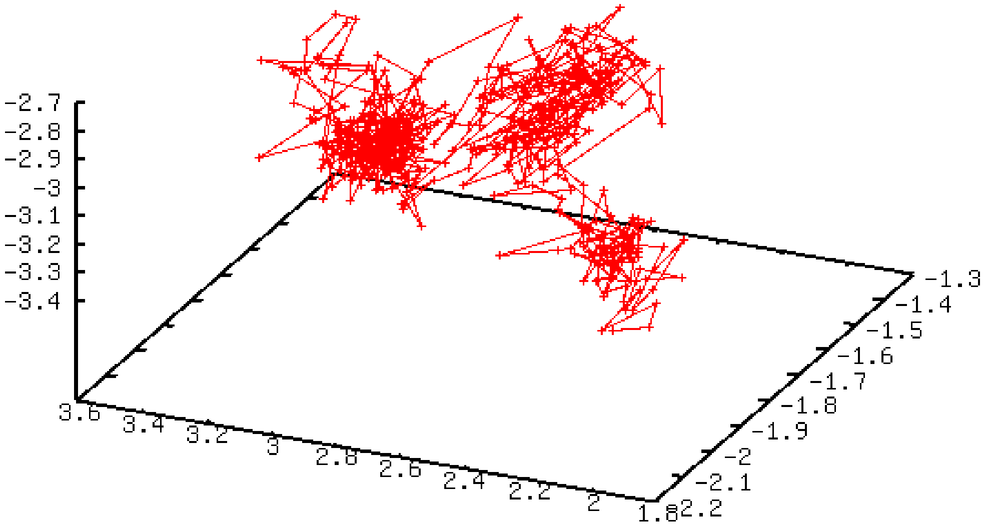

Figure 4.20: Trajectory of a fast particle from the MC simulation of $l/w = 0.8$ at $\phi = 0.614$. Three cages can be identified, whose size agrees with the result from the mean-squared displacement, $r_{\mathrm{MSD}} \approx 0.2w$. Moving to a new cage may later be followed by the return to the previous cage. The displacements between individual positions are of similar size within a cage and during transit.

return to the previous cage.

But notice in Figure 4.20 that the displacements between individual positions are of similar size within a cage and during transit. Corresponding pictures in previous studies suggest the same for the binary Lennard-Jones mixture [88] (Kob-Andersen model [51, 52]), colloidal hard spheres [92], and a 2D, bidisperse granular system [93]. Therefore, we suspect quite generally that a jump does not involve an exceptional displacement. Rather, the displacement (or series of displacements) leading to the new cage happens to be permanent, i.e. it is not undone by motion in the opposite direction.

We demonstrate in the following that fast particles indeed do not perform outstanding displacements. For a well-defined distinction of fast and slow particles, we consider the self-part of the van Hove correlation function [99] in its spherically-averaged form:

$$G_{\mathrm{s}}(r,t) = \frac{1}{4\pi r^2} \left\langle \frac{1}{N} \sum_{i}^{N} \delta[r - |\mathbf{r}_i(t) - \mathbf{r}_i(0)|] \right\rangle$$

It is the distribution of scalar displacements r in an interval t; the mean of the squares of these displacements is just the MSD. In Figure 4.21 we display the named function for several values of t, in linear (top) and semi-logarithmic (bottom) plots. The curves are normalized to unit area. The largest value of t corresponds to maximal dynamical heterogeneity, i.e. where the Non-Gaussian parameter (Figure 4.19) has its maximum. The dotted vertical lines indicate several regimes of mobility into which we sort the particles for further analysis.

We have calculated the distributions of displacement dr of each particle during the shorter intervals of 10^5 MC steps, for each of the mobility regimes. The intervals of 10^5 MC steps overlapped with each other to exclude the chance of splitting a jump in half or missing it. If jumps were to proceed in exceptional displacements, we should be able to see them in the curves of the fast particles, but not in those of the slower ones.

Figure 4.22 shows the distributions in linear (top) and semi-logarithmic (bottom) plots. The shape of the curves is the same from the fastest down to the slowest set of particles. Fast particles merely show an overall shift of their short-term displacements towards larger values, and not the addition of few large displacements to an otherwise similar distribution. Hence, we have confirmed for this system our suspicion that jumps do not involve exceptional displacements. We mention that the distributions of displacements during shorter intervals, e.g. 10^4 MC steps, lead us to the same conclusion. Note that not even this overall shift is necessary for a particle to leave a cage; it suffices if displacements combine their directions to make a significant, longer-lasting displacement. It is not surprising, however, that a mobile region allowing cage rearrangements also allows larger short-term displacements.

4.5 Summary

We have performed molecular dynamics and Monte Carlo simulations of the hard-ellipsoid fluid for nearly spherical ellipsoids. In this very simple anisometric model we observed glassy dynamics sufficiently strong that MCT asymptotic scaling laws could be tested and were found to apply. This includes time-volume-fraction superposition, factorization property, von Schweidler law, and the scaling laws of the slowing-down of relaxation. We found strong coupling of positional and orientational degrees of freedom, leading to a common value for the glass-transition volume fraction ϕ_c for positional and orientational relaxation times ($l/w = 1.25$: $\phi_c = 0.615 \pm 0.005$, $l/w = 0.80$: $\phi_c = 0.618 \pm 0.005$). Flipping modes, on the other hand, were not slowed down significantly. We also demonstrated in considerable detail that the results are independent of simulation method, as predicted by MCT. Further, we determined that even intra-cage motion must be cooperative, and identified an associated softness in the cages which trap the particles. We confirmed the presence of dynamical heterogeneities associated with the cage effect. The transit between cages was seen to occur on short

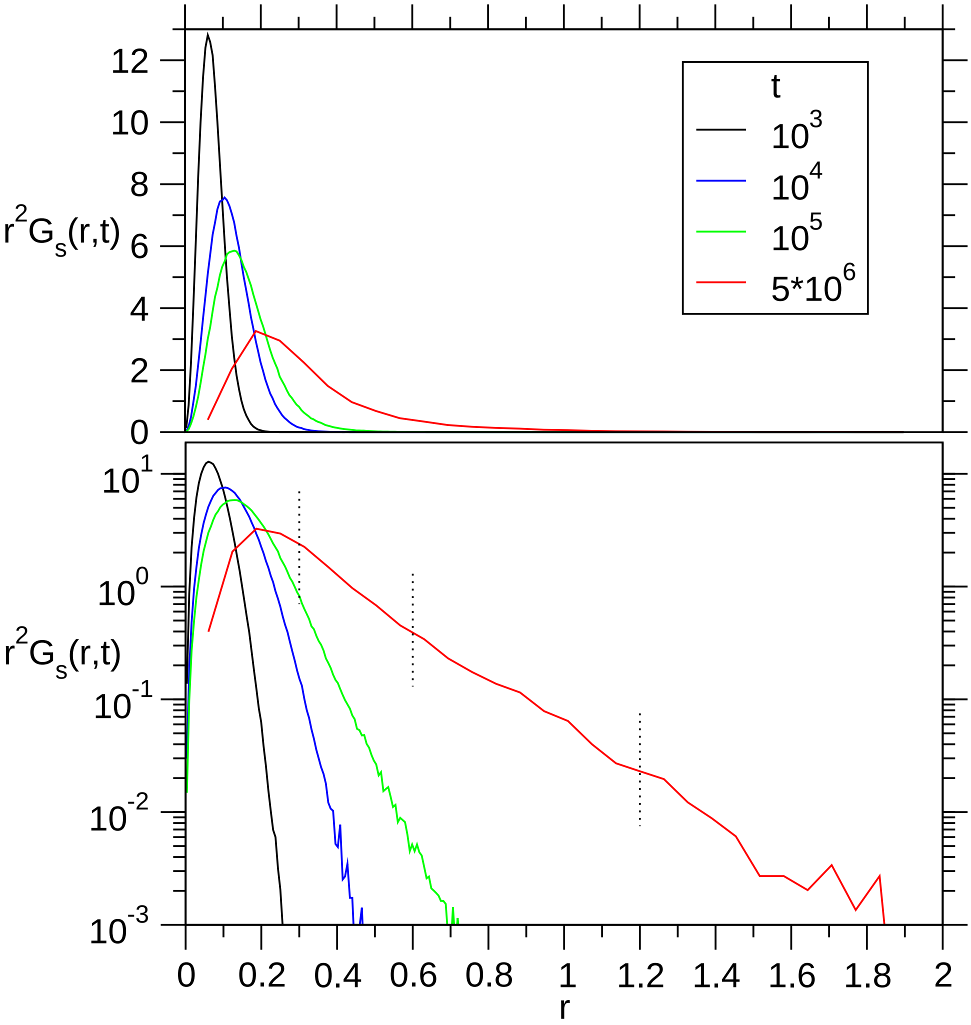

Figure 4.21: Self part of the van Hove correlation function (times r^2) for several values of t, in linear (top) and semi-logarithmic (bottom) plots, from the MC simulation of $l/w = 0.8$ at the highest volume fraction $\phi = 0.614$. It is the distribution of scalar displacements r in the interval t. The curves are normalized to unit area. The largest value of t corresponds to maximal dynamical heterogeneity, i.e. where the non-Gaussian parameter (Figure 4.19) has its maximum. The dotted vertical lines indicate the partitioning of particles according to their mobility for further analysis.

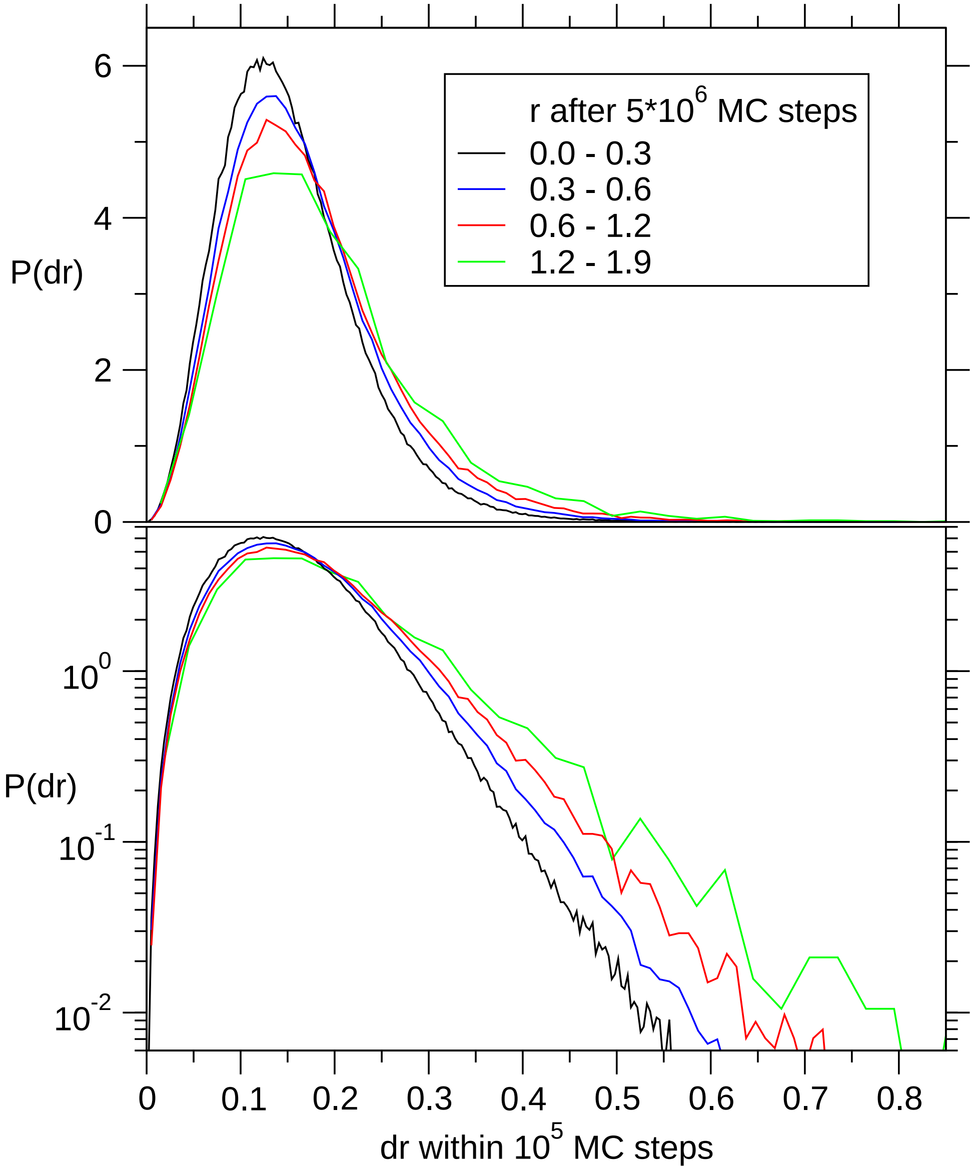

Figure 4.22: Normalized distributions of scalar displacements during intervals of 10^5 MC steps, on linear (top) and semi-logarithmic (bottom) plots, from the MC simulation of $l/w = 0.8$ at the highest volume fraction $\phi = 0.614$. The particles were separated into sets of various mobilities on a longer time scale ($5 \cdot 10^6$ MC steps; see also Figure 4.21). The shape of the curves is essentially the same from the fastest down to the slowest set of particles. Fast particles show an overall shift of their short-term displacements towards larger values, and not the addition of few large displacements to an otherwise similar distribution.

time scales, compared to the time spent in cages; but the transit was shown not to involve displacements distinguishable in character from intra-cage motion.

The presence of glassy dynamics has been predicted by MMCT [3]. However, as MMCT cannot make a statement about crystallization, a test by simulation was required. We stress that glassy dynamics is unusual in monodisperse systems. Crystallization typically intervenes unless polydispersity, network-forming bonds or other asymmetries are introduced. We argue that particle anisometry acts here as a sufficient source of disorder to prevent crystallization. This sheds new light on the question of which ingredients are required for glass formation. Recent advances of dynamic confocal microscopy with colloidal ellipsoids [37] seem promising for a study of the glassy dynamics in ellipsoids.

Acknowledgments

I would like to thank (names had to be removed in this online version):

- My supervisor, for hiring me into her group, her patience and her kind support
- My second supervisor, for his support
- The head of the group, for admitting me into his group already for my Master thesis, and for encouraging and supporting me in many ways
- Various people, for stimulating discussions and support
- Various people, for their critical reading of this text
- Many present and former group members, for stimulating discussions and support
- A professor in the UK, for sharing his MD code
- Three people whom I co-supervised with great pleasure. The work of one of them is included in this thesis; her contribution is summarized on on page 55
- The computing support in the group, for keeping things up and running and answering many questions
- The Zentrum für Datenverarbeitung at the Universität Mainz, for maintaining a cluster I extensively used
- The Deutsche Forschungsgemeinschaft (SFB TR6 and Emmy Noether), and the EU Network of Excellence SoftComp, for financial support
- The Forschungszentrum Jülich, for granting CPU time
- You, for reading this.

Appendix A

Corrected Constant-Pressure Ensemble

We left off in Section 2.1.2.1 with the partition function Eq. (2.8) in the constant-pressure-zero-tension ensemble:

$$\begin{aligned} Z(N,P,T) \quad = \quad & \int_{-\infty}^{\infty} d\ln h_{11} d\ln h_{22} d\ln h_{33} dg_{12} dg_{13} dg_{23} \int_{0}^{1} d\mathbf{s}^N \int_{4\pi} d\mathbf{u}^N \cdot \\ & \exp\{-[U(\{\mathbf{s}_i\},\mathbf{H},\{\mathbf{u}_i\})+PV(\mathbf{H})]/k_\mathrm{B}T+(N+3)\ln V(\mathbf{H})\} \end{aligned} \tag{A.1}$$

We abbreviate it to

$$Z(N,P,T) = \int_{-\infty}^{\infty} d\ln h_{11} d\ln h_{22} d\ln h_{33} dg_{12} dg_{13} dg_{23} z_{PT}^{-V(\mathbf{H})} Z_A(N,\mathbf{H},T) \tag{A.2}$$

by defining

$$Z_A(N,\mathbf{H},T) \equiv \int_{0}^{1} d\mathbf{s}^N \int_{4\pi} d\mathbf{u}^N \exp\{-U(\{\mathbf{s}_i\},\mathbf{H},\{\mathbf{u}_i\})/k_\mathrm{B}T+(N+3)\ln V(\mathbf{H})\}$$

and using once more the “fugacity” $z_{PT} = e^{P/k_\mathrm{B}T}$.

Constant-pressure MC is sufficient when $Z_A(N,\mathbf{H},T)$ is only a function of V, and not a function of g_{ij} or the ratios h_{ii}/h_{jj}; i.e., when it is independent of box shear and box aspect ratio. This is essentially the case for homogeneous fluids [57]. The task is once more to integrate out the associated degeneracies, keeping track of resulting weight factors for the remaining variables.

The g_{ij} already specify box shear independently from box size (unlike $h_{ij} = h_{jj}g_{ij}$). With $Z_A(N,\mathbf{H},T)$ invariant under changes in shear, we may carry out the integration over g_{ij}. A complication arises from the fact that the limits of this integral are infinite so that it does not converge. But for the present discussion, this is not a problem. Recall that the integrations over the angular variables in Section 2.1.2.1 yielded factors of 4π and 2π, which we then disposed of due to their irrelevance. This means that the actual value of the integral does not matter. The appropriate change of variables beforehand is the critical step. For the case of g_{ij}, we already have the correct set of variables. Instead of integration, we then simply drop the integral to obtain

$$Z(N,P,T) = \int_{-\infty}^{\infty} d\ln h_{11} d\ln h_{22} d\ln h_{33} z_{PT}^{-V(\mathbf{H})} Z_A[N,V(\mathbf{H}),T]$$

Our final task is to remove the degeneracy in box aspect ratios. We wish to integrate over $\ln h_{ii}$ such that $\ln V$ remains constant. Hence, we are interested in an appropriate change of variables such that one of them is $\ln V$. Consider that

$$\ln h_{11} + \ln h_{22} + \ln h_{33} = \ln V$$

and notice that this equation has the form of a plane:

$$x + y + z = c \tag{A.3}$$

A.3 specifies a plane perpendicular to the direction $\sqrt{1/3}(1,1,1)$. $\sqrt{1/3} \cdot c$ is its distance from the origin, which is proportional to $\ln V$. The set of values of $\ln h_{ii}$, which is in $\mathbb{R}^3$, has therefore subsets in the form of parallel planes which correspond to constant volume. The value of the latter is determined by the distance of the plane from the origin. If we now rotate to a new coordinate system where these planes are perpendicular to the x-axis, we have a set of variables with one carrying the volume and the other two orthogonal to it, allowing integration over box shapes of equal volume. Thus, our task is to find a rotation to a new set of variables x', y', z' such that $x' = \sqrt{1/3} \cdot c$. The following matrix provides this rotation:

$$\mathbf{R} = \begin{bmatrix} \sqrt{1/3} & \sqrt{1/3} & \sqrt{1/3} \\ -\sqrt{1/2} & \sqrt{1/2} & 0 \\ -\sqrt{1/6} & -\sqrt{1/6} & \sqrt{2/3} \end{bmatrix}$$

and ones easily verifies that $\det \mathbf{R} = 1$ and $\mathbf{R}^T \mathbf{R} = \mathbf{I}$. The transformation to the new variables is

$$\begin{aligned} x' &= \sqrt{1/3}(x+y+z) \\ y' &= \sqrt{1/2}(y-x) \\ z' &= \sqrt{1/6}(2z-x-y) \end{aligned}$$

and we find in x' exactly what we wanted. We note that the radicals will enter the partition function as prefactors which we can ignore. Our change of variables is then

$$\ln h_{11}, \ln h_{22}, \ln h_{33} \longrightarrow \ln(h_{11}h_{22}h_{33}), \ln(\frac{h_{22}}{h_{11}}), \ln(\frac{h_{33}^2}{h_{11}h_{22}})$$

The Jacobian of a rotation is unity, so that the partition function becomes

$$Z(N,P,T) = \int_{-\infty}^{\infty} d\ln V d\ln(\frac{h_{22}}{h_{11}}) d\ln(\frac{h_{33}^2}{h_{11}h_{22}}) z_{PT}^{-V(\mathbf{H})} Z_A[N,V(\mathbf{H}),T]$$

With regard to the actual integration over $\ln(\frac{h_{22}}{h_{11}})$ and $\ln(\frac{h_{33}^2}{h_{11}h_{22}})$, we have the same situation as for g_{ij}, and once more we realize that the actual value of the integral is immaterial; the change of variables was the important step. We have

$$Z(N,P,T) = \int_{-\infty}^{\infty} d\ln V z_{PT}^{-V(\mathbf{H})} Z_A[N,V(\mathbf{H}),T]$$

so that the final result for the partition function is

$$\begin{aligned} Z(N,P,T) &= \int_{-\infty}^{\infty} d\ln V \int_{0}^{1} d\mathbf{s}^N \int_{4\pi} d\mathbf{u}^N \cdot \\ & \exp\{-[U(\{\mathbf{s}_i\},\mathbf{H},\{\mathbf{u}_i\}) + PV]/k_{\mathrm{B}}T + (N+3)\ln V\} \end{aligned} \tag{A.4}$$

and we remark that we did not acquire additional factors of V; but none of them disappeared.

Beyond the scope of this work is the treatment beginning with even more general box shapes, e.g. twisted ones. What must we integrate out to reduce an arbitrary shape to a parallelepiped? We wonder whether more factors of volume have been overlooked.

Bibliography

[1] D. Frenkel and B. Mulder. The hard ellipsoid-of-revolution fluid i. monte carlo simulations. *Mol. Phys.*, 100:201, 2002.

[2] A. Donev, F. H. Stillinger, P. M. Chaikin, and S. Torquato. Unusually dense crystal packings of ellipsoids. *Phys. Rev. Lett.*, 92:255506, 2004.

[3] M. Letz, R. Schilling, and A. Latz. Ideal glass transition for hard ellipsoids. *Phys. Rev. E*, 62:5173, 2000.

[4] R. A. Smith. *The life and works of Thomas Graham*. Glasgow, 1884.

[5] P. N. Pusey and W. van Megen. Phase-behavior of concentrated suspensions of nearly hard colloidal spheres. *Nature*, 320:340–342, 1986.

[6] B. J. Alder and T. E. Wainwright. Phase transition for a hard sphere system. *J. Chem. Phys*, 27:1208, 1957.

[7] L. Onsager. *Ann. N. Y. Acad. Sci.*, 51:627, 1949.

[8] C. M. Care and D. J. Cleaver. Computer simulation of liquid crystals. *Reports On Progress In Phys.*, 68:2665–2700, 2005.

[9] M. R. Wilson. Progress in computer simulations of liquid crystals. *Int. Rev. In Phys. Chem.*, 24:421–455, 2005.

[10] J. Vieillard-Baron. *J. Chem. Phys.*, 56:4729, 1972.

[11] J. W. Perram, M. S. Wertheim, J. L. Lebowitz, and G. O. Williams. *Chem. Phys. Lett.*, 105:277, 1984.

[12] J. W. Perram and M. S. Wertheim. *J. Comput. Phys.*, 58:409, 1985.

[13] D. Frenkel and B. Mulder. The hard ellipsoid-of-revolution fluid i. monte carlo simulations. *Mol. Phys.*, 55:1171, 1985.

[14] P. G. de Gennes and J. Prost. *The Physics of Liquid Crystals*. Clarendon Press, Oxford, 1993.

[15] G. J. Zarragoicoechea, D. Levesque, and J. J. Weis. *Mol. Phys.*, 75:989, 1992.

[16] M. P. Allen and C. P. Mason. Stability of the nematic phase for the hard ellipsoid fluid. *Mol. Phys.*, 86:467, 1995.

[17] P. J. Camp, C. P. Mason, M. P. Allen, A. A. Khare, and D. A. Kofke. *J. Chem. Phys.*, 105:2837, 1996.

[18] M. P. Allen. *Liq. Cryst.*, 8:499, 1990.

[19] P. J. Camp and M. P. Allen. Phase diagram of the hard biaxial ellipsoid fluid. *J. Chem. Phys.*, 106:6681, 1997.

[20] M. P. Allen. In N. Attig, K. Binder, H. Grubmüller, and K. Kremer, editors, *Computational Soft Matter: From Synthetic Polymers to Proteins, NIC Series*, volume 23, chapter Liquid Crystal Systems, pages 289–320. NIC Directors, Jülich, 2004.

[21] A. Donev, I. Cisse, D. Sachs, E. Variano, F. H. Stillinger, R. Connelly, S. Torquato, and P. M. Chaikin. Improving the density of jammed disordered packings using ellipsoids. *Science*, 303:990–993, 2004.

[22] M. P. Allen and D. Frenkel. Observation of dynamical precursors of the isotropic-nematic transition by computer simulation. *Phys. Rev. Lett.*, 58: 1748, 1987.

[23] M. P. Allen, D. Frenkel, and J. Talbot. *Comput. Phys. Rep.*, 9:301, 1989.

[24] M. P. Allen. Diffusion-coefficient increases with density in hard ellipsoid liquid-crystals. *Phys. Rev. Lett.*, 65:2881–2884, 1990.

[25] P. Bereolos, J. Talbot, M. P. Allen, and G. T. Evans. Transport-properties of the hard ellipsoid fluid. *J. Chem. Phys.*, 99:6087–6097, 1993.

[26] R. Schilling and T. Scheidsteger. Mode coupling approach to the ideal glass transition of molecular liquids: Linear molecules. *Phys. Rev. E*, 56:2932, 1997.

[27] T. Franosch, M. Fuchs, W. Götze, M. R. Mayr, and A. P. Singh. Theory for the reorientational dynamics in glass-forming liquids. *Phys. Rev. E*, 56: 5659–5674, 1997.

[28] R. Schilling. Mode-coupling theory for translational and orientational dynamics near the ideal glass transition. *J. Phys.: Condens. Matter*, 12:6311, 2000.

[29] W. Götze. In J. P. Hansen, D. Levesque, and J. Zinn-Justin, editors, *Liquids, Freezing, and the Glass Transition*. North-Holland, Amsterdam, 1991.

[30] C. de Michele, R. Schilling, and F. Sciortino. Dynamics of uniaxial hard ellipsoids. *Phys. Rev. Lett.*, 98:265702, 2007.

[31] K. M. Keville, E. I. Franses, and J. M. Caruthers. *J. Colloid Interface Sci.*, 144:103, 1991.

[32] C. C. Ho, A. Keller, J. A. Odell, and R. H. Ottewill. *Colloid. Polym. Sci.*, 271:469, 1993.

[33] J. C. Loudet, A. G. Yodh, and B. Pouligny. *Phys. Rev. Lett.*, 97:018304, 2006.

[34] H. Lehle, E. Noruzifar, and M. Oettel. Ellipsoidal particles at fluid interfaces. *European Phys. J. E*, 26:151–160, 2008.

[35] M. G. Basavaraj, G. G. Fuller, J. Fransaer, and J. Vermant. *Langmuir*, 22: 6605, 2006.

[36] A. Mohraz and M. J. Solomon. *Langmuir*, 21:5298, 2005.

[37] D. Mukhija and M. J. Solomon. Translational and rotational dynamics of colloidal rods by direct visualization with confocal microscopy. *J. Colloid Interface Science*, 314:98–106, 2007.

[38] W. Kob. Supercooled liquids, the glass transition, and computer simulations. In J. P. Hansen, D. Levesque, and J. Zinn-Justin, editors, *Lecture Notes for “Slow relaxations and nonequilibrium dynamics in condensed matter”, Les Houches July, 1-25, 2002; Les Houches Session LXXVII*, pages 199–270. Springer, Berlin, 2003.

[39] U. Bengtzelius, W. Götze, and A. Sjölander. *J. Phys. C*, 17:5915, 1984.

[40] W. Kob. The Mode–Coupling Theory of the Glass Transition. In J. Fourkas, D. Kivelson, U. Mohanty, and K. Nelson, editors, *Experimental and Theoretical Approaches to Supercooled Liquids: Advances and Novel Applications*. ACS Books, Washington, 1997.

[41] S. Yip, editor. Theme Issue on Relaxation Kinetics in Supercooled Liquids–Mode Coupling Theory and its Experimental Tests. *Transport Theory and Statistical Physics*, 24(6–8), 1995.

[42] R. Schilling. Theories of the Structural Glass Transition. In G. Radons, W. Just, and P. Häussler, editors, *Collective Dynamics of Nonlinear and Disordered Systems*. Springer, Berlin, 2003.

[43] W. Götze and L. Sjögren. Relaxation processes in supercooled liquids. *Rep. Prog. Phys.*, 55:241, 1992.

[44] W. Götze. Liquids, Freezing and the Glass Transition. Les Houches – Session LI, 1989.

[45] L. Sjögren. Kinetic theory of current fluctuations in simple classical liquids. *Phys. Rev. A*, 22:2866, 1980.

[46] R. Schilling. In R. Richert and A. Blumen, editors, *Disorder Effects on Relaxational Processes*, page 193. Springer, Berlin, 1994.

[47] H. Z. Cummins, G. Li, W. M. Du, and J. Hernandez. Relaxational dynamics in supercooled liquids: experimental tests of the mode coupling theory. *Physica A*, 204:169, 1994.

[48] T. Gleim and W. Kob. The beta-relaxation dynamics of a simple liquid. *European Phys. J. B*, 13:83–86, 2000.

[49] G. Li, W. M. Du, X. K. Chen, H. Z. Cummins, and N. J. Tao. *Phys. Rev. A*, 45:3867, 1992.

[50] W. van Megen and S. M. Underwood. *Phys. Rev. E*, 49:4206, 1994.

[51] W. Kob and H. C. Andersen. Testing mode-coupling theory for a supercooled binary lennard-jones mixture - the van hove correlation-function. *Phys. Rev. E*, 51:4626–4641, 1995.

[52] W. Kob and H. C. Andersen. Testing mode-coupling theory for a supercooled binary lennard-jones mixture .2. intermediate scattering function and dynamic susceptibility. *Phys. Rev. E*, 52:4134–4153, 1995.

[53] S. Kämmerer, W. Kob, and R. Schilling. Test of mode coupling theory for a supercooled liquid of diatomic molecules. i. translational degrees of freedom. *Phys. Rev. E*, 58:2131, 1998.

[54] S. Kämmerer, W. Kob, and R. Schilling. Test of mode coupling theory for a supercooled liquid of diatomic molecules. ii. q-dependent orientational correlators. *Phys. Rev. E*, 58:2141, 1998.

[55] J. Horbach and W. Kob. Relaxation dynamics of a viscous silica melt: The intermediate scattering functions. *Phys. Rev. E*, 64:041503, 2001.

[56] Th. Voigtmann, A. M. Puertas, and M. Fuchs. Tagged-particle dynamics in a hard-sphere system: Mode-coupling theory analysis. *Phys. Rev. E*, 70: 061506, 2004.

[57] D. Frenkel and B. Smit. *Understanding Molecular Simulation*. Academic Press, San Diego, 2002.

[58] N. Metropolis, A. W. Rosenbluth, M. N. Rosenbluth, A. N. Teller, and E. Teller. Equation of state calculations by fast computing machines. *J. Chem. Phys.*, 21:1087–1092, 1953.

[59] D. P. Landau and K. Binder. *A Guide to Monte Carlo Simulations in Statistical Physics*. Cambridge University Press, Cambridge, 2000.

[60] R. Najafabadi and S. Yip. Observation of finite temeprature bain transformation in monte carlo simulation of iron. *Scripta Metallurgica*, 17:1199, 1983.

[61] S. Yashonath and C. N. R. Rao. A monte carlo study of crystal structure transformations. *Mol. Phys.*, 54:245, 1985.

[62] M. Parrinello and A. Rahman. *J. Appl. Phys.*, 52:7182, 1981.

[63] M. A. Miller, L. M. Amon, and W. P. Reinhardt. Should one adjust the maximum step size in a Metropolis Monte Carlo simulation? *Chem. Phys. Lett.*, 331:278–284, 2000.

[64] R. W. Hockney and J.W. Eastwood. *Computer Simulations Using Particles*. McGraw-Hill, New York, 1981.

[65] M. P. Allen and D. J. Tildesley. *Computer Simulation of Liquids*. Oxford University Press, Oxford, England, 1989.

[66] William H. Press, Saul A. Teukolsky, William Vetterling, and Brian P. Flannery. *Numerical Recipes: The Art of Scientific Computing*. Cambridge University Press, Cambridge, 3rd edition, 2007.

[67] A. D. Mighell, A. Santoro, and J. D. H. Donnay. In *International Tables for X-Ray Crystallography*, volume I, pages 530–535. Kynoch Press, Birmingham, 3rd edition, 1969.

[68] A. D. Mighell. Lattice symmetry and identification - The fundamental role of reduced cells in materials characterization. *J. Research National Institute Standards Technology*, 106:983–995, 2001.

[69] A. D. Mighell. Conventional cells - The last step toward general acceptance of standard conventional cells for the reporting of crystallographic data. *J. Research National Institute Standards Technology*, 107:373–377, 2002.

[70] M. Radu, P. Pfleiderer, and T. Schilling. In preparation.

[71] M. Radu. *MC-Simulationen zur Berechnung der Freien Energie von Kristallphasen in Suspensionen von harten Ellipsoiden*. Diploma Thesis, Johannes Gutenberg–Universität Mainz, 2008.

[72] W. G. Hoover and F. H. Ree. *J. Chem. Phys.*, 49:3609, 1968.

[73] W. W. Wood. *J. Chem. Phys.*, 48:415, 1968.

[74] I. R. McDonald. *Mol. Phys.*, 23:41, 1972.

[75] L. Berthier and W. Kob. The Monte Carlo dynamics of a binary Lennard-Jones glass-forming mixture. *J. Phys.-Condes. Matter*, 19, 2007.

[76] P. R. ten Wolde, M. J. Ruiz-Montero, and D. Frenkel. Numerical calculation of the rate of crystal nucleation in a lennard-jones system at moderate undercooling. *Phys. Rev. Lett.*, 75:2714, 1995.

[77] Th. Theenhaus, M. P. Allen, M. Letz, A. Latz, and R. Schilling. Dynamical precursor of nematic order in a dense fluid of hard ellipsoids of revolution. *Eur. Phys. J. E*, 8:269, 2002.

[78] C. Renner, H. Löwen, and J. L. Barrat. Orientational glass transition in a rotator model. *Phys. Rev. E*, 52:5091, 1995.

[79] S. Kämmerer, W. Kob, and R. Schilling. Dynamics of the rotational degrees of freedom in a supercooled liquid of diatomic molecules. *Phys. Rev. E*, 56:5450, 1997.

[80] A. J. Moreno, S.-H. Chong, W. Kob, and F. Sciortino. Dynamic arrest in a liquid of symmetric dumbbells: Reorientational hopping for small molecular elongations. *J. Chem. Phys.*, 123:204505, 2005.

[81] T. Gleim, W. Kob, and K. Binder. How does the relaxation of a supercooled liquid depend on its microscopic dynamics? *Phys. Rev. Lett.*, 81:4404, 1998.

[82] F. A. Lindemann. *Phys. Z.*, 11:609, 1910.

[83] M. Fuchs, I. Hofacker, and A. Latz. Primary relaxation in a hard-sphere system. *Phys. Rev. A*, 45:898, 1992.

[84] S. Kämmerer. PhD thesis, Johannes Gutenberg–Universität Mainz, 1997.

[85] M. Nauroth and W. Kob. Quantitative test of the mode-coupling theory of the ideal glass transition for a binary Lennard-Jones system. *Phys. Rev. E*, 55:657–667, 1997.

[86] I. Chang and H. Sillescu. Heterogeneity at the glass transition: Translational and rotational self-diffusion. *J. Phys. Chem. B*, 101:8794–8801, 1997.

[87] L. Berthier. Time and length scales in supercooled liquids. *Phys. Rev. E*, 69, 2004.

[88] P. Chaudhuri, L. Berthier, and W. Kob. Universal nature of particle displacements close to glass and jamming transitions. *Phys. Rev. Lett.*, 99:060604, 2007.

[89] P. Harrowell. Visualizing the collective motions responsible for the alpha and beta relaxations in a model glass. *Phys. Rev. E*, 48:4359–4363, 1993.

[90] M. D. Ediger. Spatially heterogeneous dynamics in supercooled liquids. *Ann. Rev. Phys. Chem.*, 51:99–128, 2000.

[91] A. Rahman. Correlations in the motion of atoms in liquid argon. *Phys. Rev.*, 136:A 405, 1964.

[92] E. R. Weeks, J. C. Crocker, A.C. Levitt, A. Schofield, and D. A. Weitz. *Science*, 287:627, 2000.

[93] G. Marty and O. Dauchot. *Phys. Rev. Lett.*, 94:015701, 2005.

[94] P. I. Hurtado, L. Berthier, and W. Kob. Heterogeneous diffusion in a reversible gel. *Phys. Rev. Lett.*, 98, 2007.

[95] D. A. Stariolo and G. Fabricius. Fickian crossover and length scales from two point functions in supercooled liquids. *J. Chem. Phys.*, 125, 2006.

[96] L. J. Kaufman and D. A. Weitz. Direct imaging of repulsive and attractive colloidal glasses. *J. Chem. Phys.*, 125, 2006.

[97] P. Bursac, G. Lenormand, B. Fabry, M. Oliver, D. A. Weitz, V. Viasnoff, J. P. Butler, and J. J. Fredberg. Cytoskeletal remodelling and slow dynamics in the living cell. *Nature Materials*, 4:557–561, 2005.

[98] W. Kob and H. C. Andersen. Scaling behavior in the dynamics of a supercooled lennard-jones mixture. *Nuovo Cimento Della Societa Italiana Di Fisica D-condensed Matter Atomic Mol. Chem. Phys. Fluids Plasmas Biophys.*, 16:1291–1295, 1994.

[99] L. Van Hove. Correlations in space and time and born approximation scattering in systems of interacting particles. *Phys. Rev.*, 95:249–262, 1954.

PHYSICAL REVIEW E **75**, 020402(R) (2007)

Simple monoclinic crystal phase in suspensions of hard ellipsoids

P. Pfleiderer* and T. Schilling
Institut für Physik, Johannes Gutenberg-Universität, Staudinger Weg 7, D-55099 Mainz, Germany

(Received 6 December 2006; revised manuscript received 12 January 2007; published 9 February 2007)

We present a computer simulation study on the crystalline phases of hard ellipsoids of revolution. For aspect ratios $\geqslant 3$ the previously suggested stretched-fcc phase [Frenkel and Mulder, Mol. Phys. **55**, 1171 (1985)] is replaced by a different crystalline phase. Its unit cell contains two ellipsoids with unequal orientations. The lattice is simple monoclinic. The angle of inclination of the lattice, β, is a very soft degree of freedom, while the two right angles are stiff. For one particular value of β, the close-packed version of this crystal is a specimen of the family of superdense packings recently reported [Donev *et al.*, Phys. Rev. Lett. **92**, 255506 (2004)]. These results are relevant for studies of nucleation and glassy dynamics of colloidal suspensions of ellipsoids.

DOI: 10.1103/PhysRevE.75.020402 PACS number(s): 82.70.Dd, 64.60.Cn, 61.50.Ah, 82.20.Wt

Classical, hard particles such as nonoverlapping spheres, rods, or ellipsoids are widely used as models for granular matter, colloidal and molecular fluids, crystals, and glasses. Their success—and their appeal—lies in the fact that the problem of evaluating a many-body partition function is reduced to a slightly simpler, geometrical problem, namely, the evaluation of entropic contributions only. This is an advantage, in particular, for computer simulations. Hence one of the first applications of computer simulations was a study of the liquid-solid phase transition in hard spheres [1].

In this Rapid Communication, we reexamine the high-density phase behavior of hard ellipsoids of revolution with short aspect ratios. This system has been studied in Monte Carlo simulations by Frenkel and Mulder in 1985 [2]. Since then, the focus of attention has been on the nematic phase and the isotropic-nematic transition [3–5]. Biaxial hard ellipsoids have also been studied [6,7]. But, to our knowledge, the high-density phases have not been investigated further. Knowledge of these phases is relevant for studies of elongated colloids in general, and it is crucial for the study of nucleation [8] and glassy dynamics [9] in hard ellipsoids.

At high densities, Frenkel and Mulder assumed that the most stable phase was an orientationally ordered solid which can be constructed in the following way. A face-centered cubic (fcc) system of spheres is stretched by a factor x in an arbitrary direction $\mathbf{n}$. This transformation results in a crystal structure of ellipsoids of aspect ratio x, which are oriented along $\mathbf{n}$. As the transformation is linear, the density of closest packing is the same as for the closest packing of spheres $\phi = \pi/\sqrt{18} \approx 0.7405$. Recently, Donev and co-workers showed that ellipsoids can be packed more efficiently if non-lattice-periodic packings (i.e. packings in which a unit cell contains several ellipsoids at different orientations) are taken into account [10]. For unit cells containing two particles, they constructed a family of packings which reach a density of $\phi = 0.770\,732$ for aspect ratios larger than $\sqrt{3}$.

We have performed Monte Carlo simulations of hard ellipsoids of revolution with aspect ratios $a/b = \frac{1}{3}, 2, 3, 4, 6$ and found that, for large parts of the high-density phase diagram, the lattice crystal suggested by Frenkel and Mulder is unstable with respect to a different crystalline phase. Its unit cell is simple monoclinic and contains two ellipsoids at an angle with respect to each other. We will refer to this phase as SM2 (simple monoclinic with a basis of two ellipsoids).

Simulations were performed at constant particle number N, pressure P, and temperature T. The shape of the periodic box was allowed to fluctuate, so that the crystal unit cell could find its equilibrium shape. This was achieved by implementing the Monte Carlo (MC) equivalent of the simulation method by Parrinello and Rahman [11–13]. We constructed the initial solid structures by stretching a fcc hard sphere crystal along the [111] direction by a factor of a/b. Hence the simulations were started with crystals identical to the ones studied by Frenkel and Mulder. For aspect ratios $a/b = \frac{1}{3}, 2, 3$, we simulated eight independent systems, each containing $N \approx 1700$ particles. Simulations started at $P = 50\, k_B T/8ab^2$. The pressure was lowered in subsequent runs until we observed melting to the nematic phase. In each run, equilibration lasted roughly 2×10^6 MC sweeps, and was followed by $(1.8-3.2) \times 10^6$ MC sweeps for calculating thermodynamic averages. (One MC sweep consisted of N attempts to move or rotate a particle and one attempt to change the box shape, on average.) For aspect ratio $a/b = 6$, we simulated eight independent systems with $N = 3072$ at a pressure $P = 46\, k_B T/8ab^2$. Equilibration and data acquisition summed up to more than 3×10^6 MC sweeps. One system with $a/b = 4$, $N = 1200$, and $P = 46\, k_B T/8ab^2$ was first simulated by sampling only rectangular box shapes for a total of 2.2×10^6 MC sweeps, and was then simulated including non-rectangular box shapes at the same and lower pressures for several million MC sweeps.

Particle overlap was checked by a routine [14] that uses the Vieillard-Baron [15] and Perram-Wertheim [16,17] criteria. In a simulation of a system with $a/b = 3$ and $N = 1728$, 1×10^6 MC sweeps took about 12 h of CPU time on a 1.8GHz processor.

All systems with aspect ratios $a/b \geqslant 3$ left the initial fcc structure in favor of a simple monoclinic lattice with a basis of two ellipsoids (SM2). We will discuss this structure for $a/b = 3$ and return to different aspect ratios toward the end of this Rapid Communication.

---

*Electronic address: pfleider@uni-mainz.de

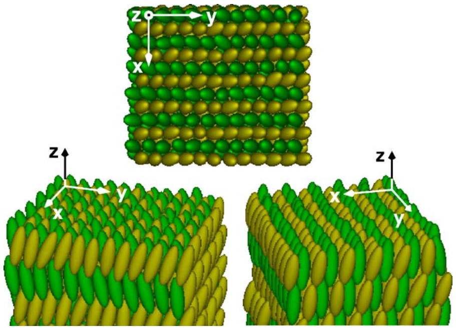

FIG. 1. (Color online) Snapshot of the SM2 crystal from different angles, with $a/b=3$, $N=1728$, and $P=46\ k_BT/8ab^2$. Color code (grayscale) indicates orientation.

Figure 1 shows a snapshot of a system in the SM2 phase with $a/b=3$. The color code (grayscale) helps distinguish the two directions of orientation which are present in the crystal. In the initial configuration, a stretched-fcc crystal, all ellipsoids were oriented along the z axis. The SM2 phase is mainly the result of a collective reorientation. The two directions of orientation alternate from layer to layer. Layers containing ellipsoids of only one orientation are here parallel to the y axis and form an angle with the x axis. Within layers parallel to the xy plane, the centers of mass of the ellipsoids form a nearly triangular lattice. It differs from the initial fcc crystal by a slight elongation along the x axis. However, the collective reorientation of the ellipsoids displaced their *tips* in such a way that they now form a rectangular lattice. This can be discerned in the top view in Fig. 1. The tips of the neighboring layers interlace. As a result, each ellipsoid now has four nearest neighbors above and below, whereas in the fcc structure, it had three. The total number of nearest neighbors has increased from 12 to 14, which is indicative of a higher packing efficiency.

The initial triangular symmetry about the z axis allows for two additional, equivalent SM2 configurations, which are rotated with respect to the one in Fig. 1 by ±60°. We observed these possibilities as well; in fact, only two out of our eight systems assumed the global orientation seen in Fig. 1.

The unit cell of the SM2 structure is shown in Fig. 2. The open circles indicate the centers of the two ellipsoids which form the basis. The cell is monoclinic. The yellow (light gray) ellipsoid is at the origin, the green (dark gray) one is at $\frac{1}{2}(\mathbf{a}+\mathbf{b})$. The orientations are symmetric about the ac plane. The parameters used to produce Figs. 2(a) and 2(b) are thermal average values obtained from simulations with $N=1728$ and $P=46\ k_BT/8ab^2$; cf. Fig. 1. The cell remained monoclinic even when the pressure was lowered down to the melting transition into the nematic phase.

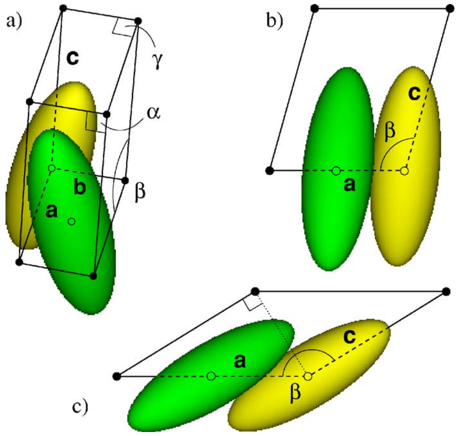

FIG. 2. (Color online) Unit cell of SM2 with $a/b=3$. The open circles indicate the centers of the two ellipsoids which form the basis. The cell is monoclinic. β exhibits large variations. The yellow (light gray) ellipsoid is at the origin; the green (dark gray) one is at $(1/2)(\mathbf{a}+\mathbf{b})$. The orientations are symmetric about the ac plane. The parameters in (a) and (b) are average values for $N=1728$ and $P=46\ k_BT/8ab^2$; cf. Fig. 1. (c) shows the cell at close packing with $\beta=148.3°$, where it is an instance of the family of packings introduced by Donev *et al.* [10].

The angle of inclination, β, relaxes extremely slowly. The simulations with $N=1728$ were too slow to equilibrate this angle. Therefore we carried out a set of very long simulations for a smaller system ($N=432$) with initial values of β in the range $105° < \beta < 150°$. After more than 100×10^6 Monte Carlo sweeps, there was still no clear evidence for a preferred value of β. Variations of 15° in a single simulation were typical, even at $P=46\ k_BT/8ab^2$. Hence, we expect the shear modulus in this degree of freedom to be very small. The other two angles α and γ were stable at 90°, with fluctuations of less than 1°. The associated shear moduli are much larger. The reason for this interesting rheological property is that planes of uniform orientation slide well past each other in the $\mathbf{c}$ direction only. In some of the long simulations, this led to undulations of the lattice in the $\mathbf{c}$ direction to the point of planar defects, which would spontaneously heal again.

To find a lower bound for the maximum density of the SM2 phase ($a/b=3$), we performed simulations sampling only the unit cell parameters and particle orientations, and imposing all symmetries of SM2. The initial parameters were average values obtained from the simulations with $N=1728$ and $P=46\ k_BT/8ab^2$. In the process of maximizing the density, β increased from 105° to about 150°, and the common tilt of the ellipsoids with respect to the bc plane disappeared. We then imposed that $(\mathbf{a}+\mathbf{c})$ be perpendicular to $\mathbf{c}$ [see Fig. 2(c)], which is equivalent to $\beta\approx 148°$. Under this condition the SM2 structure becomes an instance of the family of packings introduced by Donev *et al.* [10]. This simulation achieved the highest packing fraction, namely, $\phi \approx 0.770\,732$ (the value reported by Donev *et al.*).

But already at $\beta\approx 105°$ we found a jamming density of 99.663% of the maximum. Simulations at intermediate values indicate a smooth approach toward the maximum density as β increases. Thus, the close-packing density varies very weakly for $105° < \beta < 148°$. While this range is traversed, ellipsoids of one orientation move past neighbors of the other orientation by almost half their length. This can be seen in Figs. 2(b) and 2(c). For reasons of symmetry, this translation may even continue by the same amount while the density remains above 99.663% of the maximum. These observations are in accord with the fact that β is soft at finite pressures; evidently, the free volume distribution possesses a similarly slight variation with β.

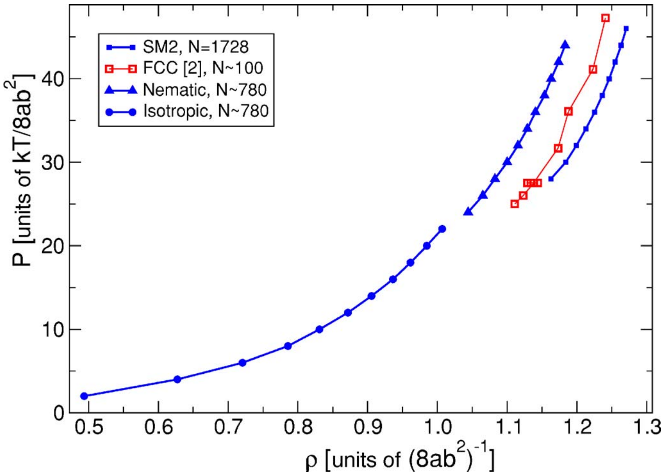

FIG. 3. (Color online) Equation of state data for $a/b=3$ and $N=1728$. The open squares show stretched-fcc data by Frenkel and Mulder [2], the filled squares the higher-density SM2 phase. Also shown are the nematic and fluid branches (triangles and circles, respectively). Errors on our data are indicated by the size of the symbols. The SM2 curve tends to underestimate the density slightly since β was not equilibrated entirely.

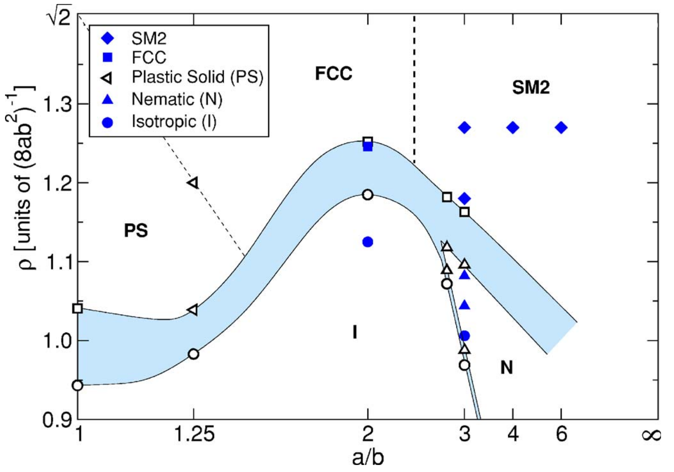

FIG. 4. (Color online) Phase diagram of hard, uniaxial ellipsoids, showing the results of Frenkel and Mulder (open symbols) [2], and their suggested phase boundaries and coexistence regions. The data points at $a/b=1$ are taken from [18]. We have inserted our state points (filled symbols) and a vertical dashed line to delimit the region in which we found the SM2 phase; but our data are insufficient to locate a phase boundary.

Figure 3 shows equation of state data of the SM2 phase from our simulations with $N=1728$ particles. The density of the SM2 is higher than that of the stretched-fcc structure for all pressures. Five of eight systems underwent the transition to the SM2 structure already at the highest simulated pressure $P=48\ k_BT/8ab^2$, the remaining three at $P=46\ k_BT/8ab^2$. Note also that in all our runs the SM2 phase melted to the nematic phase without revisiting the stretched-fcc phase from which it developed; evidently, the SM2 not only packs more efficiently than the stretched-fcc phase, it also provides for a better distribution of free volume at all densities until the transition to the nematic phase. Hence it is more stable than the stretched-fcc structure. We also show the nematic branch from an (N,P,T) compression (i.e. the pressure was raised between successive simulations) with $N\approx 780$ particles and up to 6×10^6 MC sweeps per run. Even at strong overcompression, no spontaneous crystallization occurred. This indicates that the nucleation barrier to the SM2 phase is very high. Also shown is the isotropic fluid branch as obtained from (N,P,T) compression and expansion runs with $N\approx 780$.

All eight simulations at $a/b=6$ and $P=46\ k_BT/8ab^2$ formed the SM2 phase as well, although four of them retained a planar defect. Different regions in the periodic box were able to develop different global orientations of SM2 as the systems were larger ($N=3072$) than those with $a/b=3$ ($N=1728$). We also simulated a system with $a/b=4$, $N=1200$, and $P=46\ k_BT/8ab^2$; it formed the SM2 phase as well. It also developed a planar defect, this time owing to a geometrical mismatch between the simulation box and the SM2 unit cell. Note that for $a/b=3$ and 4, the SM2 phase formed even in simulations sampling only rectangular box shapes. It is therefore more stable than the stretched-fcc phase even when it cannot assume its equilibrium shape.

By contrast, ellipsoids with $a/b=2$ and the oblate $a/b=\frac{1}{3}$ showed no tendency to leave the initial stretched-fcc structure. We studied each of these systems with eight independent simulations. In none of them did two preferred directions of ellipsoid orientation develop. All of them melted to the nematic phase on expansion, directly from the stretched-fcc structure. But note that the apparent stability of fcc in our simulations may well be due to a free energy barrier, rather than indicating genuine stability.

In Fig. 4 we show a phase diagram of hard ellipsoids of revolution. It includes part of the results of Frenkel and Mulder, and their suggested phase boundaries and coexistence regions. We have inserted our state points and a vertical dashed line to delimit the region in which we found the SM2 phase; but our data are insufficient to locate a phase boundary.

In the high-density phase diagram of hard ellipsoids of revolution we have found a crystal that is more stable than the stretched-fcc structure proposed by Frenkel and Mulder [2]. This phase, SM2, has a simple monoclinic unit cell containing a basis of two ellipsoids. The angle of inclination, β, is a very soft degree of freedom, whereas the other angles are not. At one value of β ($\approx 148.3°$ for $a/b=3$), the close-packed SM2 structure is an instance of the family of packings introduced by Donev *et al.* [10]. As for thermodynamic stability, our results unequivocally remove the stretched-fcc structure for aspect ratio $a/b=3$ from the phase diagram of hard, uniaxial ellipsoids. Our state points for $a/b=4$ and 6 suggest that this holds for the entire range of $3\leqslant a/b\leqslant 6$, and possibly beyond. However, this does not prove that SM2 is the ground state. A procedure has been developed for making almost monodisperse ellipsoids [19,20], which are of colloidal size. Their behavior at water-air interfaces has been studied [21,22]; also three-dimensional structural properties of a sedimentation of these particles have been successfully characterized [23]. It would be interesting to perform experiments probing colloidal crystals of ellipsoids.

This work was supported by the Emmy Noether Program and SFB TR6 of the Deutsche Forschungsgemeinschaft (DFG), and the European Network of Excellence SoftComp. We are grateful to the NIC Jülich for computing time, and to K. Binder, D. Frenkel, M. P. Allen, J. Vermant, A. Donev, and W. A. Siebel for helpful suggestions.

[1] B. J. Alder and T. E. Wainwright, J. Chem. Phys. **27**, 1208 (1957).
[2] D. Frenkel and B. Mulder, Mol. Phys. **55**, 1171 (1985).
[3] G. J. Zarragoicoechea, D. Levesque, and J. J. Weis, Mol. Phys. **75**, 989 (1992).
[4] M. P. Allen and C. P. Mason, Mol. Phys. **86**, 467 (1995).
[5] P. J. Camp, C. P. Mason, M. P. Allen, A. A. Khare, and D. A. Kofke, J. Chem. Phys. **105**, 2837 (1996).
[6] M. P. Allen, Liq. Cryst. **8**, 499 (1990).
[7] P. J. Camp and M. P. Allen, J. Chem. Phys. **106**, 6681 (1997).
[8] T. Schilling and D. Frenkel, Comput. Phys. Commun. **169**, 117 (2005).
[9] M. Letz, R. Schilling, and A. Latz, Phys. Rev. E **62**, 5173 (2000).
[10] A. Donev, F. H. Stillinger, P. M. Chaikin, and S. Torquato, Phys. Rev. Lett. **92**, 255506 (2004).
[11] M. Parrinello and A. Rahman, J. Appl. Phys. **52**, 7182 (1981).
[12] R. Najafabadi and S. Yip, Scr. Metall. **17**, 1199 (1983).
[13] S. Yashonath and C. N. R. Rao, Mol. Phys. **54**, 245 (1985).
[14] M. P. Allen, D. Frenkel, and J. Talbot, Comput. Phys. Rep. **9**, 301 (1989).
[15] J. Vieillard-Baron, J. Chem. Phys. **56**, 4729 (1972).
[16] J. W. Perram, M. S. Wertheim, J. L. Lebowitz, and G. O. Williams, Chem. Phys. Lett. **105**, 277 (1984).
[17] J. W. Perram and M. S. Wertheim, J. Comput. Phys. **58**, 409 (1985).
[18] W. G. Hoover and F. H. Ree, J. Chem. Phys. **49**, 3609 (1968).
[19] K. M. Keville, E. I. Franses, and J. M. Caruthers, J. Colloid Interface Sci. **144**, 103 (1991).
[20] C. C. Ho, A. Keller, J. A. Odell, and R. H. Ottewill, Colloid Polym. Sci. **271**, 469 (1993).
[21] M. G. Basavaraj, G. G. Fuller, J. Fransaer, and J. Vermant, Langmuir **22**, 6605 (2006).
[22] J. C. Loudet, A. G. Yodh, and B. Pouligny, Phys. Rev. Lett. **97**, 018304 (2006).
[23] A. Mohraz and M. J. Solomon, Langmuir **21**, 5298 (2005).

A Letters Journal Exploring
the Frontiers of Physics

October 2008

EPL, **84** (2008) 16003
doi: `10.1209/0295-5075/84/16003`

`www.epljournal.org`

Glassy dynamics in monodisperse hard ellipsoids

P. Pfleiderer[a], K. Milinkovic and T. Schilling

Institut für Physik, Johannes Gutenberg-Universität - Staudinger Weg 7, D-55099 Mainz, Germany, EU

received 1 August 2008; accepted 22 August 2008

PACS `64.70.pv` – Colloids
PACS `61.20.Ja` – Computer simulation of liquid structure
PACS `61.25.Em` – Molecular liquids

Abstract – We present evidence from computer simulations for glassy dynamics in suspensions of monodisperse hard ellipsoids. In equilibrium, almost spherical ellipsoids show a first-order transition from an isotropic phase to a rotator phase. When overcompressing the isotropic phase into the rotator regime, we observe super-Arrhenius slowing-down of diffusion and relaxation, accompanied by two-step relaxation in positional and orientational correlators. The effects are strong enough for asymptotic laws of mode-coupling theory to apply. Glassy dynamics are unusual in monodisperse systems. Typically, polydispersity in size, a mixture of particle species or network-forming covalent bonds are prerequisite to prevent crystallization. Here, we show that a slight particle anisometry acts as a sufficient source of disorder. This sheds new light on the question of which ingredients are required for glass formation.

Hard-particle models play a key role in statistical mechanics. They are conceptually and computationally simple, and they offer insight into systems in which particle shape is important, including atomic, molecular, colloidal, and granular systems. Ellipsoids are a classic model of non-spherical particles. We report here that this simple anisometry can hinder crystallization and facilitate glassy dynamics —a phenomenon which does usually not occur in monodisperse systems. Typically, polydispersity, additional particle species, or other sources of disorder, such as tetra-valency, are needed for the development of glass-like behavior (*i.e.* drastic slowing-down of the dynamics without a change in structure).

In recent years, there have been two studies closely related to our topic, which we briefly summarize here: Letz and coworkers [1] have applied idealized molecular mode-coupling theory (MMCT [2,3]) to the hard-ellipsoid fluid. In addition to conventional mode-coupling theory (MCT) [4], MMCT takes orientational degrees of freedom into account. For nearly spherical ellipsoids, they predicted a discontinuous glass transition in positional and orientational degrees of freedom. MMCT locates the transition inside the coexistence region between the isotropic fluid and the positionally ordered phases. In addition, a continuous transition was predicted upon further compression into the rotator regime. This transition affects only the odd-parity orientational correlators, *e.g.* 180° flips.

However, MCT cannot make statements about crystal nucleation. Hence, the MCT prediction of a glass transition is not sufficient to conclude that the transition will occur in a simulation or experiment. A prominent example is the overcompression of monodisperse hard spheres. Here, the nucleation barrier can be easily crossed, and crystallization always prevents glass formation.

De Michele *et al.* [5] have recently studied the dynamics of hard ellipsoids by molecular dynamics simulations. The states which they simulated were mostly located in the isotropic region. They computed isodiffusivity lines, which showed that the dynamics of the positional and orientational degrees of freedom were decoupled, since the positional isodiffusivity lines crossed the orientational ones at nearly 90°. This decoupling also appeared in correlation functions. The self-part of the intermediate scattering function displayed slight stretching only when overcompressing nearly spherical ellipsoids, while the second-order orientational correlator showed such stretching only for sufficiently elongated particles, *i.e.* near the isotropic-nematic transition. Clear indicators of glassy dynamics, however, would include a strong increase of relaxation times with volume fraction, even pointing towards dynamical arrest. Typically, correlators then develop a two-step decay, whose second step is affected by

---

[a] E-mail: `pfleider@uni-mainz.de`

this slowing-down. Such phenomena were not seen in [5] as overcompression was not significant.

We have performed Monte Carlo (MC) and molecular dynamics (MD) simulations for hard symmetrical ellipsoids of length-to-width ratios $l/w = 1.25$ (prolate) and $l/w = 0.8$ (oblate). We overcompressed these systems into the rotator regime (*i.e.* beyond volume fraction $\phi \approx 0.55$ [6]). We found two-step relaxation both in positional and even-parity orientational correlators. Positional and orientational relaxation slow down more strongly than an Arrhenius law. Odd-parity orientational correlators indicate that flipping is not affected. The observed glassy dynamics are strong enough to compare with MMCT. Also, we compare the MC and MD results.

The systems were equilibrated using MC at constant particle number N, pressure P and temperature T [7,8] in a cubic box with periodic boundaries. Each system contained more than 3000 particles. Random isotropic configurations were used as starting configurations. Towards the end of each run, a configuration with a volume fraction close to the average volume fraction was chosen and scaled to the average volume fraction exactly. The systems were considered equilibrated[1] when the volume fraction had settled and all positional and the orientational correlators were independent of absolute simulation time. For production, we used MC and MD. In the MC simulations (now at constant volume) the step sizes were fixed to small values, so that unphysical grazing moves were negligible. The particles then mimic Brownian motion, similar to colloidal ellipsoids suspended in a liquid. The step sizes were the same for all runs, hence a unique time scale could be established. The MD simulations implemented free flight and elastic collisions [9].

The systems had a slight tendency to crystallize to the rotator phase at high volume fractions. To monitor crystallinity, we computed the local positional order using the bond-orientational order parameter q_6 [10]. The fraction of particles which were part of crystalline clusters never exceeded 2.6% and was typically below 0.5%.

To demonstrate the slowing-down of the positional degrees of freedom, we consider the self-part of the intermediate scattering function, $F_\mathrm{s}(q,t) = \langle \exp[i\mathbf{q}\cdot\Delta\mathbf{r}(t)]\rangle$, where $\mathbf{q}$ is the wave vector, $\Delta\mathbf{r}(t)$ the displacement of an ellipsoid after time t, and the angle brackets denote average over particles and ensemble average. In isotropic systems, F_s is a function of the absolute value q only. Decay of $F_\mathrm{s}(q,t)$ indicates that structural relaxation has occured on the length scale set by q. In fig. 1 we show $F_\mathrm{s}(q,t)$ for all simulations. The wavelength q_max was chosen close to the first maximum of the static structure factor (prolate: $6.85/w$, oblate: $7.85/w$), *i.e.* it corresponds to the neighbor spacing. One can clearly see the development of a plateau with increasing volume fraction. This means that there are two distinct stages of relaxation, and the latter slows down dramatically upon increase of volume fraction (note the logarithmic time scale). This two-step decay is a typical phenomenon in glass formers [4]. It is interpreted in terms of particles being trapped in cages formed by their nearest neighbors. The initial decay corresponds to motion within the traps, and the final decay to escape. At high volume fractions, exceedingly cooperative rearrangements are required for escape, making such events rare. Indicators of caging have not been seen in hard ellipsoids before (unless the moment of inertia was strongly increased [11]).

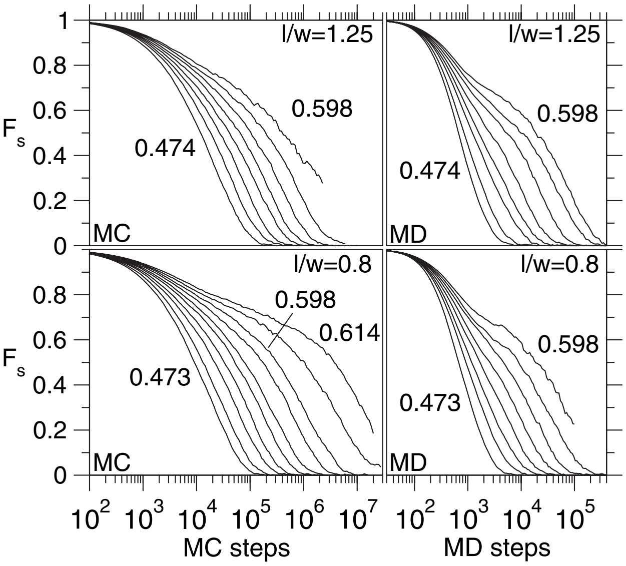

Fig. 1: Self-intermediate scattering functions at several volume fractions ϕ (prolate: 0.474, 0.511, 0.533, 0.551, 0.565, 0.578, 0.588, 0.598; oblate: 0.473, 0.504, 0.533, 0.550, 0.565, 0.578, 0.589, 0.598, 0.606, 0.614). At high volume fractions there is a plateau on intermediate time scales. The final relaxation is slowed down strongly with increasing volume fraction, indicative of glassy dynamics.

Dynamics in the orientational degrees of freedom is observed in terms of the second-order orientational correlator $L_2(t) = (1/2)\langle 3\cos^2\theta(t) - 1\rangle$, where $\theta(t)$ is the angle between the orientation at time t and the original orientation of an ellipsoid. Decay of this function indicates that relaxation of orientational degrees of freedom has taken place. Since $L_2(t)$ is an even function in $\cos\theta(t)$, the head-to-tail symmetry of the particles is taken into account. Figure 2 shows the orientational correlation functions. As in the intermediate scattering functions, plateaus develop at high volume fractions. Evidently, the cages hinder rotations of the ellipsoids. As a consequence, orientational and positional degrees of freedom are coupled. This is in contrast with the decoupling found at lower volume fractions [5].

The shape of both positional and orientational correlators differs between MC and MD on short time scales,

---

[1] For the case of overcompression, "equilibrated" here means within the metastable isotropic basin.

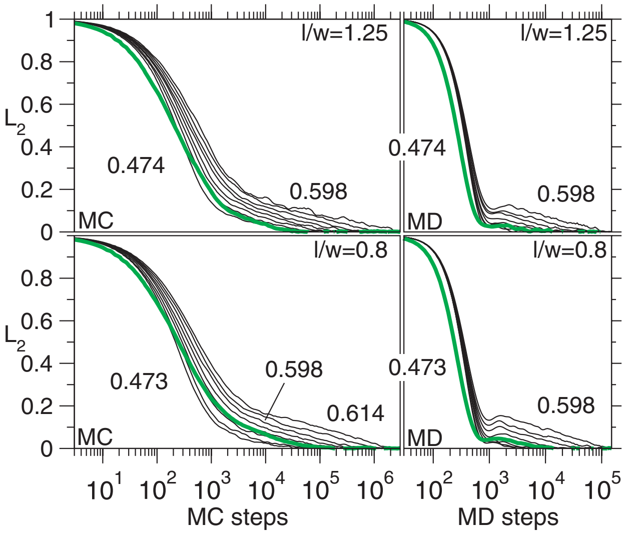

Fig. 2: (Color online) Second-order orientational correlators at several volume fractions ϕ as in fig. 1. Again a plateau develops with increasing ϕ. Hence, orientational degrees of freedom are coupled to the positional ones. Also shown are the third-order correlators at the highest density (bold green lines). They do not slow down, indicating that flipping modes are not affected.

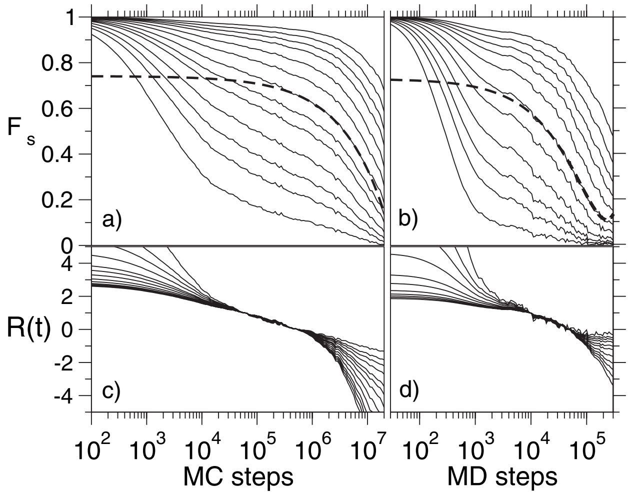

Fig. 3: Self-intermediate scattering functions $F_s(q,t)$ of a) the oblate system (MC data) and b) the prolate system (MD data) at the highest volume fraction, for the range $2.8 < qw < 20$. The dashed lines show fits to the von Schweidler law $F_s(q,t) = f_q - h_q^{(1)} t^b + h_q^{(2)} t^{2b}$ with $b = 0.65$. c) and d) show the same data transformed to $R(t) = [F_s(q,t) - F_s(q,t_1)]/[F_s(q,t_2) - F_s(q,t_1)]$. The collapse of the functions onto master curves demonstrates the factorization property.

reflecting the individual microscopic dynamics. On intermediate and long time scales, they do not differ significantly. Furthermore, when the correlators of the highest few volume fractions are rescaled by their decay time, their long time parts fall onto a master curve. These properties confirm predictions of MCT [12].

Unlike $L_2(t)$, the third-order orientational correlation function $L_3(t) = (1/2)\langle 5\cos^3\theta(t) - 3\cos\theta(t)\rangle$ does not show plateaus (bold green lines in fig. 2). Hence, while the overall reorientation slows down, flipping is barely hindered. This is in accord with the MMCT prediction of Letz *et al.* [1] and has also been found for the case of diatomic Lennard-Jones dumbbells [13], and symmetric Lennard-Jones dumbbells [14]. We note in passing that crystallization, if it occurs, releases the orientational degrees of freedom: The orientational correlators accelerate by three orders of magnitude and no longer have a plateau.

Next, we show that the slowing-down in our systems is strong enough to test MCT asymptotic laws. To this end, we first return to the intermediate scattering functions and focus on their q-dependence at high volume fractions. Figure 3 presents these functions for a) the oblate system (MC) and b) the prolate system (MD; in each case the other method shows similar results), with wavelengths in the range $2.8 < qw < 20$. We test two MCT predictions for the vicinity of the glass transition [4]. Firstly, for the late stages of the plateau and the early stages of the final decay, these functions should be well-fitted by the von Schweidler law (including the second-order correction), $F_s(q,t) = f_q - h_q^{(1)} t^b + h_q^{(2)} t^{2b}$, where f_q is the plateau height, $h_q^{(i)}$ are amplitudes, and b is a system-universal exponent (also independent of the microscopic dynamics). Agreement is excellent, as shown for two examples in fig. 3 (dashed lines). MC and MD data of both systems are consistent with $b = 0.65 \pm 0.2$. Secondly, where the $F_s(q,t)$ are near their plateaus, they should obey $F_s(q,t) = f_q + h_q G(t)$, where h_q is an amplitude, and $G(t)$ is a system-universal function. This relation entails the "factorization property", *i.e.* that $F_s(q,t)$ can be factorized into a q-dependent and a t-dependent part. To test this property for our systems, we transform $F_s(q,t)$ to $R(t) = [F_s(q,t) - F_s(q,t_1)]/[F_s(q,t_2) - F_s(q,t_1)]$, as done in [15], where t_1 and t_2 are times in the regime where the property holds. Since $R(t)$ is not a function of q, all correlators should fall onto a single master curve. Moreover, the curves should remain ordered, *i.e.* a curve which is above another on the left-hand side remains above the other on the right-hand side. Panels c) and d) of fig. 3 demonstrate the validity of the factorization property, and indeed they remain ordered.

We finally demonstrate the applicability of an MCT scaling law for the slowing-down, which even allows us to extract the MCT glass transition volume fraction. Figure 4 shows relaxation times and diffusion constants as a function of volume fraction. The relaxation times are defined as the times at which the positional correlators have reached the value 0.1, and the orientational correlators have reached the value 0.02 (since the plateau is quite low). The diffusion constants were determined from the mean squared displacements via the Einstein relation $D = \lim_{t\to\infty} \frac{\mathrm{d}}{\mathrm{d}t}\langle(\Delta\mathbf{r}(t))^2\rangle/6$. The upper panels

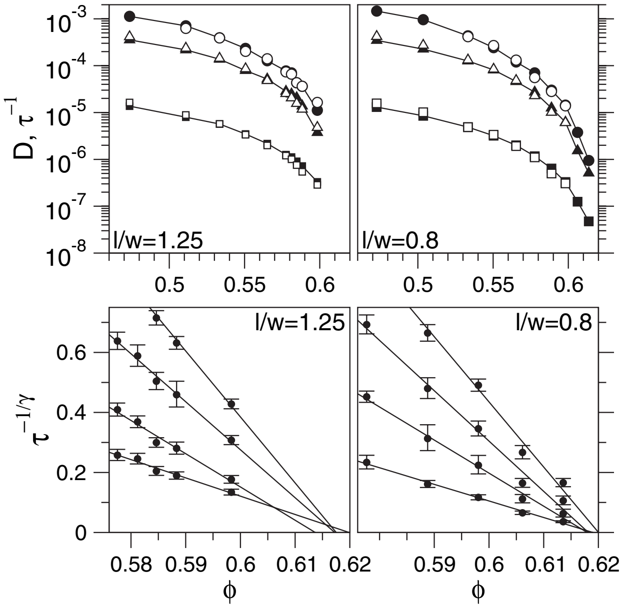

Fig. 4: Upper panels: inverse relaxation times τ^{-1} obtained from $F_{\mathrm{s}}(q_{\max},t)$ (triangles) and from $L_2(t)$ (circles), and diffusion constants D (squares), as a function of volume fraction ϕ. MC data (filled symbols, lines to guide the eye, and rescaled to match MD time scale) and MD data (open symbols) show excellent agreement. Lower panels (MC data only): $\tau^{-1/\gamma}$ multiplied by arbitrary factors for clarity, from $F_{\mathrm{s}}(q,t)$ (several values of q) and $L_2(t)$, demonstrating the validity of the MCT scaling law $\tau^{-1} \propto (\phi_c - \phi)^{\gamma}$. $\gamma = 2.3$. The straight-line fits indicate a glass transition volume fraction of $\phi_c = 0.615 \pm 0.005$ (prolate system) and $\phi_c = 0.618 \pm 0.005$ (oblate system). MD data agree.

of fig. 4 show inverse relaxation times τ^{-1} obtained from $F_{\mathrm{s}}(q_{\max},t)$ (triangles) and from $L_2(t)$ (circles), and diffusion constants D (squares). The MC values (filled symbols) have been multiplied by a factor of 24 (prolate) and 18 (oblate) to match the MD time scale (L_2: 19 and 16, respectively). The errors are of symbol size or less. Note that in each system, one common factor for the positional variables yields excellent agreement between MC and MD (open symbols), in agreement with MCT. The factor for the orientational relaxation times need not be the same since it depends on the choice of the orientational MC move size. The slowing-down of all variables is super-Arrhenius. According to MCT, it should approach a power law of the form $D \propto \tau^{-1} \propto (\phi_c - \phi)^{\gamma}$, where ϕ_c is the MCT glass-transition volume fraction, and γ is related to the von Schweidler exponent b. Both ϕ_c and γ should be system-universal. In the lower panels of fig. 4 we demonstrate the validity of this prediction for the MC results of $F_{\mathrm{s}}(q,t)$ (from top: prolate: $qw = 6.85$, 11, 16; oblate: $qw = 7.85$, 16, 20) and L_2 (bottom). The exponent $\gamma = 2.3$ was chosen in agreement with $b = 0.65$. The straight-line fits comply with a common $\phi_c = 0.615 \pm 0.005$ for the prolate system and with $\phi_c = 0.618 \pm 0.005$ for the oblate system. The fact that there is a common value for positional and orientational relaxation times further demonstrates the strong coupling of these degrees of freedom. We found agreement with the analogous analysis of the MD data. The values we found differ from the MMCT predictions of Letz *et al.* [1], *viz.* $\phi_c = 0.540$ and 0.536 ($l/w = 1.25$ and 0.80, respectively). The mismatch between the numerical MCT calculations based on static structure, and scaling law fits based on simulated dynamics is, however, not unusual [16,17] and has been attributed to activated ("hopping") processes for which MCT does not account. A similar mismatch is found in the hard-sphere system [18]. We note that the present study also displays the prolate-oblate symmetry seen in previous work on the equilibrium properties and dynamics of ellipsoids [1,5,6]. However, we observed that crystallization does not have this symmetry: the prolate system crystallizes more readily.

In summary, we have performed molecular dynamics and Monte Carlo simulations of the hard-ellipsoid fluid. In this very simple anisometric model we observe glassy dynamics sufficiently strong that MCT asymptotic scaling laws can be tested and are found to apply. We find strong coupling of positional and orientational degrees of freedom, leading to a common value for the glass-transition volume fraction ϕ_c for positional and orientational relaxation times ($l/w = 1.25$: $\phi_c = 0.615 \pm 0.005$, $l/w = 0.80$: $\phi_c = 0.618 \pm 0.005$). The presence of glassy dynamics has been predicted by MMCT. However, as MMCT cannot make a statement about crystallization, a test by simulation was required. We argue that particle anisometry acts as a sufficient source of disorder to prevent crystallization. This sheds new light on the question of which ingredients are required for glass formation. Experimental studies of glassy dynamics in the isotropic phase of liquid crystals have been conducted [19], but not in ellipsoids. It is possible to synthesize ellipsoids of colloidal size [20,21] and to study their dynamics with confocal microscopy [22]. In the light of the above, an experimental study of glassy dynamics in colloidal hard ellipsoids seems very promising.

* * *

This work was supported by the Emmy Noether Program and SFB TR6 of the Deutsche Forschungsgemeinschaft (DFG), and the European Network of Excellence SoftComp. We are grateful to M. P. Allen for sharing his molecular dynamics code, to the NIC, Jülich for computing time, and to K. Binder, R. Schilling, M. P. Allen, J. Horbach, J. Baschnagel, W. Kob, M. Letz and W. A. Siebel for helpful suggestions.

REFERENCES

[1] Letz M., Schilling R. and Latz A., *Phys. Rev. E*, **62** (2000) 5173.

[2] Franosch T., Fuchs M., Götze W., Mayr M. R. and Singh A. P., *Phys. Rev. E*, **56** (1997) 5659.

[3] Schilling R. and Scheidsteger T., *Phys. Rev. E*, **56** (1997) 2932.

[4] Götze W., in *Liquids, Freezing, and the Glass Transition*, edited by J. P. Hansen, D. Levesque and J. Zinn-Justin (North-Holland, Amsterdam) 1991.

[5] De Michele C., Schilling R. and Sciortino F., *Phys. Rev. Lett.*, **98** (2007) 265702.

[6] Frenkel D. and Mulder B., *Mol. Phys.*, **55** (1985) 1171.

[7] Wood W. W., *J. Chem. Phys.*, **48** (1968) 415.

[8] McDonald I. R., *Mol. Phys.*, **23** (1972) 41.

[9] Allen M. P., Frenkel D. and Talbot J., *Comput. Phys. Rep.*, **9** (1989) 301.

[10] ten Wolde P. R., Ruiz-Montero M. J. and Frenkel D., *Phys. Rev. Lett.*, **75** (1995) 2714.

[11] Theenhaus T., Allen M. P., Letz M., Latz A. and Schilling R., *Eur. Phys. J. E*, **8** (2002) 269.

[12] Götze W. and Sjögren L., *Rep. Prog. Phys.*, **55** (1992) 241.

[13] Kämmerer S., Kob W. and Schilling R., *Phys. Rev. E*, **56** (1997) 5450.

[14] Chong S.-H., Moreno A. J., Sciortino F. and Kob W., *Phys. Rev. Lett.*, **94** (2005) 215701.

[15] Gleim T. and Kob W., *Eur. J. B*, **13** (2000) 83.

[16] Kob W. and Andersen H. C., *Phys. Rev. E*, **52** (1995) 4134.

[17] Nauroth M. and Kob W., *Phys. Rev. E*, **55** (1997) 657.

[18] Voigtmann T., Puertas A. M. and Fuchs M., *Phys. Rev. E*, **70** (2004) 061506.

[19] Cang H., Li J., Novikov V. N. and Fayer M. D., *J. Chem. Phys.*, **118** (2003) 9303.

[20] Keville K. M., Franses E. I. and Caruthers J. M., *J. Colloid Interface Sci.*, **144** (1991) 103.

[21] Ho C. C., Keller A., Odell J. A. and Ottewill R. H., *Colloid Polym. Sci.*, **271** (1993) 469.

[22] Mukhija D. and Solomon M. J., *J. Colloid Interface Sci.*, **314** (2007) 98.

A Letters Journal Exploring the Frontiers of Physics

November 2008

EPL, **84** (2008) 49901
doi: 10.1209/0295-5075/84/49901

www.epljournal.org

Erratum

Glassy dynamics in monodisperse hard ellipsoids

P. Pfleiderer[a], K. Milinkovic and T. Schilling

Institut für Physik, Johannes Gutenberg-Universität - Staudinger Weg 7, D-55099 Mainz, Germany, EU

Original article: *Europhysics Letters (EPL)*, **84** (2008) 16003.

PACS 99.10.Cd – Errata

After the online publication, we realized some errors in the figures, none of which affect the line of arguments or conclusions of our publication. Corrected versions of figs. 1–3 are published here below. In fig. 1, the curves of the right-hand panels were swapped. In fig. 2, lower left panel, the curves corresponding to the two highest volume fractions were missing. In fig. 3, the data in panels b) and d) is valid, and should be shown, only up to 10^5 MD steps, as crystallization begins in this system thereafter. And regarding fig. 4, we would like to add that the diffusion constants of the prolate ($l/w = 1.25$) system have been divided by 1.3 to match the structural length scale of the oblate ($l/w = 0.80$) system as given by the maximum of the static structure factor.

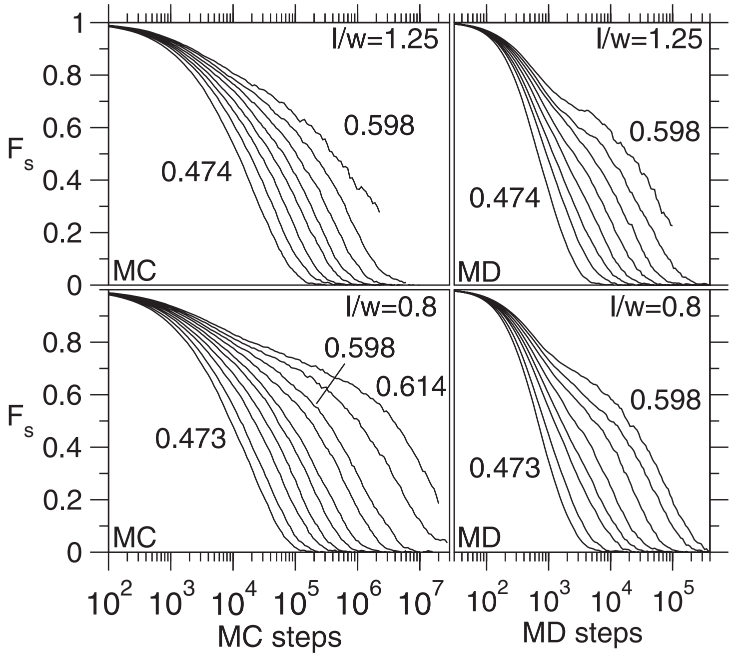

Fig. 1: Self-intermediate scattering functions at several volume fractions ϕ (prolate: 0.474, 0.511, 0.533, 0.551, 0.565, 0.578, 0.588, 0.598; oblate: 0.473, 0.504, 0.533, 0.550, 0.565, 0.578, 0.589, 0.598, 0.606, 0.614). At high volume fractions there is a plateau on intermediate time scales. The final relaxation is slowed down strongly with increasing volume fraction, indicative of glassy dynamics.

---

[a] E-mail: pfleider@uni-mainz.de

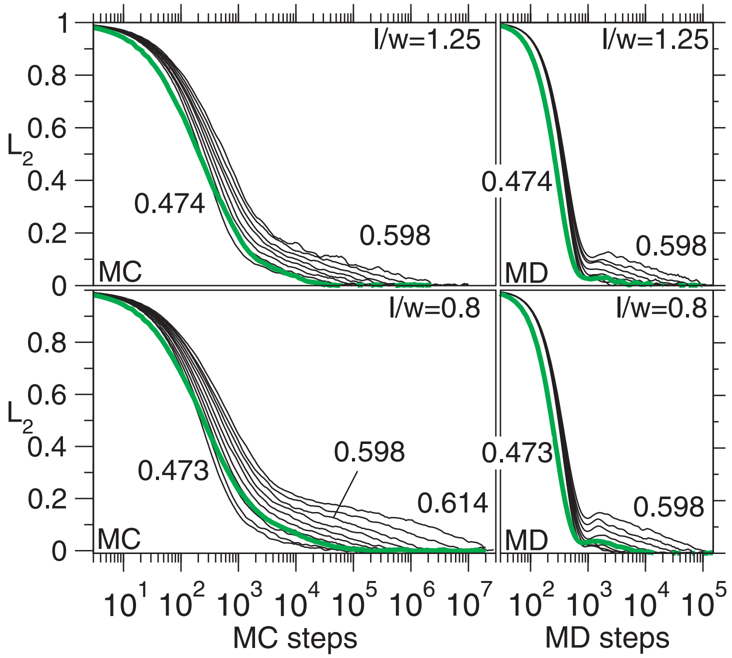

Fig. 2: (Color online) Second-order orientational correlators at several volume fractions ϕ as in fig. 1. Again a plateau develops with increasing ϕ. Hence, orientational degrees of freedom are coupled to the positional ones. Also shown are the third-order correlators at the highest density (bold green lines). They do not slow down, indicating that flipping modes are not affected.

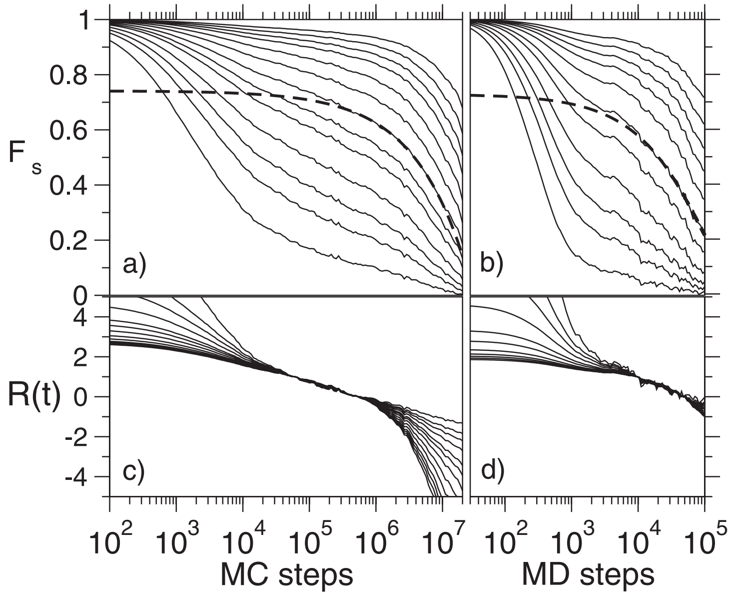

Fig. 3: Self-intermediate scattering functions $F_s(q,t)$ of a) the oblate system (MC data) and b) the prolate system (MD data) at the highest volume fraction, for the range $2.8 \leqslant qw \leqslant 20$. The dashed lines show fits to the von Schweidler law $F_s(q,t) = f_q - h_q^{(1)} t^b + h_q^{(2)} t^{2b}$ with $b = 0.65$. c) and d) show the same data transformed to $R(t) = [F_s(q,t) - F_s(q,t_1)]/[F_s(q,t_2) - F_s(q,t_1)]$. The collapse of the functions onto master curves demonstrates the factorization property.